Novel Digital Signal Processing Techniques for Performance Monitoring in Optical Orthogonal Frequency Division Multiplexing Systems

BO, Tianwai

A Thesis Submitted in Partial Fulfillment

of the Requirements for the Degree of

Doctor of Philosophy

in

Information Engineering

The Chinese University of Hong Kong

September 2016

Acknowledgment

To my great surprise, four years of pursuing a Ph.D. degree elapses so fast that I just set feet in the door of research in fiber-optic communication. Finally, I get the chance to write down the acknowledgment here. I would like to give my great gratitude to my supervisor, Prof. Calvin Chun-Kit Chan. He changed my life from a fated coder to a researcher exploring the unknowns in fiber-optic communication. During the four-year study, I have gained a lot in the countless discussions with Prof. Chan. The self-motivation, dedication to excellence, and optimistic attitude I learned from him, enlightens my research and life. Research is struggle indeed, however I am lucky enough to have Prof. Chan as my director and friend.

I want to extend my gratitude to Prof. Lian-Kuan Chen, for his kind discussions and instructions. I learned a lot from him, not only the critical thinking, the sensitivity to the details and the dynamism of research, but also how to be a noble man of integrity, curiosity, and self-discipline.

I also want to thank the warm-hearted technicians, Barry and Ben, from the Department of Information Engineering. My experiment could not be conducted smoothly without them.

I have learnt quite a lot from the senior guys in the Lightwave lab during my four-year study, and they are Dr. Kam-Hon Tse, Wei Jia, Zhixin Liu and Ming Li. They guided me in how to do research and showed me what the good work was. I would like to extend my gratitude to Professor Guo-Wei Lu and Dr. Ning Deng as well, for offering me valuable opportunities doing research outside the campus.

It is a pleasure to work with all the lab members in the Lightwave lab, Shuang Gao, Xun Guan, Chao Xiang, Zheyu Fan, Yajun Wu, Qianmei Yang, Yang Hong, Tesi Wu, Hon-Tung Luk and Dr. Jin Tang. Thanks for the discussions in the past days. The memories with you all are priceless.

Last but not least, I am deeply indebted to my family, in particular Alice and Richard, you are always the source of my power, the beacon of my life and the fortress of myself. I am pleased to share every happiness in my life with you, as always.

Abstract

The Internet traffic will reach 1.1 zettabytes (1 billion terabytes) per year by 2016 and maintains a 23 percent compound annual growth rate, which heavily relies on optical fiber communications, in both backbone and access networks. To support such enormous volume of traffic, researchers and engineers are working hard to increase the spectral efficiency of current fiber-optic communication systems. It can be achieved by using advanced modulation formats, tightening the channel spacing and adopting novel multiplexing methods. In the meantime, optical network is evolving from fixed grid to flexible grid as the number of connection links grows exponentially. A joint-point technique supporting both high spectral efficiency and good flexibility is optical orthogonal frequency division multiplexing (OFDM), which is a very promising candidate for the next-generation software-defined optical network.

This thesis investigates the optical performance monitoring (OPM) in the optical OFDM enabled optical network, using novel digital signal processing techniques. In addition to the monitoring of fiber impairments, e.g. chromatic dispersion, polarization mode dispersion (PMD), OPM in optical OFDM-enabled optical flexible networks also monitors some new parameters, like laser linewidth and modulation formats, so as to assist the control plane to do dynamic routing. In particular, in this thesis we have studied the PMD monitoring, laser phase noise estimation and compensation, as well as modulation format recognition in optical OFDM systems.

In the first project, we propose a low-cost polarization mode dispersion monitoring scheme for direct-detected optical OFDM (DDO-OFDM) system. Only a low-cost single-ended photodiode is used for PMD monitoring and it achieves a large monitoring range as well as high accuracy. In this

study, we firstly show the novel code-correlated power estimation technique. Then, we apply this technique to realize an accurate PMD monitoring in both double sideband and single sideband 10-Gbps DDO-OFDM systems. Finally, we investigate a cost reduction method using photodiode with low-bandwidth of 1 GHz for monitoring, as well as an accuracy improvement method to make the PMD monitoring insensitive to the input angle of the state of polarization of the optical signal.

In the second topic, the estimation and compensation of laser phase noise at the coherent receiver in a coherent optical OFDM system, is investigated. We propose a novel image processing technique, which is based on the bounding box of the constellation diagram of the received OFDM signal, so as to blindly estimate the common phase error induced by the laser phase noise. Two independent approaches, based on two types of bounding boxes, are proposed and experimentally demonstrated. They show comparable performance with conventional pilot aided method but with much improvement in the spectral efficiency.

In the third topic, we propose a novel blind modulation format recognition (MFR) algorithm, which is applicable to both single-carrier and OFDM systems. It is based on innovative image-processing techniques, including connected component analysis (CCA) which simplifies the MFR computation. Experimental results show the feasibility of the CCA-based MFR algorithm. We also use numerical simulations to investigate the optical signal-to-noise ratio (OSNR) sensitivity and optimize several key parameters of the proposed algorithm. Besides, a performance-enhanced modification has been proposed, and further significant improvement in OSNR sensitivity and reduction in computation complexity have been demonstrated, via both numerical simulations and experiments.

摘要

根據最近的報告，整個互聯網的流量在 2016 年將達到 1.1 澤字節，並且保持 23 個百分點的年增長率。這將導致無論是在骨幹網絡還是接入網絡，都將重度依賴光纖傳輸網絡。為了支持這樣巨大體量的數據傳輸，研究者和工程師都在努力提升現有光纖傳輸鏈路的頻譜利用效率。這可以經由使用高階調製格式，減少信道之間的間距，和新的維度上的複用技術來實現。與此同時，光網絡自身的運轉也在逐漸從固定的模式向更加彈性的方式轉變，這是由於光網絡中的連接數量一直保持著指數級的增長。光正交頻分複用技術能夠同時支持上述的高頻譜利用效率和彈性的網絡運轉模式，因此成為一項非常有前途的，支持下一代軟件定義光網絡的候選方案。

在這篇論文中，我們主要研究使用新穎的數字信號處理技術在光正交頻分複用系統中進行光性能監控。和在傳統的光網絡中進行光性能監控的關注點不同，在光正交頻分複用系統實現的彈性光網絡中進行光性能監控并不局限于監控光纖的損傷，比如光纖的色散和偏振模式色散。新的監測項目，比如激光器的線寬，以及在光網絡中傳輸的信號調製格式，都需要被監控，以便幫助網絡的控制層來實現更智能的動態交換。具體來說，我們研究了在光正交頻分複用系統中的偏振模式色散的監控，激光器相位噪聲的估計和補償，以及調製格式的識別。

在第一項研究中，我們提出了一個針對直接檢測的光正交頻分複用系統的低成本偏振模式色散監控方案。在這個方案中，只需採用一個低成本的單端光電二極管，就能實現

對光纖偏振模式色散的較大監測範圍和較高的準確度的監測。首先，我們提出了一項創新性的基於一段編碼的相干運算的功率估計技術。然後，我們在雙邊帶和單邊帶的 10 吉比特直接監測光正交頻分複用系統中實現了精確的偏振模式色散監測。最後，我們研究了如何使用更低帶寬的光電二極管來進一步降低成本的方案，以及實現了對輸入的光信號偏振態不敏感的更加精確的監測方案。

在第二項研究課題中，我們研究了解決相干光正交頻分複用系統中的激光器相位噪聲的估計和補償問題。我們創新性地提出使用圖像處理技術來解決這個問題。經過傅里葉變換之後的光正交頻分複用信號的星座圖，它的邊界框的偏轉被用來盲估計激光器相位噪聲導致的共同相位錯誤。兩種獨立的方案，依賴于兩種不同的邊界框類型，經實驗證明可以成功地估計和補償上述的共同相位錯誤。他們同常用的插入已知相位的載波方式相比，在同樣的性能下，有著大大提高的頻譜利用效率。

在最後一項研究課題中，我們提出了一種新穎的盲調製格式識別的算法，這種算法借助圖像處理技術，對單載波相干通信系統和光正交頻分複用系統都能成功的識別出其調製格式。它的核心技術是圖像處理技術中的連接成分分析，使用這種方法可以大大簡化調製格式識別的運算。實驗結果表明了這種方法的可行性，我們還進行了數值仿真來研究這種方法對光信噪比的敏感度，並且優化了算法中的數個核心參數。最後，我們提出了一種改進方案，來進一步提高對光信噪比的敏感度，同時降低運算複雜度。這種改進方案也被數值仿真和傳輸實驗證明。

Table of Contents

List of figures and tables

Chapters 1 Introduction

1.1 Optical orthogonal frequency division multiplexing (OFDM) system

1.1.1 Introduction to OFDM system

OFDM has been widely used in wired broadcasting transmission systems, wireless local area networks, and mobile communications. It can effectively mitigate the dispersion in a multi-path wireless channel. Optical OFDM systems with different implementation methods have been developed individually in [1] [2] so as to combat the dispersion in single mode fiber. It shows superior tolerance to chromatic dispersion [2] and polarization mode dispersion [3]. Besides, optical OFDM exhibits higher spectral efficiency and better flexibility, making it a very promising enabling technique for next-generation flexible software-defined optical networks [4].

The concept of OFDM was first proposed in 1966 in a United State patent [5] and the first practical application was realized by Cimini at Bell labs in mobile communication in 1985 [6]. Soon it became popular in both wireline broadcasting and access networks. In 1998, discrete multi-tone (DMT) modulation was standardized as the enabling technique in asymmetric digital subscriber line (ADSL) systems, which enabled high speed Internet access for more than 10 years. Nowadays, OFDM has the widest application in wireless local area networks and the fourth generation mobile networks.

OFDM was first adopted in optical wireless transmission in 2001 [7]. Later, in 2005, it was implemented in multimode fiber optical systems to tackle the intermodal dispersion [8]. The first coherent optical OFDM system was demonstrated in 2006 [2]. After that, many optical OFDM implementations were proposed for different specific applications. High speed, long haul transmission of 8000 km over standard single mode fiber [9] and a record spectral efficiency of 14bit/s/Hz [10] have been demonstrated these years. Recently, optical OFDM has also found its applications in passive optical networks (PON) [11] and short reach communications [12] for its full utilization of channel bandwidth. Fig. 1.1 shows the historical development of the OFDM theory and application by 2008.

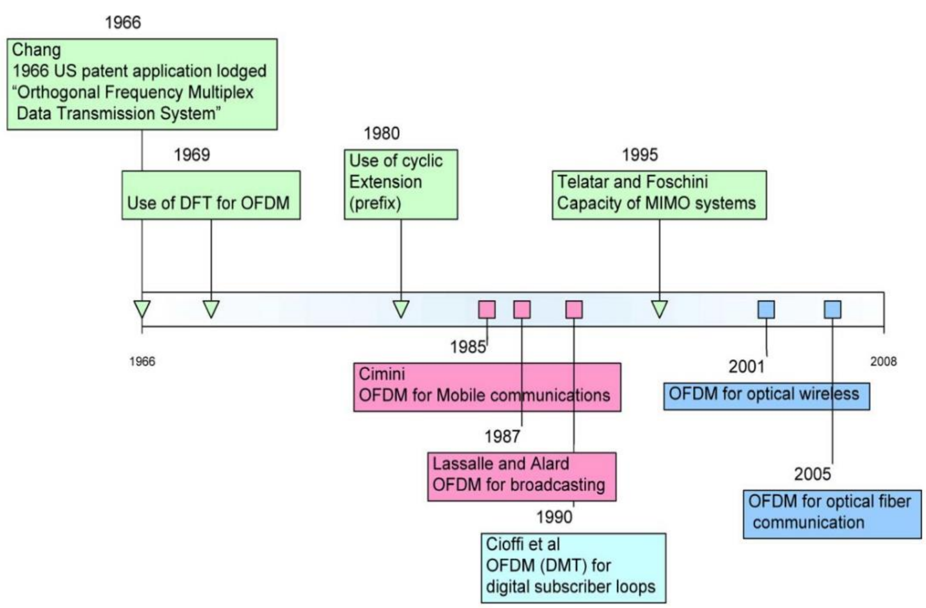

Fig. 1.1 Historical development of the underlying theory of OFDM and its practical implementation by 2008. [13]

1.1.2 OFDM Basis

Among various multiplexing domains, OFDM can be classified into a frequency multiplexing system, but with a much narrower frequency spacing. Actually, the adjacent subcarriers in the

OFDM system overlap, which are attributed to the orthogonality among neighboring subcarriers. Obviously, OFDM has much improved spectral efficiency than the conventional frequency division multiplexing (FDM) system. Besides, it has great tolerance to dispersion, by simply inserting a cyclic prefix before one OFDM symbol. Here we give a brief introduction of the principle of OFDM, mainly on the orthogonality of the subcarriers, the cyclic prefix, and the basic system structure.

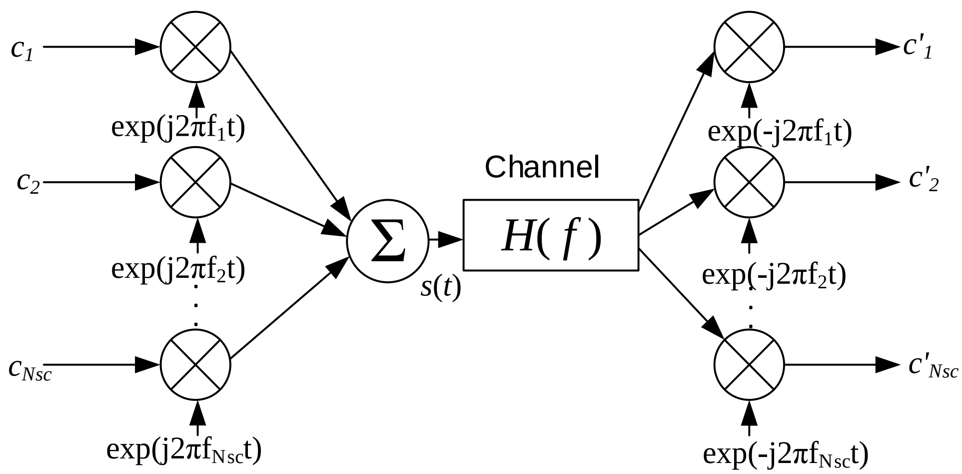

Fig. 1.2 Conceptual diagram for a generic multi-carrier modulation (MCM) system [14]

Fig. 1.2 shows a conceptual diagram for a multi-carrier modulation (MCM) system. N_{sc} is the total number of subcarriers, c_{ki} is the i-th information symbol on the k-th subcarrier, and f_k is the frequency of the k-th subcarrier. Therefore, the modulated signal $s(t)$ is

$$s(t)=\sum_{i=-\infty}^{+\infty}\sum_{k=1}^{N_{sc}}c_{ki}\prod(t)\exp\left[j2\pi f_k\left(t-iT_s\right)\right] \tag{1.1}$$

$$\prod(t)=\begin{cases}1, & \left(0<t\le T_s\right)\\ 0, & \left(t\le 0,\ t>T_s\right)\end{cases} \tag{1.2}$$

where T_s is the symbol period, and $\Pi(t)$ is the waveform shaping function. Eq. (1.2) denotes a rectangular waveform profile. At the receiver, assume an optimized detector is used for each subcarrier, then the detected information symbol at the output is

$$c'_{ki} = \int_0^{T_s} r(t - iT_s) s_k^* dt = \int_0^{T_s} r(t - iT_s) \exp\left(-j2\pi f_k t\right) dt \tag{1.3}$$

We are interested in the correlation between any two subcarriers,

$$\begin{aligned} \delta_{ki} &= \frac{1}{T}\int_0^{T_s} s_k s_l^* dt = \frac{1}{T}\int_0^{T_s} \exp\left(j2\pi \left(f_k - f_l \right) t \right) dt \\ &= \exp\left(j\pi \left(f_k - f_l \right) T_s \right) \frac{\sin\left(\pi \left(f_k - f_l \right) T_s \right)}{\pi \left(f_k - f_l \right) T_s} \end{aligned} \tag{1.4}$$

Therefore, as long as the following condition is satisfied,

$$f_k - f_l = m\frac{1}{T_s} \tag{1.5}$$

we can tell that the two subcarriers are orthogonal to each other, as their correlation is 0. In this way, the channel spacing between subcarriers can be as small as $1/T_s$, which makes a high spectral efficiency.

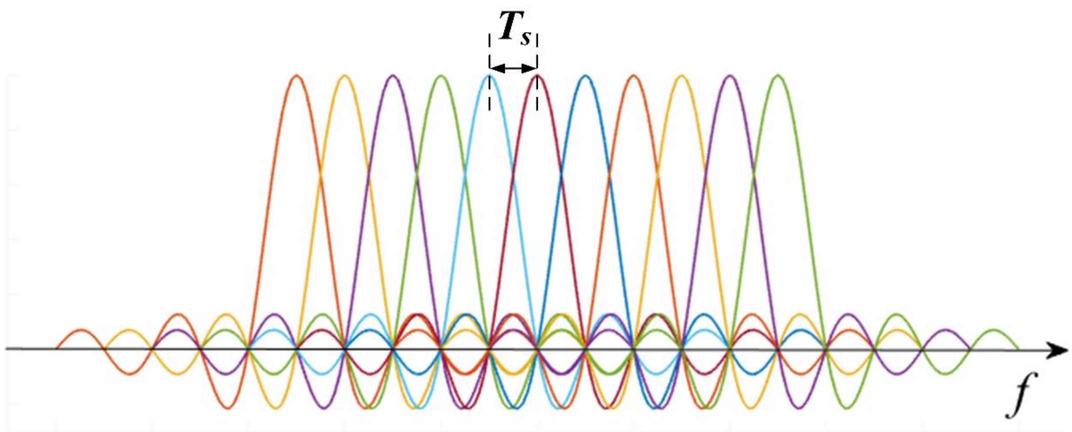

Fig. 1.3 Spectrum of an OFDM signal

From Fig. 1.3, we can see that there is overlapping between adjacent subcarriers of the OFDM signal. Meanwhile, there is no inter-carrier interference (ICI) as long as the orthogonality among the subcarriers preserves.

Cyclic prefix (CP) is a very important element of OFDM. By inserting a copy of the partial trailing waveform at the end of the OFDM symbol to its beginning, the dispersion-induced time walk-off can be recovered as long as the group delay is within the length of CP. Thus, the dispersion only introduces a subcarrier-dependent phase rotation to each subcarrier, which can be readily corrected via a one-tap equalizer. The principle of the introduction of phase rotation could be derived from the property of discrete Fourier transform (DFT) as follows:

$$y(n) = x\left((n+m)\right)_N R_N(n) \tag{1.6}$$

$$Y(k) = DFT\left[y(n)\right] = \exp(-j2\pi km/N)X(k) \tag{1.7}$$

where N is the DFT size, and m is discrete delayed length, ((.)) is the periodic extension, and R_N is the principal values of the periodic extension. Fig. 1.4 shows the process of CP insertion, as well as the DFT window misalignment, due to the dispersion effect. The CP mechanism saves the computation-intensive equalization at the receiver, while only simple one-tap equalization can effectively combat the dispersion effect. In general, the length of CP is proportional to the maximum chromatic dispersion it can tackle. However, the CP increases the overhead, thus reduces the spectral efficiency. Hence, the length of CP is an important parameter to be optimized in the OFDM system design.

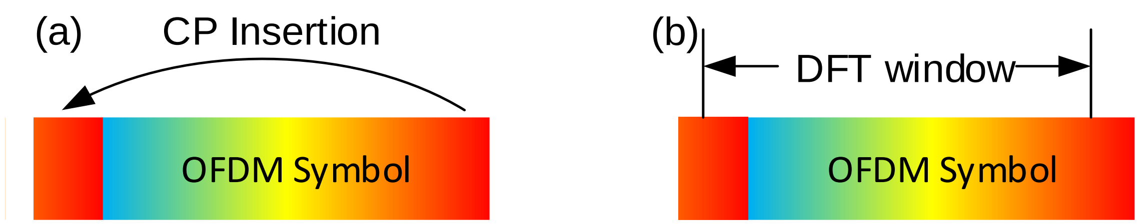

Fig. 1.4 Illustration of (a) cyclic prefix insertion; (b) DFT window misalignment.

Then it comes to the system structure of the OFDM system. The multiplication of each subcarrier and its respective data, together with the summation in Fig. 1.2, can be effectively implemented via inverse fast Fourier transform (IFFT), which is the engineering implementation of inverse discrete Fourier transform (IDFT). Therefore, the data modulation and multiplexing can be achieved at the same time by IFFT effectively. Reversely, demultiplexing and demodulation can be implemented in a similar but reverse way, by fast Fourier transform (FFT) at the receiver. Fig. 1.5 shows the system structure. By the subcarriers multiplexing, high-speed serial data streams are transmitted in parallel channels, thus the data rate for each subcarrier is relatively low, which alleviates the requirement for high-speed electronics. The optical link provides a linear channel for the electrical OFDM signals, through frequency up-conversion and down-conversion.

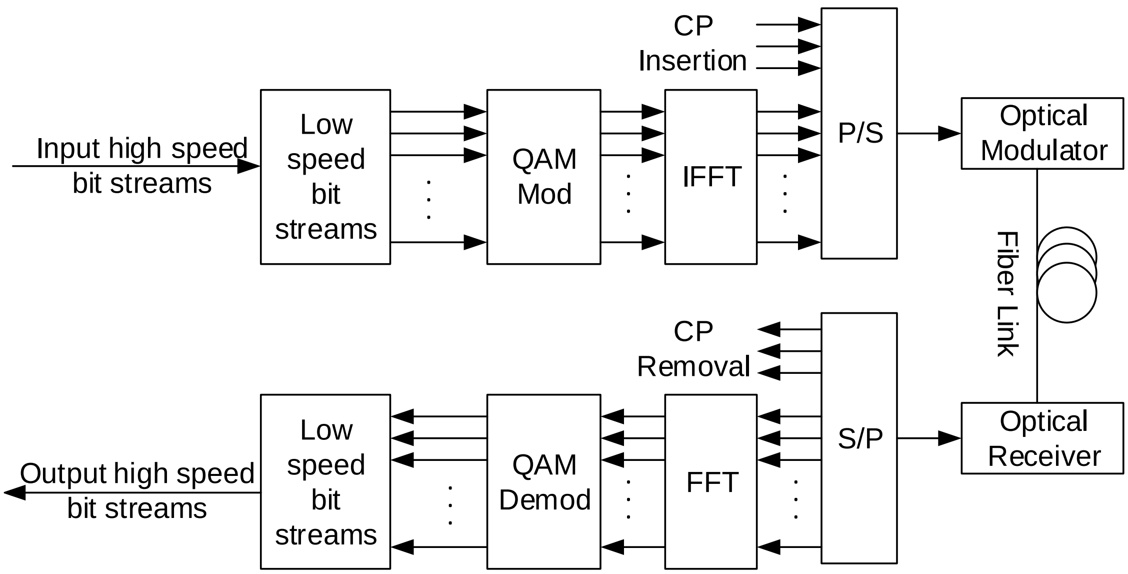

Fig. 1.5 System structure of optical OFDM system. Mod: modulation, QAM: quadrature amplitude modulation, Demod: demodulation; P/S: parallel-to-serial; S/P: serial-to-parallel.

According to the detection method used, optical OFDM system can be categorized into direct-detected optical OFDM (DDO-OFDM) and coherent optical OFDM (CO-OFDM). Fig. 1.6 shows the corresponding optical receivers used in these two kinds of optical OFDM systems. It can be clearly seen that the DDO-OFDM has much simpler structure than that of the CO-OFDM. However, CO-OFDM enjoys more degrees of freedom (DOF) to support more multiplexing methods. CO-OFDM also gives higher receiver sensitivity, owing to the use of local oscillator. A detailed comparison between CO-OFDM and DDO-OFDM is depicted in Table 1.1.

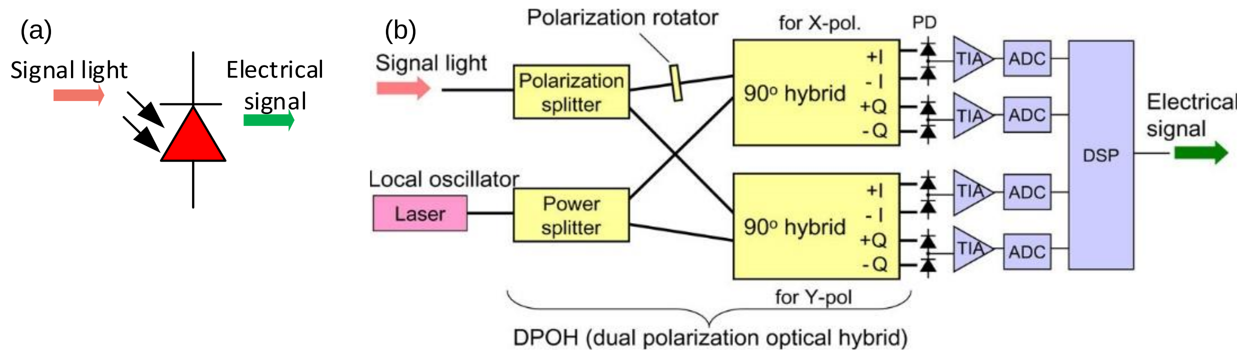

Fig. 1.6 (a) Direct-detected photodiode (b) structure of coherent optical receiver.

Table 1.1 Comparison of CO-OFDM and DDO-OFDM

	CO-OFDM	DDO-OFDM
Receiver	Coherent receiver	Simple photodiode
Sensitivity of receivers	High sensitivity	Require higher OSNR
Spectral efficiency	High	Usually need guard band
DSP complexity	High	Low
Cost	High	Low
Application	Long-haul	Metro, Access network

1.1.3 OFDM in software-defined optical network (SDN)

Optical OFDM has long been considered as a very promising physical-layer interface for flexible/elastic and software-defined networks shortly after it has been proposed [4], for its high spectral efficiency and adaptive data rate modification. In an elastic optical network, the two main features are the flexible grid, instead of the rigid grid, as well as adaptive data rate and modulation format according to the channel state information. These requirements pose new challenges to the conventional single-carrier transponders and wavelength cross-connects deployed in the network.

Nevertheless, multi-carrier modulation schemes show a significant advantage in the elastic optical networks. The subcarriers in an optical OFDM system can be easily assigned with different modulation formats so as to reserve sufficient margin for the transmission. Meanwhile, the occupied bandwidth of a certain channel can be modified by aggregating different number of subcarriers to form the optical OFDM signal. In this way, the granularity of the whole system is determined by the channel spacing of the OFDM system, which is two to three orders of magnitude lower than the current grid in optical network.

Optical OFDM system has appeared in the proposal of spectrum-sliced elastic optical path network (SLICE) [15]. Fig. 1.7 shows the spectrum assignment in SLICE network architecture. Traditional fixed-grid optical network wastes the spectrum resource especially when the traffic in one channel is excessively small. The relative large guard band between the neighboring channels aggravates the waste as well. On the contrary, the flexible spectrum assignment scheme requires narrower guard band, and the bandwidth is adaptively allocated according to the traffic demand. To support the flexibility, OFDM is utilized at the software-defined optical transponder (SDOT) [16], which can (i) dynamically set up the physical link without human intervention; (ii) assign an optical line rate for the link with enough margin; (iii) support multiple formats; and (iv) actively report the channel state information to the control plane. This SDOT can be implemented by either electrical or all-optical manner, as depicted in Fig. 1.8. Therefore, modification of the modulation format and the data rate (bandwidth) could be made in either the OFDM transmitter, or the physical layer (PHY) of the current optical transport network (OTN), respectively.

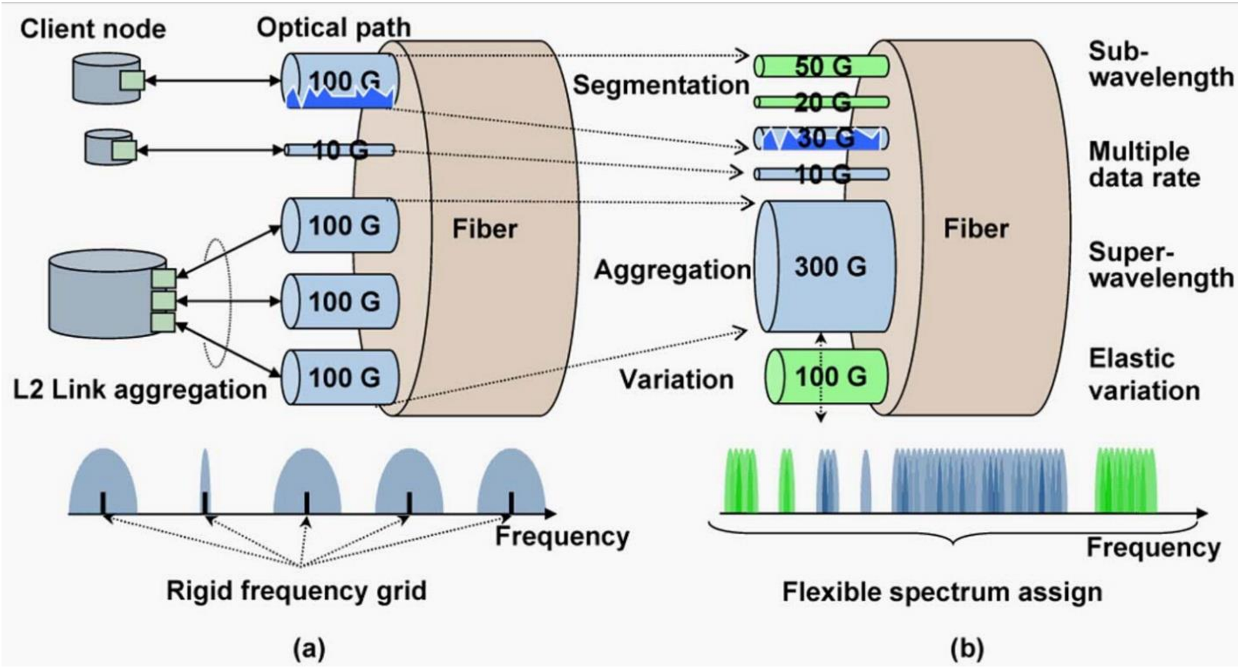

Fig. 1.7 Spectrum assignment in SLICE: (a) conventional optical path network, and (b) SLICE [13].

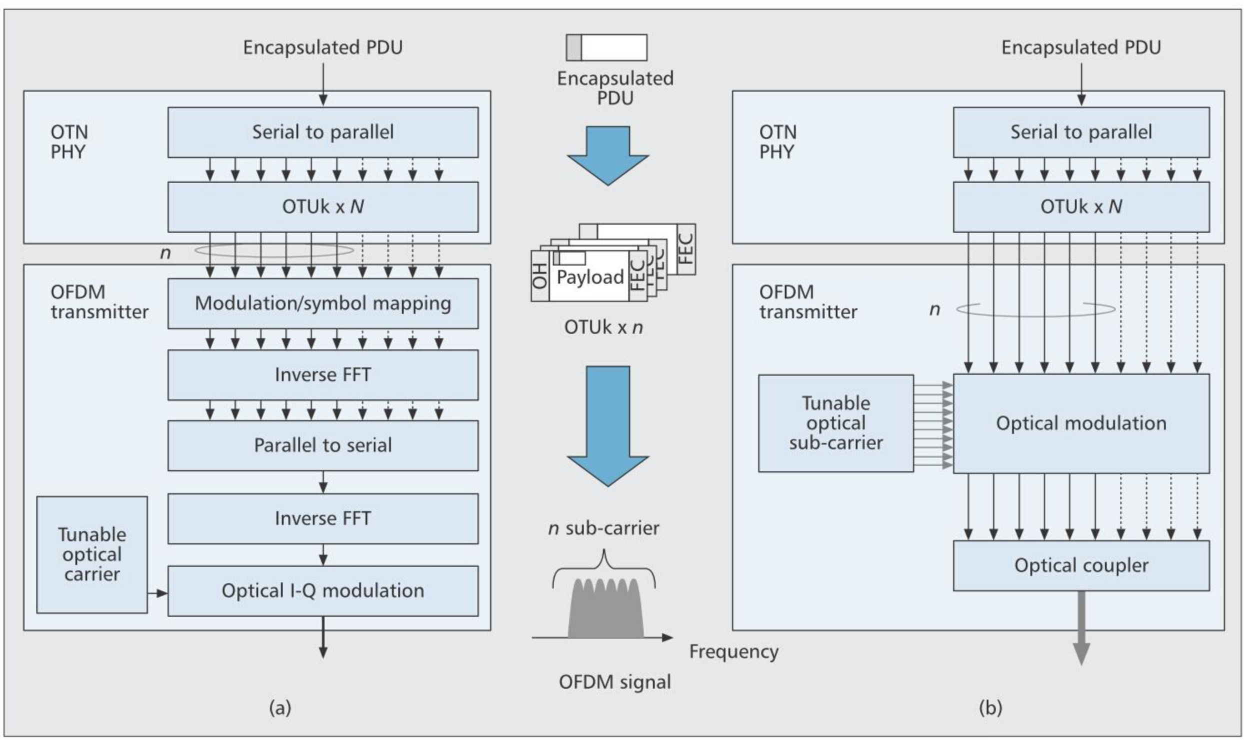

Fig. 1.8 Implementation examples of OTN PHY and OFDM optics (a) electrical approach; (b) optical approach.[15]

1.2 Optical performance monitoring

Currently, optical networks are progressing towards reconfigurable, flexible and smart fashion. The optical network we are facing today and in the near future is much more sophisticated than what we are accustomed to before. Therefore, the optical signal is more vulnerable to the impairments in the fiber link. To assure the quality of service (QoS) of the data delivery, optical performance monitoring is a highly indispensable element in the network management. The application of OPM in current reconfigurable and flexible optical network is reflected in the following aspects: (a) fault identification and location; (b) network resiliency (c) impairment-aware routing; (d) dynamic bandwidth allocation; (e) adaptive modulation format modification. The channel state information (CSI) is of great importance for the control plane, and is the essential information to support the reconfigurability and flexibility. OPM elements need to be distributively deployed in the network, both at the intermediate nodes and the receivers, so as to provide as much information as possible. Fig. 1.9 shows the general parameters to be monitored in a typical optical network. Of course, the diversity of fiber-optic communication techniques makes the task of monitoring vary case by case in different transmission systems, as the dominant impairments may differ. However, in the viewpoint of network management, ubiquitous monitoring is necessary to provide enough information for the control plane. In this section, we briefly review the fiber impairments, current OPM techniques, and in particular, the OPM in optical OFDM systems.

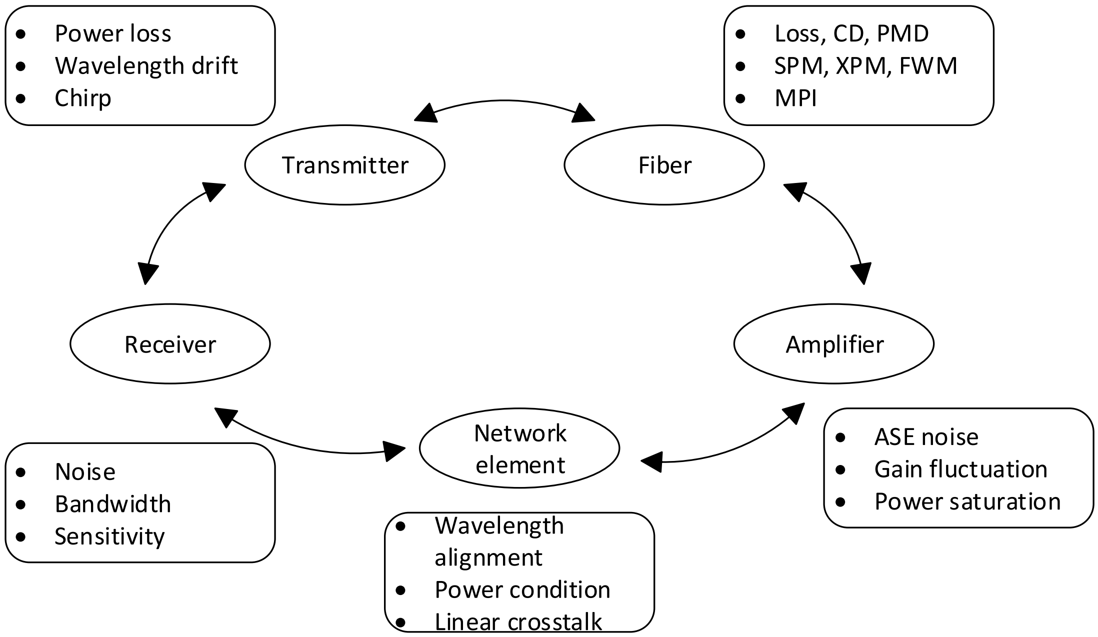

Fig. 1.9 Overview of various optical impairments within the network [17]

1.2.1 Transmission impairments

In general, the dispersion effects like chromatic dispersion (CD) and polarization mode dispersion (PMD), the polarization dependent loss (PDL), fiber nonlinearity and the optical signal-to-noise ratio (OSNR) are the key parameters to be monitored as their effects are closely relative to the signal quality. In this section, we only focus on the transmission impairments in single mode fiber (SMF).

The group index in SMF slightly varies at different wavelengths, thus the light travels at different speeds. This leads to material dispersion. Besides, the shape of the waveguide together with the refractive index profile in the fiber core and claddings bring another kind of dispersion known as waveguide dispersion. These two types of dispersion have opposite influence on the optical signal, and the overall effect is close to zero at around 1310 nm in SMF. With the presence of chromatic dispersion, short optical pulse is spread out into a broader distribution. In the direct-detection system, CD introduces a frequency selective power fading due to the power-law of photodetectors.

Polarization mode dispersion originates from the birefringence in optical fiber, which leads to the difference in refractive indices between the two orthogonal polarization modes. The birefringence comes from the imperfection in the fiber fabrication. As different polarized mode of light travels at a different speed in SMF, the optical pulse width will be broadened as well. The first order PMD is called differential group delay (DGD). It is one of the most important parameters to be monitored, as it introduces inter-symbol interference (ISI), especially in high-speed optical transmission systems. An in-depth review of PMD-related effects and mitigation methods will be presented in Chapter 2.

Polarization dependent loss originates from the Dichroism of optical components, fiber bending and oblique reflection, resulting in power variations in the transmission system. It also induces power imbalance in the polarization multiplexed system. It is defined by the power ratio of the maximum optical power and the minimum optical power among all the states of polarization.

$$PDL_{dB} = 10 \times \log\left(\frac{P_{Max}}{P_{Min}}\right) \tag{1.8}$$

In an optical transmission system in which these devices are deployed, the total PDL of the link should be carefully monitored, so that further mitigation method has to be taken if it is getting disastrous.

Fiber nonlinearity is also an important impairment in fiber transmission. It can be categorized into two groups, according to the origin. The first group is related to Kerr effect, through which the refractive index is dependent on the optical intensity. Self-phase modulation (SPM), cross-phase modulation (XPM) and four-wave mixing (FWM) belong to this group. The second group, which is related to nonlinear optical scattering, includes stimulated Raman scattering (SRS) and stimulated Brillouin scattering (SBS). The scale of nonlinearity is determined by the product of optical power and effective transmission length. Fiber nonlinearity is the main barrier for ultra-long-haul fiber transmission.

OSNR is one of the most important parameters in the fiber-optic transmission system design. Its common definition is given by [18]

$$OSNR_{dB} = 10\log\frac{P_i}{N_i} + 10\log\frac{B_m}{B_r} \tag{1.9}$$

where P_i is the signal power, N_i is the noise power, B_m is the signal bandwidth and B_r is the reference bandwidth (0.1 nm, usually). Noise in fiber-optic system mainly comes from optical amplifiers, which have non-negligible noise figure that degrades the OSNR of the output optical signal.

1.2.2 Overview of OPM techniques

OPM has been a hot research topic over the past years. Many schemes have been proposed to monitor the fiber impairments, as mentioned in the last section, such as timing alignment [19, 20], frequency chirp, excessive filtering, interference effect and other parameters that affect the signal quality. In this section, we try to give an overview of the current OPM techniques, in the following four domains: time domain, frequency domain, polarization domain and digital domain.

The most straightforward method in the time domain monitoring is examining the eye diagram of the signal [21]. The eye diagram is a direct indication of the signal quality, and most impairments have their own specific behaviors in the eye diagram. Other time domain methods include asymmetric amplitude histogram [22], delay-tap sampling [23], two-tap sampling [24] and linear optical sampling [25].

Dispersion effects like CD and PMD are frequency dependent. Hence, the frequency spectrum of the signal can be used to monitor the optical performance. The RF tone, either inherent [26], regenerated [27], or extrinsic (inserted for monitoring purpose) [28] is a useful tool in OPM. In some monitoring schemes, characteristics of the spectrum, either optical spectrum [21]or electrical spectrum [29], are used for monitoring.

In the polarization domain, two commonly used techniques are polarization nulling and measuring the degree of polarization (DOP). The former makes the use of the fact that noise in an optical signal is usually unpolarized, while the signal is polarized. By sweeping all the state of polarization (SOP), the power of the signal and the noise are derived, thus the OSNR is easily obtained [30]. On the other hand, PMD depolarizes the optical signal, thus the DOP varies with respect to the PMD value. Hence, the DOP can be used to estimate PMD of the fiber link [31, 32].

The digital domain here refers to the newly proposed OPM techniques that require digital signal processing techniques to retrieve OPM information. For example, artificial neural network (ANN) can use the parameters derived from eye diagram [33], asymmetric amplitude histogram [34] and delay-tap sampling techniques [35] to monitor the fiber impairments. On the other hand, digital signal processing is widely used in coherent optical communications, in which advanced modulation formats, polarization multiplexing, and pulse shaping make OPM more challenging [36]. The coefficients from the converged digital equalizers can be used for OPM monitoring [37].

1.2.3 OPM in optical OFDM system

In optical OFDM system, chromatic dispersion induced dispersion can be compensated as long as the dispersion is within the period of cyclic prefix. In particular, the polarization mode dispersion and polarization dependent loss are not a big problem in coherent optical OFDM system. However, optical performance monitoring is still crucial in optical OFDM system. In an optical network, optical paths are dynamically set up and routed, so the accumulated chromatic dispersion could be very large. It has the possibility of exceeding the CP length. On the other hand, if the control plane knows the exact value of the accumulated chromatic dispersion, the length of CP can be further optimized and so as the spectral efficiency. Moreover, direct-detected optical OFDM (DDO-OFDM) is more and more popular in the metro/medium transmission, in which CD and PMD could induce frequency dependent power fading caused by the square-law photodetector. In addition, OSNR should be actively monitored among the whole network, as its value is the key metric for adaptive modulation format and data rate in a flexible optical network.

Optical performance monitoring has new challenges in the OFDM enabled flexible optical network, compared with that in the conventional single-carrier fiber-optic transmission system. The channel spacing of the formers becomes much narrower. As shown in Fig. 1.10, the spacing between subcarriers, Δf, is much smaller than the channel guard band, Δf_G. It is worth pointing out that Δf_G is still smaller than current fixed-grid of dense wavelength division multiplexing (DWDM) standard, which is 50/100 GHz. On the other hand, time-domain OFDM signal does not have constant amplitudes, but a noise-like multi-level amplitudes distribution. Therefore, the traditional delay interferometer based methods [38, 39] do not apply to optical OFDM signal.

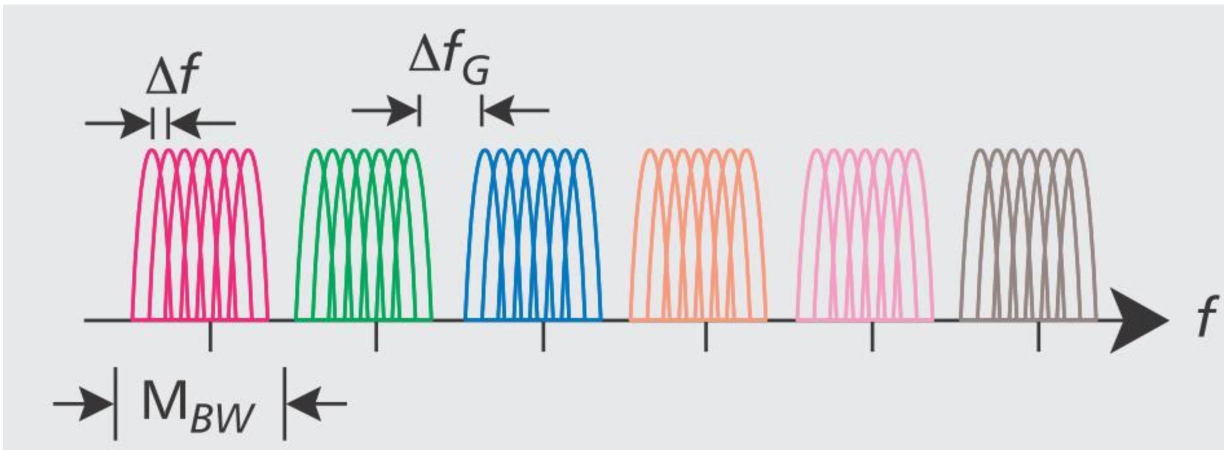

Fig. 1.10 Optical spectrum of OFDM-based flexible optical network.

Fortunately, an OFDM symbol usually consists of training symbols, which are initially designed for timing synchronization, frequency offset estimation, polarization demultiplexing and channel estimation. Training symbols are commonly pre-known by the receiver so that optical performance monitoring could be implemented via normal or specially designed training symbols [40, 41], which significantly alleviates the difficulty of monitoring.

Since optical OFDM was proposed as a new modulation format in 2006, the subsequent research on optical performance monitoring in optical OFDM has been performed since 2007 [40]. The optical channel estimation information at the coherent receiver is used to estimate the chromatic dispersion, OSNR, and Q-factors in [40]. Experimental demonstration of simultaneously CD and PMD monitoring using the same method was reported in [41]. In [42, 43], a coherent receiver with low bandwidth was used to monitor OSNR and first-order PMD, respectively. The principle in the latter OPM schemes is quite different from the monitoring schemes based on channel estimation. The sampled signal is converted to Stokes space, where the OPM is performed without aided-data.

1.3 Research challenges in optical OFDM enabled Software-defined optical Network

1.3.1 OPM in OFDM enabled software-defined network

As discussed in 1.1.3, software-defined network dynamically manages the optical network according to channel state information. On one hand, OPM will play more important role in the agile network operation which is on its way towards robustness, flexibility, and reconfigurability. On the other hand, the reconfigurable capability poses new challenges to OPM as well. In addition to the monitoring accuracy, the response time, dynamic range of monitoring and the cost are more crucial in the flexible optical network. Hence, we will discuss a few challenges of OPM in OFDM enabled SDN.

The first challenge is the **much-reduced channel spacing**. In the flexible network, the fixed grid is becoming flexible and the channel spacing becomes much narrower. Previous 50 GHz grid is reduced to 12.5 GHz, or even 6.25 GHz in the new proposal, so as to increase the spectral efficiency. Moreover, the channel spacing between subcarriers in optical OFDM system can reduce to several GHz to tens of MHz. It brings problems for conventional OPM techniques. For example, it is hardly possible to use the state-of-the-art optical spectrum analyzer (OSA) to measure OSNR of each subcarrier of the optical OFDM signal, as it is hard to interpolate the noise level under such narrow channel spacing, limited by the resolution of OSA.

The second issue is the **accommodated transparency**. The OPM techniques used in the SDN should be transparent to the modulation format, which is adaptive to the transmission length and the bandwidth allocated. Conventional OPM techniques are mostly proposed to handle the modulation formats used in the direct-detection system. The monitoring of higher order modulation formats, which are usually implemented in coherent optical communication systems, is still ongoing. Moreover, the widely used polarization multiplexing, even the spatial division multiplexing which is still under investigation, puts forwards new challenge to current OPM techniques.

The last concern is **the cost**. It is clearly seen that the number of performance monitoring modules in the SDN will skyrocket due to massive, distributed deployment at intermediate nodes and receivers in the network. Therefore, passive methods are preferred rather than active methods, direct-detection methods are preferred rather than coherent-detection methods, multi-purpose and integrated devices are preferred rather than sole-purpose, bulky devices.

1.3.2 New parameters to be monitored

With the evolution of fiber-optic transmission from direct-detection manner to coherent detection, especially the low-cost, powerful CMOS techniques are massively used in the coherent receivers, the focus of OPM changes. CD and PMD are not that important as those in the intensity modulated/direct-detection (IM/DD) systems. Nevertheless, OSNR remains its importance to be monitored. The challenge is to perform accurate in-band OSNR monitoring, in the presence of nonlinearities.

In particular, laser linewidth, which characterizes the laser phase noise, is attracting more attentions in coherent optical systems. An optical OFDM system is well known to be more vulnerable to the laser phase noise than in a single-carrier system, due to its relative long symbol duration. The impairment-aware routing could still fail if the linewidth information is not considered even though other fiber impairments have been taken into consideration. Therefore, monitoring of the laser linewidth can fill the black point in the blind zone of conventional OPM techniques. Recent research on this new topic has been reported in the literature [44].

Another novel monitoring item can be the modulation format of the optical signals. In SDN, the receiver can get the information of the modulation format from the control plane, which embeds the modulation format information through specific protocol and sends to the receiver. However, it takes an additional path to carry the control information. There is another possibility that the receiver can recognize the modulation format blindly, although the recognition time is still a vital issue. In this way, it can reduce the traffic in the control path. In burst mode optical communication system, the feature of modulation format recognition is highly desirable, as long as it can respond fast enough.

1.4 Contributions of this thesis

This thesis research aims to investigate the optical performance monitoring techniques in optical OFDM systems. We have proposed several novel OPM related techniques for optical OFDM systems, especially considering the SDN enabled by optical OFDM system, using digital signal processing techniques.

1.4.1 Low-cost PMD monitoring scheme in direct-detected optical OFDM system

In this work, we propose a low-cost PMD monitoring scheme for DDO-OFDM system. A pair of codes is inserted into two subcarriers of the OFDM signal. At the direct-detection receiver, code correlation is performed to estimate the powers of these two code-assisted subcarriers. Their power ratio is then used to estimate the first-order DGD value of the fiber link.

The proposed scheme is first experimentally demonstrated in a vestigial sideband DDO-OFDM system. Then we apply the proposed scheme in an RF-tone-aided single sideband DDO-OFDM system, which supports high-speed and long-haul transmission. The monitoring accuracy and the tolerance to other fiber impairments, like chromatic dispersion, have been investigated. Finally, we demonstrate the feasibility of using a low-bandwidth photodiode in this monitoring scheme, to further reduce the cost.

To support random polarization walk-off, we propose a three-pilot-subcarrier scheme. It shows good tolerance to the scrambled polarizations. The PDL effect on the monitoring accuracy is also discussed in this work.

1.4.2 Laser phase noise compensation in coherent optical OFDM system

In this work, we take the first investigation to use image processing technique to compensate the common phase error (CPE) induced by laser phase noise in a CO-OFDM system. We propose a novel scheme, which originates from the skew detection and correction problem in image processing, to blindly correct the common phase rotation. The bounding box of the constellation diagram is used to evaluate the scale of rotation. A series of test phases are applied to rotate the constellation of received data samples, and the test phase with the minimum area of the bounding box is the estimated rotated angle for correct CPE estimation. We show that, it is a simplified modification of blind phase searching algorithm, and the computation complexity has been investigated.

On the other hand, we propose another approach to solve the CPE problem. It is also based on image processing, in which the convex hull of the constellation points is used to quickly determine the rotated angle. It does not require test phases and has much reduced complexity.

The root mean square errors of the two proposed algorithms have been investigated, via numerical simulations. Meanwhile, we conduct both back-to-back and long-haul transmission experiment, to verify the feasibility of the proposed schemes and evaluate their performances, compared with conventional pilot-aided (PA) method. Our proposed methods show comparable performance and much increased spectral efficiency than the PA method.

1.4.3 Modulation format recognition

In this work, we propose a blind modulation format recognition algorithm, applicable to both single-carrier systems and optical OFDM systems. It converts the received data to the Stokes space first, followed by a series of preprocessing procedures. Then the data are converted into a binary graph, based on the density of distribution. Connected component analysis is utilized to count the number of subsets in the final binary image, so as to recognize the modulation format up to 16QAM.

Detailed characterization has been performed to optimize the key parameters in the proposed algorithm. Besides, by taking the advantage of the symmetry of the signal constellation diagram, an improved algorithm is proposed. Simulations and experiments show that it has a significant increase in the OSNR sensitivity and much reduced requirement of the data samples involved in the recognition.

1.5 Outline of this thesis

The remaining chapters of this chapters are organized as follows:

Chapter 2 depicts the background for this thesis research. The physics basis of PMD in single mode fiber and the current schemes for PMD monitoring have been reviewed. Fundamental terminologies and techniques in image processing, like bounding box, convex hull, connected component analysis are discussed in this chapter as well.

Chapter 3 proposes a novel code-correlated scheme for PMD monitoring in an optical OFDM system. The principle and implementation are explained in details. Experimental demonstration of the proposed PMD monitoring scheme has been shown in two different configurations of direct-detection optical OFDM systems. Besides, the feasibility of using a low-cost narrow bandwidth photodiode is investigated and experimentally demonstrated.

Chapter 4 studies how to estimate and compensate the laser phase noise effect in coherent optical OFDM system. A series of image processing techniques have been proposed to recover the common phase error at the receiver. The computation complexity has been well studied. An inter-channel interference cancellation method based on digital equalizer design is also proposed and experimentally investigated in this chapter.

Chapter 5 shows another approach which uses image processing technique in the digital signal processing part to realize a new blind modulation format recognition algorithm. It is verified by both numerical simulation and experiment. The detailed principle and algorithm design together with the performance optimization are also described.

Chapter 6 gives the summary of this thesis and suggests the potential future work.

Chapters 2 Background

This thesis research aims at subsystem innovation for the optical OFDM-enabled software-defined network. We have proposed a PMD monitoring scheme for DDO-OFDM system at the intermediate nodes of the network, a set of laser phase noise estimation and compensation methods for CO-OFDM at the coherent receiver, and novel modulation format recognition algorithms for both single-carrier and multi-carrier optical systems. In this chapter, we give the background of these three subsystem design. Especially for the latter two projects, we have made the first attempt, to the best of our knowledge, to use image processing techniques to solve practical problems in fiber-optic communications. Therefore, the background will be discussed comprehensively, to aid the understanding of this thesis. In each following section of this chapter, we consider the origin of the problem, the current schemes, and the fundamental background of the methods we have used.

2.1 PMD monitoring in optical OFDM system

2.1.1 PMD representation in time domain and frequency domain

PMD derives from the birefringence of optical fiber. Two orthogonally polarized *HE*-11 modes travel at different velocities in a single mode fiber, which leads to different arrival times for the two modes. Geometric irregularities of the core or internal stress, as well as fiber bending, twisting and pinching would make contributions to variance in birefringence. Fig. 2.1 illustrates the birefringence effect of single mode fiber in the time domain. Due to inequality of equivalent refractive indices for the two orthogonal polarization modes, the pulse width of the optical signal will be broadened after fiber transmission. The difference in their group delays is defined as differential group delay (DGD) and PMD is defined as the average of DGD along the fiber length [45]. DGD is frequency dependent, thus the PMD effect in each channel of wavelength division multiplexing (WDM) system has slight difference.

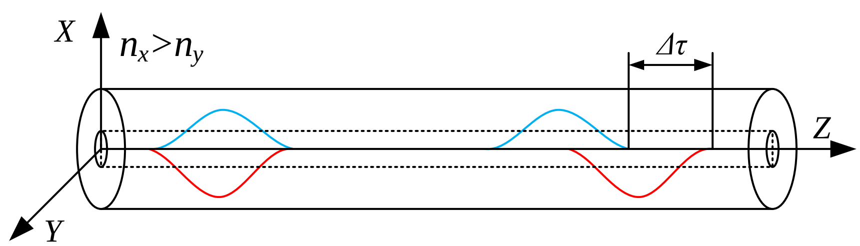

Fig. 2.1 Principal state of polarization (PSP) and differential group delay ($\Delta\tau$). n_x and n_y are the refractive indices along each PSP, respectively.

In spite of the random and susceptible property of birefringence, C.D Poole and Wagner found that there are always two orthogonal input states of polarization (SOP) whose corresponding output SOPs exhibit zero dispersion and they are wavelength independent to the first order, at a certain small frequency range [46]. These two orthogonal input states of polarization are defined as the principal state of polarization (PSP).

The above description is the time-domain definition of PMD. Here, we give the frequency definition of PMD as well. The two PSPs are transparent for the frequencies and this effect only applies in a small bandwidth, namely PSP bandwidth. The PSP can be used to define the PMD vector, whose amplitude is the DGD and its orientation is the same as that of the fast axis of the PSP. PMD vector describes how an output polarization state changes with frequency as a precession around the PMD vector for a fixed input polarization, which is the fundamental theory in the PMD measurement in the frequency domain [47]. This precession on the change of the polarization state can be expressed as [47]

$$\frac{d\hat{s}_{out}}{d\omega} = \vec{\Omega} \times \hat{s}_{out} \tag{2.1}$$

where $\hat{s}_{out}$ denotes the state of polarization, ω is the angular frequency of the light , and $\vec{\Omega}$ is the PMD vector. As PMD vector varies with the optical frequency, the Taylor-series extension of PMD vector Ω with precession $\Delta\omega$ about the carrier frequency ω_0 is

$$\vec{\Omega}(\omega_0 + \Delta\omega) = \vec{\Omega}(\omega_0) + \frac{d\vec{\Omega}}{d\omega}(\omega_0)\Delta\omega + \cdots \tag{2.2}$$

The first term is called the first order PMD, and the remaining terms are called the higher-order PMDs which give more complicated impact on the system performance as discussed in [48].

2.1.2 PMD-induced power fading

As the SOP of an optical signal rotates dependent on the DGD and frequency, each frequency component (subcarrier) of the optical OFDM signal will have a relative difference in SOP with the optical carrier after fiber transmission. It is not a critical issue in a CO-OFDM system, in which a polarization-diverse coherent receiver is used. However, when only a single-receiver is used to detect the DDO-OFDM signal, the optical carrier and the optical signal will beat, according to the square law of the photodiode detection. The misalignment of the SOPs among the optical carrier and the optical subcarriers creates destructive interference among themselves during the signal beating, which leads to power fading over the entire power spectrum of the detected signal, characterized by (2.3) [49],

$$H\left(\omega_k, \gamma, \Delta\tau\right) = \gamma + \left(1-\gamma\right) e^{-j\omega_k \Delta\tau} \tag{2.3}$$

where γ is the power splitting ratio, ω_k (=2πf_k) is the angular frequency difference between the optical carrier and the k^{th} optical subcarrier residing at frequency f_k. $\Delta\tau$ is the DGD value of the fiber link. In (2.3), if γ equals 0.5, i.e., the input optical signal is equally split into two orthogonal principal states of polarization (PSPs), and using frequency difference instead of angular frequency difference, the DGD gives the highest impact on the optical signal and (2.3) becomes,

$$\left|H\left(f_k, \Delta\tau\right)\right| = \left|\cos\left(\pi f_k \Delta\tau\right)\right| \tag{2.4}$$

The frequency dependent polarization rotation induced by the first-order PMD leads to misalignment of the SOPs between the optical carrier and the data subcarriers, as show in Fig. 2.2(a). Therefore, the electrical spectrum after the photodetector is corrupted by frequency-selective power fading. Fig. 2.2(b) shows the numerical calculation result for Eq.(2.4). DGD value ($\Delta\tau$) ranges from 0 to 100 ps, and f_k ranges from 0 to 40 GHz. A periodic power fading could be clearly seen.

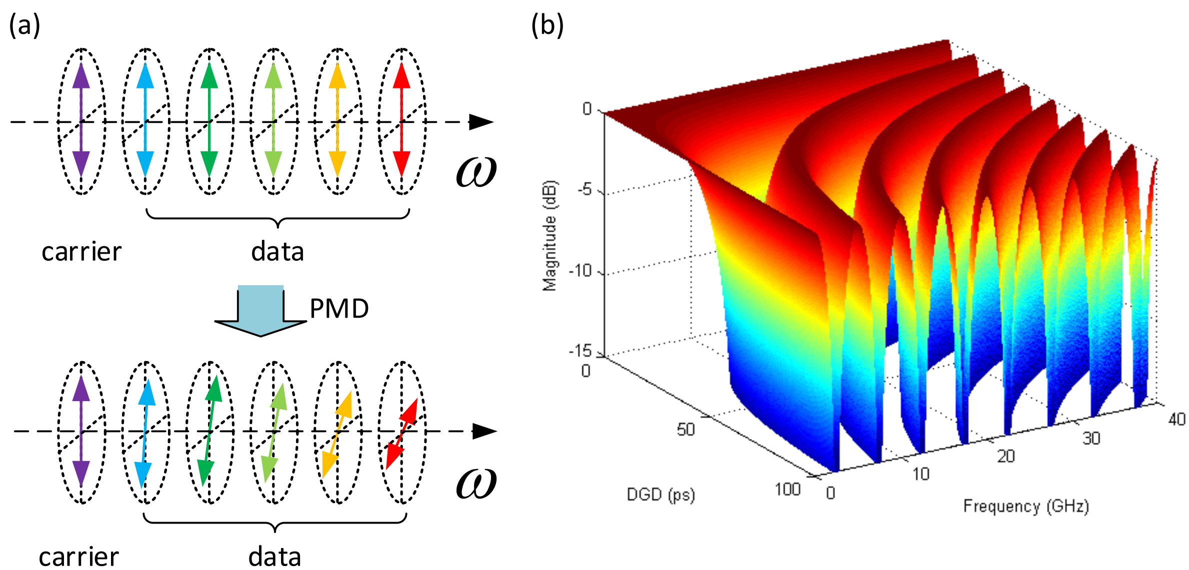

Fig. 2.2 (a) Illustration of frequency dependent SOP rotation due to first-order PMD; (b) Numerical calculation result for the normalized magnitude of channel response under DGD from 0-100 ps for an optical signal with bandwidth of 40 GHz.

2.1.3 PMD induced penalty in fiber communication system

In the direct-detection on-off keying optical system, C.D. Poole et, al. gives an empirical approximation of the penalty of the OSNR sensitivity, given by [50],

$$\text{Penalty(dB)} = 5.1\langle \Delta\tau \rangle^2 / T^2 \tag{2.5}$$

where $\Delta\tau$ is the DGD value and T is symbol duration. From (2.5), it is easy to conclude that the signal with higher data rate is more susceptible to PMD values. It is easy to understand as higher date rate has shorter symbol duration, thus more susceptible to dispersion effect. A numerical calculation result based on this equation is shown in Fig. 2.3.

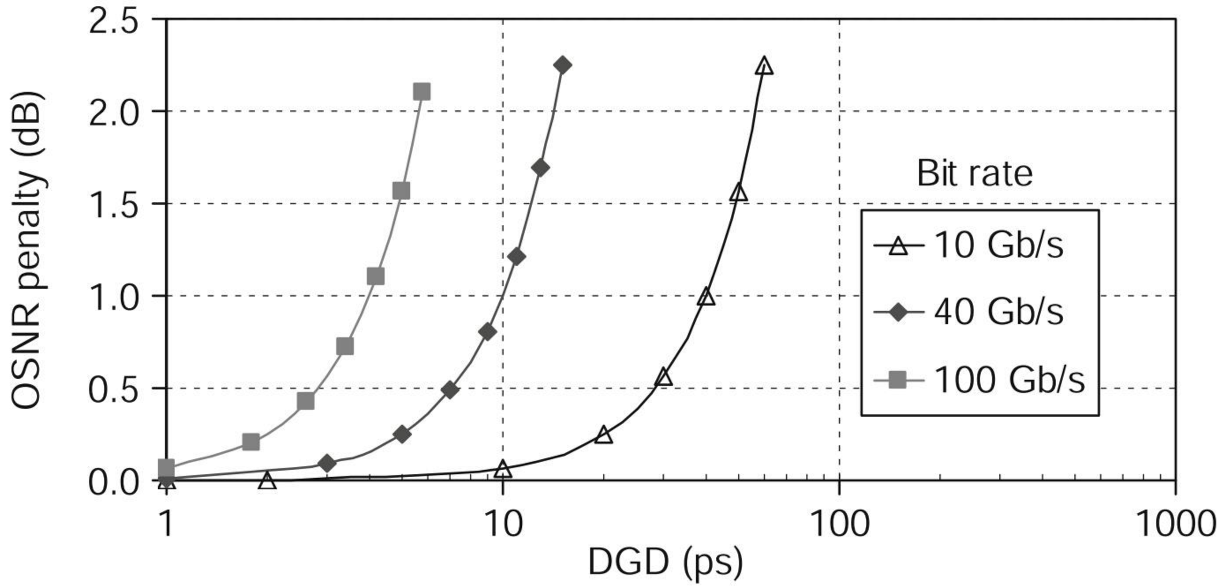

Fig. 2.3 OSNR penalty against DGD for NRZ systems with data rates of 10, 40, and 100 Gbps. [51]

In coherent optical communication systems, especially when polarization multiplexing is applied, the presence of PMD introduces a time delay into the two orthogonal polarization components. Moreover, PMD affects the orthogonality of polarization multiplexing, which results in the crosstalk between the polarizations. Meanwhile, PMD is a frequency-dependent phenomenon, hence complex adaptive equalizers are required in coherent optical communication system to compensate the PMD-induced detriment to the signal [36].

2.1.4 PMD monitoring techniques

Extensive research has been performed in the monitoring schemes of PMD over the past years. In this section, we briefly review several famous PMD monitoring techniques.

As discussed in 2.1.2, PMD induces a frequency selective power fading to the power spectrum in direct-detected optical system. A straightforward PMD monitoring approach was to measure the power fading of certain frequency component. For return-to-zero (RZ) modulation format, there is a strong RF clock tone in the electrical signal spectrum, thus its power can be used to estimate PMD value of the fiber link. To mitigate the monitoring ambiguity introduced by chromatic dispersion induced power fading in the double sideband system, a narrow optical filter could be centered at the clock frequency in one sideband before the photodetector [26]. Non-return-to-zero (NRZ) signal does not have an RF clock tone, but a dispersive fiber Bragg grating can be used to regenerate the RF clock tone [27]. Therefore, the same method could be used in NRZ system to monitor PMD. Other than measuring the power of certain frequency, the PMD could be estimated from the frequency where power notch in the power spectrum [29].

The degree of polarization (DOP), which is defined as the power ratio of the polarized light to the total power of light, could also be used to monitor PMD. The principle is that PMD depolarizes as it induces frequency dependent polarization rotation, thus degrades the DOP. Monitoring PMD in the NRZ [52] and RZ [31] system have been demonstrated. However, the monitoring range of this method was limited by the pulse width.

Asymmetric amplitude histogram (AAH) can also be used to monitor PMD, based on the shape of histogram [22]. However, its monitoring accuracy is susceptible to the interplay of other impairments. To combat this limitation, 2-D delay-tap sampling [23] has been proposed,so as to achieve simultaneously monitoring of several fiber impairments. Meanwhile, both AAH and delay-tap sampling techniques can provide the input information to an artificial neural network (ANN) [35, 53] to achieve more accurate monitoring. ANNs trained with other observations [33, 53] have also been demonstrated to monitor fiber impairments including PMD.

Coherent optical communication can fully compensate CD and PMD using digital filters at the receiver [37]. In this system, the CD and PMD monitoring could be directly read from the fiber coefficients. Low-cost monitoring at the intermediate nodes is the new challenge in this case.

2.1.5 PMD monitoring in optical OFDM system

Although many PMD monitoring schemes have been proposed in the single-carrier system, the research of PMD monitoring in optical OFDM system is still under investigation. And only a limited number of schemes have been proposed. It probably because CO-OFDM has better PMD tolerance [54]. However, the DDO-OFDM system suffers a non-negligible system outage due to PMD [49, 55]. Therefore, PMD monitoring is still necessary in such direct-detected systems.

The first scheme uses channel estimation information at the coherent receiver to estimate first-order PMD value [41]. The magnitude of channel response suffers a periodic fading, whose period's inverse value is proportional to DGD value, as shown in Fig. 2.4. The second approach is still in CO-OFDM system. A coherent receiver with low bandwidth is utilized to calculate the first-order PMD value in the Stokes space. In Poincaré sphere, the state of polarizations of OFDM subcarriers distributes in an arc trace due to frequency-dependent DGD. Therefore, DGD can be derived from the angle relationship between the first and last subcarrier:

$$\Delta\tau = \frac{\Delta\varphi}{2\pi\Delta f} \tag{2.6}$$

where $\Delta\varphi$ is angle, $\Delta\tau$ is DGD value, and Δf is bandwidth of OFDM signal.

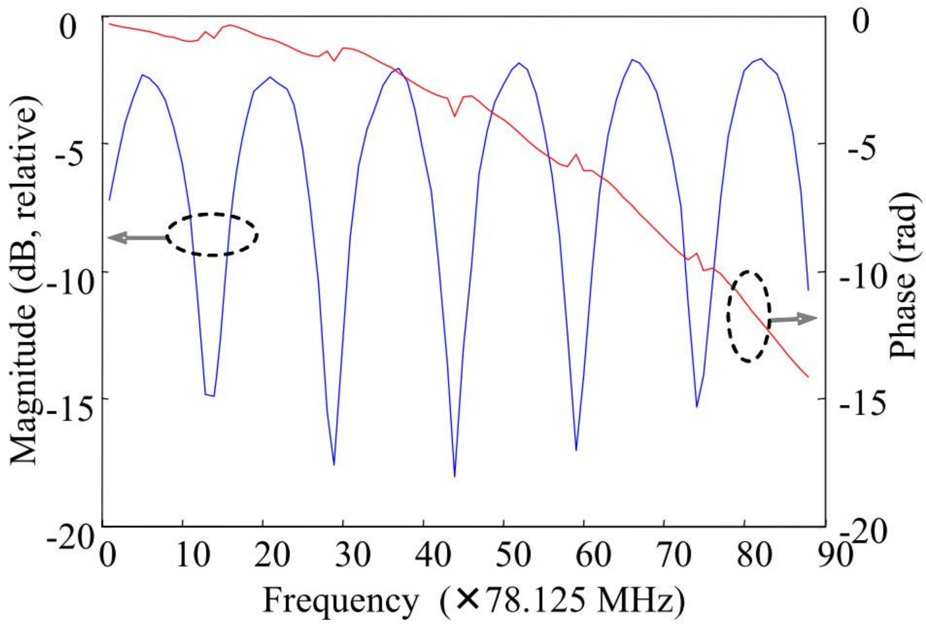

Fig. 2.4 Estimated channel responses for x-polarization cnmponent. The DGD value is set to be 900 ps.[41]

The existing problem for the current PMD monitoring scheme is that they all require a coherent receiver in the monitoring module, which is costly. It limits the large-scale deployment in the optical network. Low-cost PMD monitoring schemes for optical OFDM system are highly desirable.

2.2 Laser phase noise estimation and compensation in coherent optical OFDM system

2.2.1 Laser phase noise model in optical OFDM system

Laser phase noise, which is generated at the lasers located at both transmitter and receiver, is usually modeled as a finite-power Wiener process in both wireless and coherent optical communication systems [56, 57]. In the time domain, phase noise can be treated as an integral of the Gaussian distributed variables [57]:

$$\varphi_k = \sum_{i=-\infty}^{k} f_i \tag{2.7}$$

where f_i is a random Gaussian variable with zero mean and the variance

$$\sigma_f^2 = 2\pi\left(\Delta f \cdot T_s\right) \tag{2.8}$$

where Δf is the laser linewidth and T_s is the symbol duration.

Fig. 2.5 denotes a simplified channel model of a CO-OFDM system. The OFDM signal generated after IDFT is to modulate a continuous wave (CW) light at the modulator. The signal laser introduces a phase noise item to the signal. The OFDM signal is denote by:

$$s(n) = \sum_{k=0}^{N-1} s_k e^{j\frac{2\pi}{N}kn} \tag{2.9}$$

where N is FFT size, k is the subcarrier index.

The signal after modulation is:

$$r(n) = s(n) \cdot e^{j\varphi(n)} \tag{2.10}$$

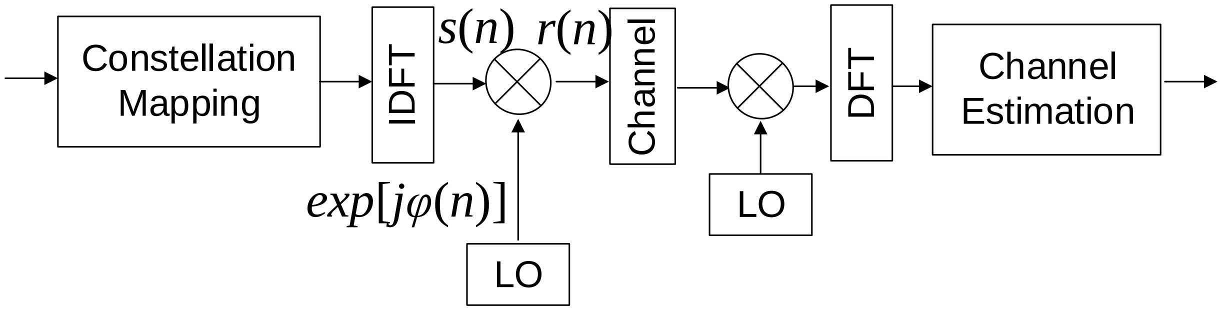

Fig. 2.5 Simplified channel model of a CO-OFDM system. IDFT: inverse discrete Fourier transform; DFT: discrete Fourier transform; LO: local oscillator.

Assume an ideal channel and the phase noise from local oscillator is also denoted by $\varphi(n)$. The signal after FFT at the receiver is:

$$\begin{aligned} y(k) &= \frac{1}{N}\sum_{m=0}^{N-1} r(m)\cdot e^{-j\frac{2\pi}{N}km} \\ &= \frac{1}{N}\sum_{m=0}^{N-1} e^{j\varphi(m)} \sum_{r=0}^{N-1} s_r e^{j\frac{2\pi}{N}rm} e^{-j\frac{2\pi}{N}km} \\ &= \frac{1}{N}\sum_{m=0}^{N-1} e^{j\varphi(m)} \sum_{r=0}^{N-1} s_r e^{j\frac{2\pi}{N}(r-k)m} \\ &= \frac{1}{N}\sum_{r=0}^{N-1} s_r \sum_{m=0}^{N-1} e^{j\varphi(m)} e^{j\frac{2\pi}{N}(r-k)m} \end{aligned} \tag{2.11}$$

If small phase noise assumption applies, i.e.,

$$e^{j\varphi(m)} \approx 1 + j\varphi(m) \tag{2.12}$$

(2.11) becomes:

$$\begin{aligned} y(k) &\approx \frac{1}{N}\sum_{r=0}^{N-1} s_r \sum_{m=0}^{N-1} e^{j\frac{2\pi}{N}(r-k)m} + \frac{j}{N}\sum_{r=0}^{N-1} s_r \sum_{m=0}^{N-1} \varphi(m) e^{j\frac{2\pi}{N}(r-k)m} \\ &= s_k + \frac{j}{N}\sum_{r=0}^{N-1} s_r \sum_{m=0}^{N-1} \varphi(m) e^{j\frac{2\pi}{N}(r-k)m} \\ &= s_k + c_k \end{aligned} \tag{2.13}$$

Dependent on whether r equals k or not, there are two types of phase noise effect on the received data in OFDM system.

In the first case, $r = k$, we have:

$$c_k = \frac{j}{N}\sum_{r=0}^{N-1} s_r \sum_{m=0}^{N-1} \varphi(m) = j\frac{s_k}{N}\sum_{m=0}^{N-1} \varphi(m) = j \cdot s_k \cdot \Psi \tag{2.14}$$

A common phase error Ψ is added to every subcarrier. It results in a rotation of the constellation of this OFDM symbol, known as common phase error (CPE).

In the second case, $r \neq k$, we have:

$$c_k = \frac{j}{N}\sum_{r=0}^{N-1} s_r \sum_{m=0}^{N-1} \varphi(m) \cdot e^{j\frac{2\pi}{N}(r-k)m} \tag{2.15}$$

A complex number is added to each subcarrier, which has a similar appearance of white noise. It is known as inter-carrier interference (ICI). Note that the small phase assumption could be removed based on the simulation result in [58] and the aforementioned phase noise model in OFDM systems is applied to any phase noise value.

Fig. 2.6 shows the simulation result for a QPSK-OFDM signal, and only laser phase noise is considered in the channel model. In the constellation diagram of data samples in one received

OFDM symbol, we can clearly see the effect of laser phase noise: CPE induces a common rotation of the constellation, while ICI is responsible for the enlargement of the constellation points.

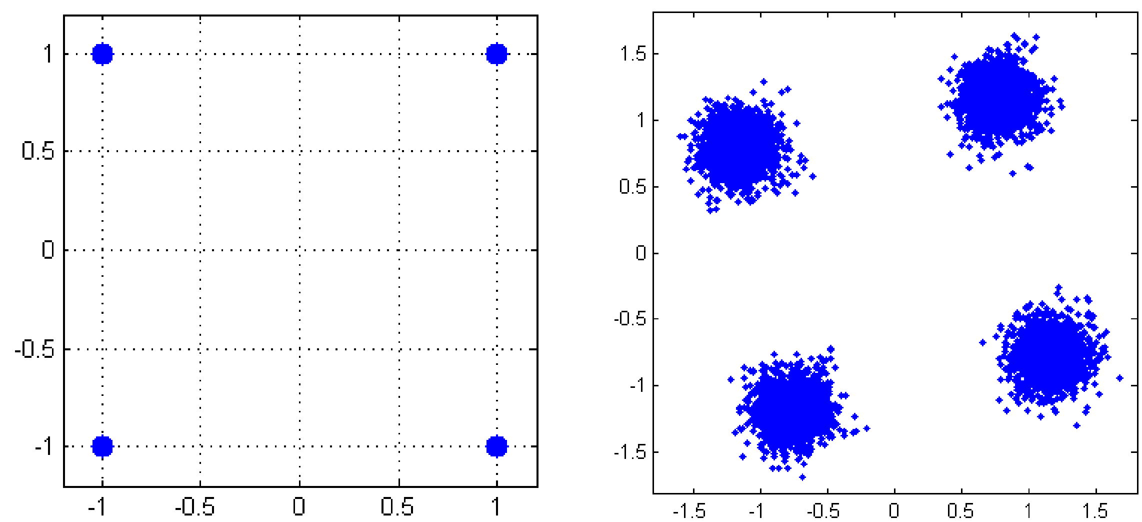

Fig. 2.6 Constellation of QPSK-OFDM signal before modulation (left) and the simulation result of received signal (right), in which only laser phase noise is considered.

2.2.2 Previous laser phase noise compensation schemes

The most widely used common phase error compensation method is the well-known pilot-aided (PA) method [59], in which part of the subcarriers are modulated with pilot data. The phases of the data in these pilot subcarriers are checked at the receiver after FFT, and the phase changes are averaged among the pilot subcarriers to alleviate the degradation of accuracy due to the white noise in the system. Fig. 2.7 shows the pilot subcarriers' alignment in the frequency domain for the PA method.

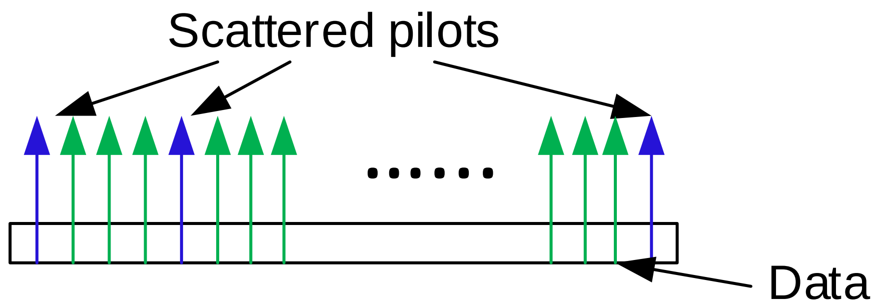

Fig. 2.7 Illustration of pilot subcarriers design in the pilot-aided CPE estimation method.

Data-aided (DA) is another approach to estimate the common phase error [59]. For CO-OFDM with QPSK mapping in each subcarrier, the data modulation can be removed by *M*-th power-law method [60]. After removing the data modulation, it remains only the common phase error as well as the Gaussian noise. Averaging can also help to alleviate the noise influence, so as to increase the accuracy. The operation can be written as

$$\varphi_i = \frac{1}{N}\sum_{k=0}^{N-1}\left\{\arg\left(y_{ik}^{M}\right)/M\right\} \tag{2.16}$$

where N is the number of subcarriers, arg(.) is the phase of a symbol, M = 4 for QPSK. Decision direct and differential coding can be used to remove the ambiguity introduced by *M*-th power [59].

PA method has better performance both in simulation and experiment, as shown in [59]. Meanwhile, PA method has the least computation resource requirement. However, the reduction of spectral efficiency is the main drawback of PA method, as it inserts the pilot subcarriers in every OFDM symbol.

Another commonly used method in optical OFDM is the RF-tone aided method. It inserts an RF tone at the lower frequency before up-conversion, and uses either narrow electrical filter

[61] or optical filter [62] to get the RF tone at the receiver. It has better performance than PA method and DA method, especially when laser linewidth is larger. It is because it compensates not only the common phase error but also the ICI effect. However, it requires narrower filter, and several subcarriers around the inserted RF tone are usually padded with zeros for protection, thus also decreasing the spectral efficiency.

In addition to these commonly used methods, many novel methods have been proposed these years. In [63], Le et al, proposed to insert quasi pilot-aided subcarriers, which are symmetrically distributed among the positive and negative subcarriers. These quasi-pilots design can also help to mitigate fiber nonlinearity effect in CO-OFDM systems [64]. To compensate the reduction in spectral efficiency of PA method, [65] modulates the pilot subcarriers with pulse amplitude modulation format. As the initial phase of data in these pilots is zero, the receiver can recover the common phase error based on the exact phase of these subcarriers. The benefit is that it does not decrease the spectral efficiency. Blind common phase error estimation based on constant amplitude modulation [66] and non-data-aided approach using decision-direct method for phase recovery [67] are also proposed.

There is no much research on ICI mitigation in CO-OFDM systems. In [68], the subcarriers are designed in pairs with Hermitian symmetry. At the receivers, the residual phase noise after digital coherent superposition is much smaller than ICI. Interpolation of the common phase error in sub-symbols in one OFDM symbol has been demonstrated as a simple and effective ICI mitigation method [69]. By carefully designing a matched filter, the ICI and common phase error can be compensated simultaneously at the receiver [70]. Besides, orthogonal basis expansion has also demonstrated as an effective tool in the compensation of laser phase noise in CO-OFDM system [71-73].

2.2.3 Bounding box

In geometry, the bounding box is defined as the smallest box within which all the points lie. According to the direction of box, there are two types of bounding box, named by axis-alignment bounding box and best-fit bounding box, as depicted in Fig. 2.8. The former's edges are parallel to the Cartesian coordinate axes, while the latter one is arbitrarily oriented and covers all the points with the minimum area as well as maintaining the rectangular shape.

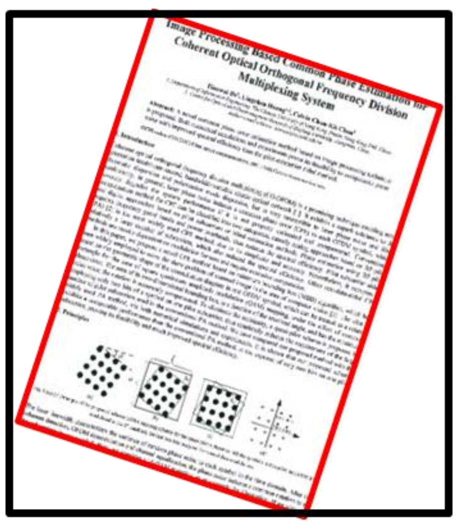

Fig. 2.8 Two types of bounding box of an image: axis-aligned bounding box (black) and best-fit bounding box (red).

The axis-aligned bounding box is often used as a coarse location of an object, as it requires very little computation to obtain. To find the axis-aligned bounding box of a set of points in the 2-D plane, it only needs to find the minimal and maximal values of the data in the two coordinate axes.

In the meantime, the best-fit bounding box (BBB) offers more information than axis-aligned bounding box, as its leaning angle can tell the approximate skew of the object it covers. However, it takes more computation effort to calculate the best-fit bounding box of a set of points. A widely used algorithm to find the best-fit bounding box is called Rotating Calipers algorithm [74], as its implementation is similar to using a rotating caliper to measure the length of an object.

The convex hull of the points set should be obtained first before applying the Rotating Calipers algorithm. In mathematics, the convex hull of a given point set X_i in the 2-D plane is the smallest convex set that contains X_i. In a graphic view, convex hull is the minimum convex polygon that contains all the points. Fig. 2.9 illustrates the calculation of convex hull of a given set of points. The final points in the rightmost figure in Fig. 2.9 is the convex hull of the points in the leftmost figure.

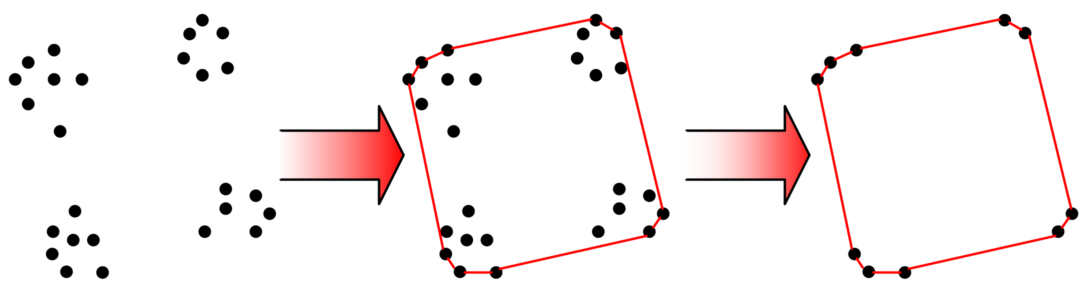

Fig. 2.9 Convex hull.

There is an import theorem showing the smallest enclosing rectangle of the polygon has a side collinear with one of the edges of its convex hull [75], which provides the theoretical foundation for the Rotating Calipers algorithm. In the Rotating Calipers algorithm, each edge of the convex hull is gone through. The convex hull is first rotated, such that one edge is along a major axis, say x-coordinate. It is now an axis-aligned bounding box, whose area can be calculated easily by the product of the length of edges. Fig. 2.10 shows the implementation of Rotating

Calipers algorithm. After traversing all the edges, the minimum area is selected and then the best-fit bounding box is obtained.

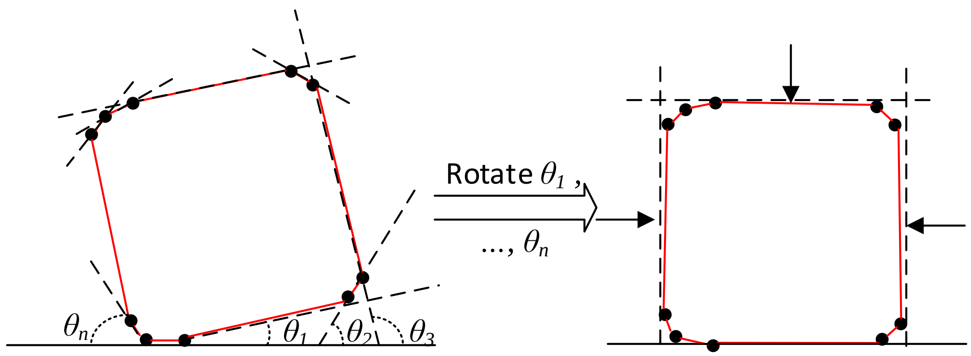

Fig. 2.10 Illustration of Rotating Calipers algorithm.

The last thing is how to calculate the convex hull for given points set in 2-D plane. A lot of research has been put in the efficient calculation of convex hull, because of its wide application in computer vision. The Graham Scan algorithm [76], the Quickhull algorithm [77], and the Chan's algorithm [78] are popular algorithms in this area.

Here we give a brief introduction of Graham's algorithm, which could run in $O(n\log n)$ time, where n is the number of points. There is an initial radial sorting process which needs a so-called "is-left" decision to decide the whether one point is in the counter-clock or clock-wise direction of the line determined by the origin and previous point. The "is-left" relationship is obtained by a determinant:

$$\Delta = (x_2 - x_1)(y_3 - y_1) - (y_2 - y_1)(x_3 - x_1) \tag{2.17}$$

which is actually the cross product of the vector $\overrightarrow{P_1P_2}$ and $\overrightarrow{P_1P_3}$. The relationship with respect to the cross product is

$$\begin{cases} \Delta > 0, \text{ left} \\ \Delta = 0, \text{ collinear} \\ \Delta < 0, \text{ right} \end{cases} \tag{2.18}$$

This "is-left" process consists of 5 real additions and 2 real multiplications. The first scan sorts all the points in counter-clock direction. In the second scan, each point is checked to determine whether it is the convex hull, via the same "is-left" operation.

If the expected output size of convex hull is pre-known, say h, the complexity can be reduced to $O(n\log h)$ by Chan's algorithm [78]. It has been demonstrated as the optimal algorithm for the convex hull calculation.

2.3 Modulation formats recognition in coherent optical transmission system

In digital communication, modulation format recognition is an important intermediate processing step between detection and demodulation, and blind recognition is a vital function in software defined radio (SDR) system [79]. Nowadays, optical network is developing towards software-defined manner, thus a general coherent is highly required to cope with the variety of modulation formats. Usually, supplement information can be transmitted together with data or in the separate channel to reconfigure the general-purpose coherent receiver. This approach is simple but at the expense of transmission efficiency. On the other hand, blind modulation format has great significance in reducing overhead thus increasing spectral efficiency.

2.3.1 Modulation format recognition methods in coherent optical communication system

The first report of modulation format recognition in optical transmission systems is in 2010 [80]. Cognitive digital receiver utilizing K-means algorithm to recognize QPSK, 8PSK and 16QAM was proposed for burst mode phase modulated radio over fiber links. The core technique was K-means clustering algorithm [81], which is a fundamental clustering algorithm in machine learning.

A blind modulation recognition method which is conducted in the time domain was proposed in [82]. The higher-order statistics (HOS) of the polarization demultiplexed signal was calculated and used as an estimator for different modulation format.

In [83], physical layer characteristics of PSK and NRZ signals were used to identify the modulation format, in which the characteristics of the received data's histogram was analyzed. However, it can only recognize simple modulation formats such as OOK, BPSK and QPSK. Another approach which is based on physical layer characteristics and use artificial neural network [84], was also proposed. It could support the successful recognition up to 16QAM. The main drawback is the heavy training load, as fiber impairments like CD and PMD, and OSNR of optical signal, all need to be trained previously.

In [85], the power distribution of the signal after polarization demultiplexing but before frequency offset and carrier phase recovery was proposed. It had small computation load in the recognition process, but the power ratio it used is sensitive to the signal's OSNR. Hence, an external OSNR monitoring module was required in the practical implementation [86].

A series of machine-learning based autonomous modulation methods have been proposed [87, 88]. They were implemented in Stokes space, by which no polarization demultiplexing, frequency offset estimation and carrier phase recovery were required. The performance of several clustering algorithms, i.e., K-means [81], expectation maximization [89], DBSCAN [90], OPTICS [91] and spectral clustering [92] have been evaluated in [88].

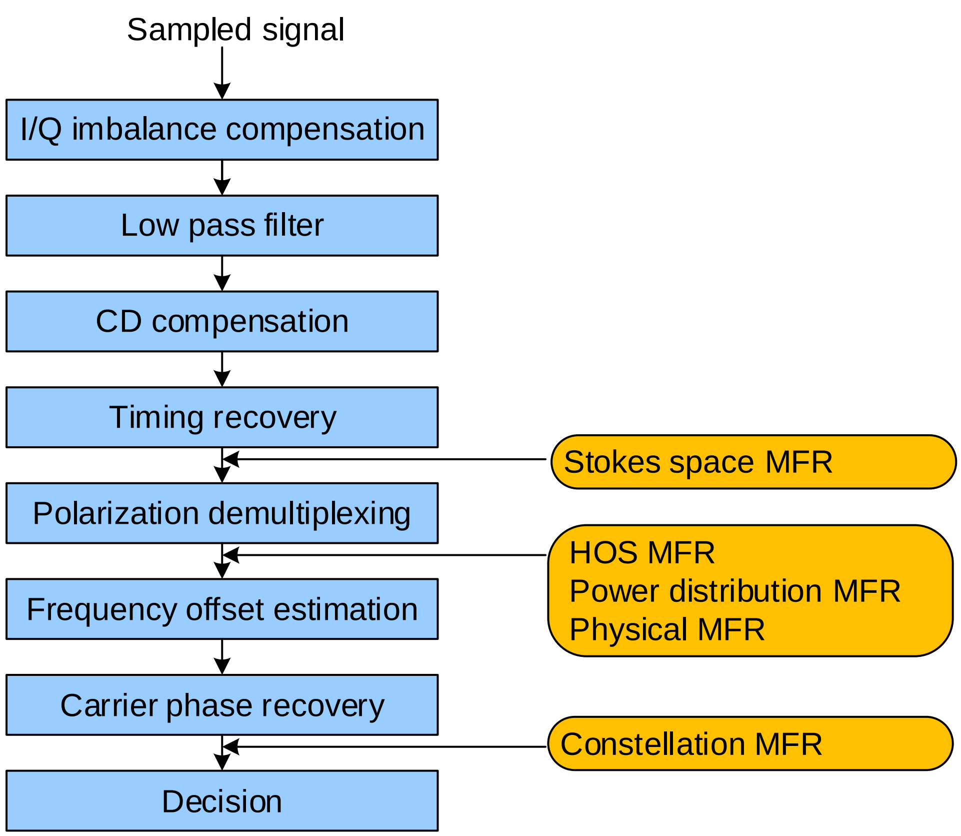

Fig. 2.11 Locations in the receiver DSP process for MFR algorithms

Fig. 2.11 shows the locations in the receiver DSP process where MFR is performed for the above-mentioned algorithms. Obviously, it is better to have modulation format successfully recognized in as early stage as possible, so that the optimal subsequent DSP algorithms can be chosen for specific modulation format. In this way, Stokes space MFR is most advantageous.

2.3.2 Background of using image processing techniques in blind modulation format recognition

Some basic terms like bounding box, convex hull, and skew detection have been discussed in the previous section, where we use these techniques to solve the constellation rotation problem induced by laser phase noise. In this section, we discuss several background concepts, for the image processing techniques based modulation format recognition algorithm, such as Voronoi diagram, averaging filter, and connected component analysis. First of all, the Stokes representation of optical signal is explained.

Stokes representation of optical signal

To represent an optical field in single mode fiber, there are two principle manners, namely the Jones and Stokes representations. In the Jones space, a two-element complex vector is used to represent polarized light.

$$\vec{E} = \begin{pmatrix} \overrightarrow{E_x} \\ \overrightarrow{E_y} \end{pmatrix} = \begin{pmatrix} E_{0x} e^{i\delta_x} \\ E_{0y} e^{i\delta_y} \end{pmatrix} \tag{2.19}$$

where E_{0x} and E_{0y} represent the maximum amplitudes and δ_x and δ_y denote the phases. In (2.19), there are two orthogonal states of polarization and each polarization is a complex optical field, so there are 4 degrees of freedom in total in Jones representation. The Jones representation allows calculation of the interference effects and in some cases provids a simpler description of optical physic [93].

The problem of Jones representation is that it is not convenient to measure the electric field of optical signal directly, especially when dealing with partially polarized light. For this reason, Stoke representation has been developed to represent the polarization in term of easily measured optical powers. In the Stokes space, four parameters which can be measured by the corresponding intensities are used as coordinates to describe optical polarizations.

$$\left[s_0, s_1, s_2, s_3\right]^T \tag{2.20}$$

In Eq. (2.20), s_0 is the total power which consists of both polarized and unpolarized light, s_1 is the power through a linear polarizer, s_2 is the power through left 45-degree polarizer, and s_3 is the power though right circular polarizer. s_0 is not an independent parameter, as it can be obtained by the rest three parameters by

$$s_0 = \sqrt{s_1^2 + s_2^2 + s_3^2} \tag{2.21}$$

Therefore, the total degree of freedom in Stokes is three. The Stokes vector of an optical signal can always be derived from its Jones representation by

$$\begin{bmatrix} s_0 \\ s_1 \\ s_2 \\ s_3 \end{bmatrix} = \begin{bmatrix} \left|E_x\right|^2 + \left|E_y\right|^2 \\ \left|E_x\right|^2 - \left|E_y\right|^2 \\ 2\Re\left\{E_x E_y^*\right\} \\ 2\Im\left\{E_x E_y^*\right\} \end{bmatrix}^T \tag{2.22}$$

Now that we have the Stokes representation of an optical signal, it is easy to visualize the state of polarization (SOP) in the Poincaré sphere. As seen in Fig. 2.12, each point in the surface of Poincare sphere represents a SOP of optical signal. These SOPs can be denoted by either [S_1 S_2 S_3] in Cartesian coordinates or [Ip χ ψ] in polar coordinates.

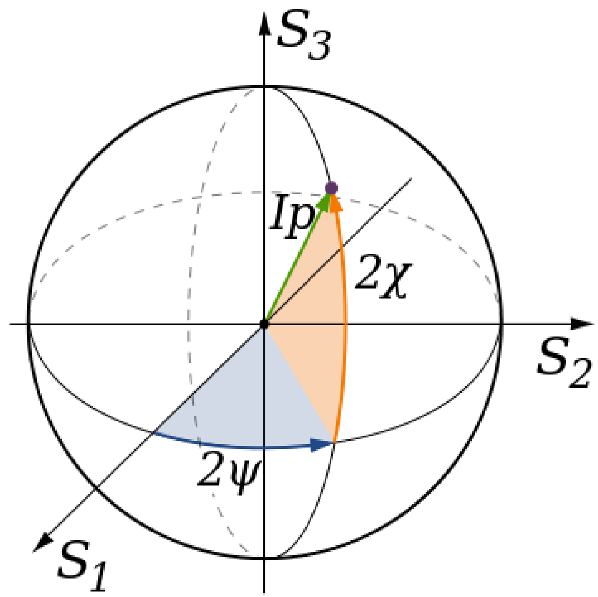

Fig. 2.12 Poincaré sphere.

One conclusion that could be derived from Eq.(2.22) is that the phase noise which applies on x- and y-polarization simultaneously can be removed in the conversion from Jones space to Stokes space. This conclusion is quite important as it provides an inherent tolerance to the phase noise in Stoke space, which is very useful for monitoring [94].

Voronoi diagram

Voronoi diagram is a partitioning of a plane into regions based on the distance to the points in a specific subset of the plane. Each point in Voronoi diagram is called seed or site. For each seed, there is a corresponding region consisting of all points closer to that seed than to any other. These regions are called Voronoi cells. Fig. 2.13 shows the example for Voronoi diagram of a set of planar points. Different colors are filled in Voronoi cells to make them easier to identify. For each specific point (named “seed”) in a point set, we can find such a polygon, that all the points inside this polygon are closer to this seed other than any other seeds.

To calculate the Voronoi diagram from a given data set, Fortune's algorithm [95] can be used, which can achieve a time complexity of $O(n\log n)$, where n is the number of total points. The detailed description of the Fotune's algorithm is shown in Chapter 5.

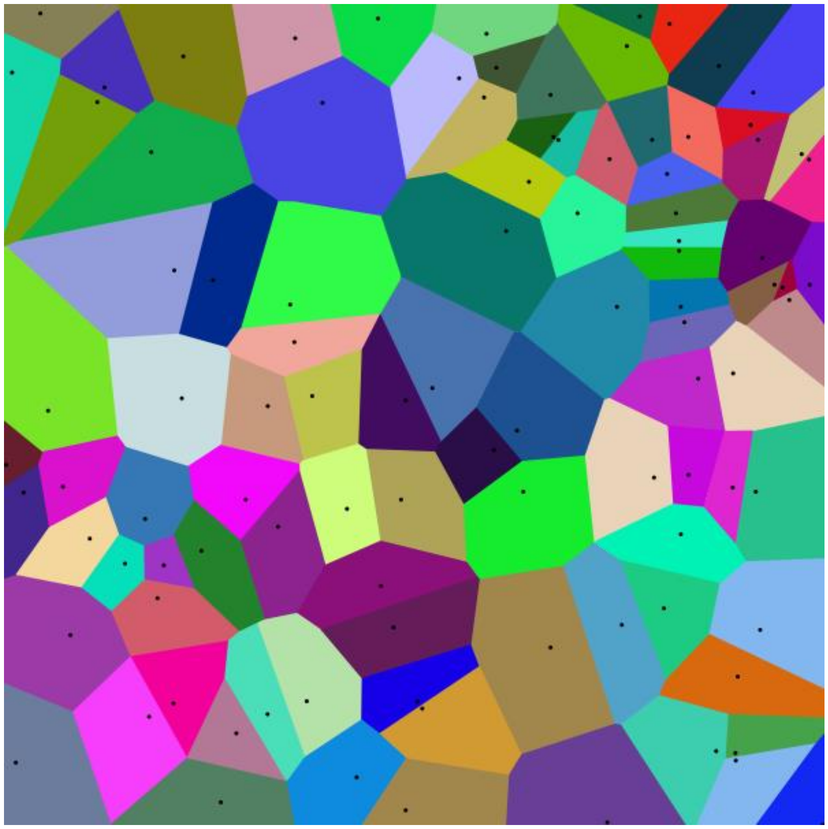

Fig. 2.13 Voronoi diagram. [96]

Averaging Filter

An averaging filter is a simple bi-directional smoothing filter in a binary graph. It is implemented by a 2-dimentional convolution operation. In mathematics, the 2D convolution of matrix ***a*** and ***b*** is defined by

$$c(n_1, n_2) = \sum_{k_1=-\infty}^{\infty} \sum_{k_2=-\infty}^{\infty} a(k_1, k_2) b(n_1 - k_1, n_2 - k_2) \tag{2.23}$$

where k_1,k_2,n_1, and n_2 are the indices of a matrix.

In the averaging filter, the coefficient matrix consists of all ones, with size $\boldsymbol{n}$.

$$coeff = \begin{bmatrix} 1 & \cdots & 1 \\ \vdots & \ddots & \vdots \\ 1 & \cdots & 1 \end{bmatrix} \tag{2.24}$$

The binary image is first enlarged with a guard size by adding zeros around the image. Then it is reversed, followed by 2D convolution with the coefficient matrix. After the convolution, if there is any value in the convolution output smaller than $\boldsymbol{n}\times\boldsymbol{n}$, the corresponding pixels in the binary image will be assigned with 0. That is why we need to added protected area around the original image. After the filtering, the protected area is removed and the image is reversed back.

Connected component analysis

In image processing, connected component analysis (CCA), also named as connected component labeling is to find and mark all the connected region in an image. There are two kinds of connectivity, namely 4-connectivity and 8 connectivity, based on how many pixels are connected.

$$N_4(p) = \{(x \pm 1, y), (x, y \pm 1)\} \tag{2.25}$$

$$N_8(p) = N_4 \cup \{(x \pm 1, y+1), (x \pm 1, y-1)\} \tag{2.26}$$

Eq.(2.25) and Eq.(2.26) give the definition of 4- and 8- connectivity, respectively. Fig. 2.14 illustrates the concepts. In the former definition, 2, 4, 6, and 8 are connected with 5, while 1, 3, 7, and 9 are not. However, the latter definition extends the connectivity to all the surrounded 8 pixels.

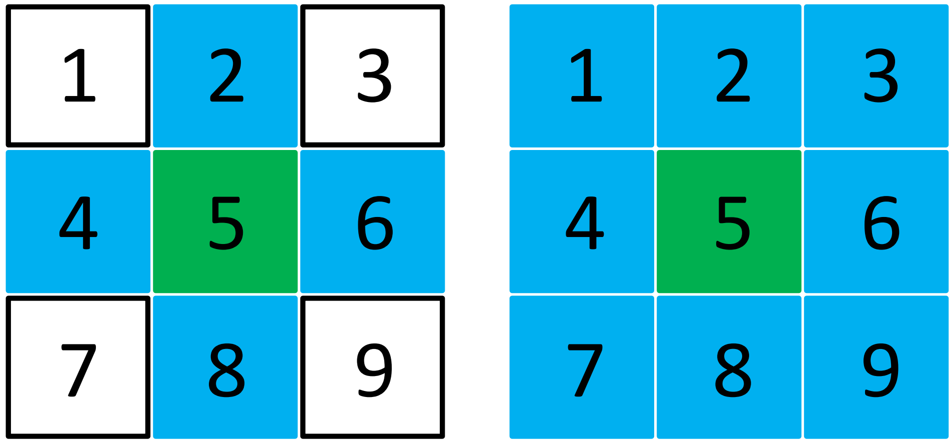

Fig. 2.14Four-connectivity (left) and eight-connectivity (right).

Connected component analysis has many applications in computer vision, such as, optical character recognition, moving object separation and detection, etc. To label out all the connected area in an binary image, it can be easily implemented in $O(n)$ time. Here we briefly give an example named by “Two-pass” algorithm.

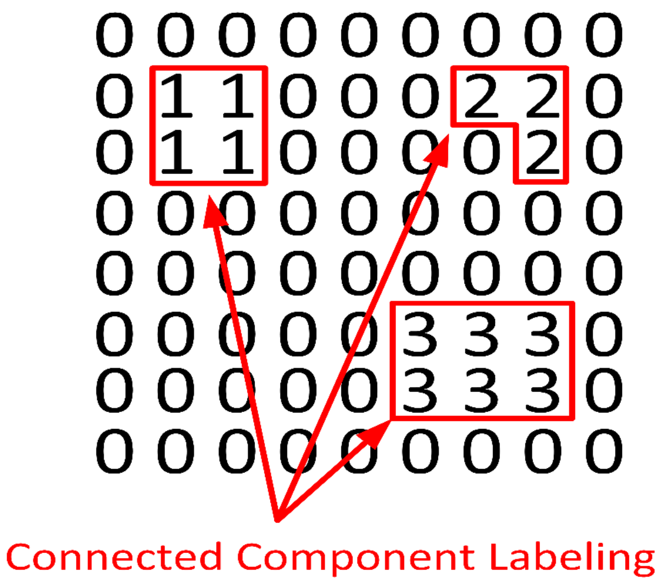

Fig. 2.15 Conneced component analysis (labeling)

Table 2.1 Two-pass algorithm

```
Load the binary image to memory
First scan:
for each pixel B(x,y) in binary image do
    Access B(x,y), if B(x,y)  == 1
    If all neighbor pixels of B(x,y) are 0
        Label += 1, B(x,y) = label
    Else if there is neighbor whose label > 1
        B(x,y) = min{Neighbors}
        Record the equality of labels of neighbors
        labelSet[i] = {label_m, ..., label_n}
    End if
End for
Second scan:
for each pixel B(x,y) in binary image do
    Access B(x,y), if B(x,y) > 1
    find the minimum of label value in all label = B(x,y)
    B(x,y) = min_label
End for
```

Chapters 3 Polarization Mode Dispersion Monitoring in optical OFDM System

3.1 Introduction

Recently, flexible optical network has been widely recognized as a promising approach to support future high-speed heterogeneous data traffic [15]. Optical orthogonal frequency division multiplexing (OFDM) is one of the feasible candidates to enable such flexible network, for its flexible bandwidth and high spectral efficiency [16]. To date, there are two mainstreams of optical OFDM systems, in terms of the signal detection technique, namely coherent optical OFDM (CO-OFDM) [2] and direct detection optical OFDM (DDO-OFDM) [1]. In medium/short distance transmission, such as metro/access networks, DDO-OFDM is more preferred because of its low requirement for transmitter's laser linewidth [97]. It employs a cost-effective photodiode, instead of expensive coherent receivers, to achieve high speed transmission, though at certain expense of sensitivity. As reported in [98], super-channel DDO-OFDM with 432-Gb/s, 3040-km single mode fiber transmission has been experimentally demonstrated, highlighting the good potential of DDO-OFDM even in long haul transmission.

However, DDO-OFDM suffers from a critical drawback of power fading induced by the chromatic dispersion (CD) and polarization mode dispersion (PMD) of the fiber link, due to the square-law of photodiode. Generally, the frequency-dependent power fading reduces the signal power of the optical subcarriers at higher frequencies, and this degrades the performance of DDO-OFDM system [13]. Single side band (SSB) modulation can remove the power fading induced by chromatic dispersion [99] but does no help to the PMD-induced power fading. Moreover, simulations have shown that PMD induces significant performance degradation in optical OFDM system with commonly used single polarization photodiode [100]. Therefore, monitoring of the PMD is indispensable in DDO-OFDM based flexible optical networks. In order to assure the quality of the optical OFDM signals over an optical network, low-cost and effective in-line optical performance monitoring (OPM) techniques are highly desirable to be incorporated at the intermediate network nodes, such that the network control plane can be kept updated of the optical signal quality, for the subsequent compensation.

In this chapter, we studies a low-cost implementation of PMD monitoring scheme for DDO-OFDM system.

3.2 Principles

3.2.1 PMD induced power fading

The principle and effect of PMD induced power fading have been discussed in detail in section 2.1.2. In this section, we start from the following channel response:

$$\left|H\left(f_k,\Delta\tau\right)\right| = \left|\cos\left(\pi f_k \Delta\tau\right)\right| \tag{3.1}$$

where $\Delta\tau$ is the DGD value of the fiber link, f_k is the frequency difference between the optical carrier and the k^{th} subcarrier. Fig. 3.1 depicts the frequency response derived from Eq.(3.1), in which the electrical spectrum after power-law detector is corrupted by a frequency-selective power fading. The first frequency dip occurs at $f_k = 1/2\Delta\tau$.

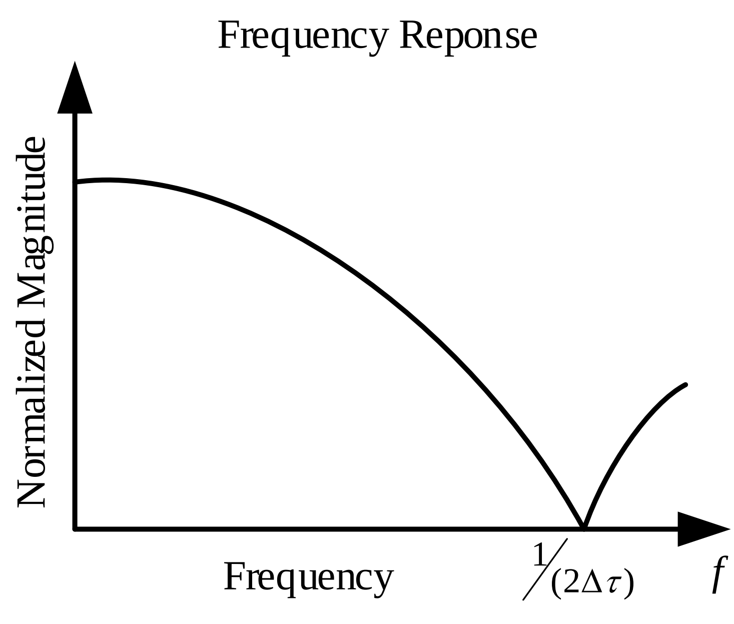

Fig. 3.1 Channel response of the PMD induced power fading characterized by (3.1).

3.2.2 Correlation based power estimation

In a DDO-OFDM system, data can be freely modulated onto a certain optical subcarrier. Two distinct pilot sequences are loaded to the first and the last subcarrier of the OFDM signal, respectively, via inverse fast Fourier transform (IFFT). If the IFFT size is N, that is, there are N samples in one OFDM symbol, the OFDM symbol in time domain can be expressed, as follows:

$$s(n) = \frac{1}{N}\sum_{k=1}^{N} S(k) e^{j2\pi\frac{k}{N}\cdot n} \tag{3.2}$$

where $S(k)$ is the information carried on the k^{th} subcarrier of the OFDM symbol. Consider the i^{th} subcarrier in the m^{th} OFDM symbol is loaded with a designated pilot data $C(m)$, that is, $S_m(i) = C(m)$. $C(m)$ can be regarded as a pilot subcarrier. At the receiver, we generate a pilot signal $c(n)$, which is generated by padding all the subcarriers to be zero except the i^{th} subcarrier set to be $C(m)$. The time domain expression of the pre-defined sequence is:

$$c_m(n) = \frac{1}{N} C(m) e^{j2\pi \frac{i}{N} \cdot n} \tag{3.3}$$

For M OFDM symbols, by applying signal correlation procedure between the OFDM signal, $s(n)$, and the regenerated pilot sequence, $c(n)$, the maximum correlation value is calculated, as follows:

$$\begin{aligned}
R_{\max} &= \sum_{m=1}^{M} \frac{1}{N^2} \sum_{n=1}^{N} s_m^*(n) c_m(n) \\
&= \sum_{m=1}^{M} \frac{1}{N^2} \sum_{n=1}^{N} \sum_{k=1}^{N} S_m(k)^* e^{-j2\pi \frac{k}{N} \cdot n} C(m) e^{j2\pi \frac{i}{N} \cdot n} \\
&= \sum_{m=1}^{M} \frac{1}{N^2} \left(\sum_{n=1}^{N} S_m(i)^* e^{-j2\pi \frac{k}{N} \cdot n} C(m) e^{j2\pi \frac{i}{N} \cdot n} \right. \\
&\quad \left. + \sum_{n=1}^{N} \sum_{\substack{k=1 \\ k \neq i}}^{N} S_m(k)^* e^{-j2\pi \frac{k}{N} \cdot n} C(m) e^{j2\pi \frac{i}{N} \cdot n} \right)
\end{aligned} \tag{3.4}$$

The second term in Eq.(3.4) will become zero, as arbitrary two subcarriers are orthogonal. With $S_m(i) = C(m)$, the maximum correlation value of M OFDM symbols is

$$R_{\max} = \frac{1}{N} \sum_{m=1}^{M} \left| C(m) \right|^2 \tag{3.5}$$

which corresponds to the average power of the pilot data sequence $C(m)$, loaded at the i^{th} subcarrier. This shows the feasibility of using the peak magnitude of the pilot correlation result to estimate the power of a certain frequency component. As the amplitude response for all the subcarriers is quite constant with time, except for the random fluctuations caused by the ASE noise [99], averaging over several OFDM symbols makes the power estimation result more accurate.

3.2.3 PMD Monitoring

Owing to the relatively flat power spectrum of the input optical OFDM signal, such cosine-like PMD-induced power fading would be imposed over the whole signal's spectrum. Hence, the DGD value of fiber can be derived from the spectrum, which is of the cosine function, as in Eq.(3.1). To derive the DGD value $\Delta\tau$, at least the amplitudes of the two frequencies, within the same period of the cosine function, should be known, as illustrates in Fig. 3.2. We have

$$A_1 = a_1 \cos(\pi f_1 \Delta\tau) \tag{3.6}$$

$$A_2 = a_2 \cos(\pi f_2 \Delta\tau) \tag{3.7}$$

where f_1 and f_2 are two different frequency components of the OFDM signal, A_1 and A_2 are the corresponding amplitudes. a_1 and a_2 are the corresponding ideal magnitudes of the OFDM signal transfer function without DGD, and are identical in general. By combining Eq.(3.6) and Eq.(3.7), we have,

$$\cos(\pi f_1 \Delta\tau) = q \cdot \cos(\pi f_2 \Delta\tau) \tag{3.8}$$

where q is the ratio of A_1 to A_2. If the values of f_1, f_2, A_1 and A_2 are known, the unknown parameter $\Delta\tau$ can be easily derived, via Eq.(3.8). A straightforward solution of estimating the amplitudes of the frequency components is to use an RF spectrum analyzer, which is expensive. Here, we propose a simple method based on data correlation technique to determine the amplitudes, A_1 and A_2, in order to derive the DGD value, $\Delta\tau$.

With the effectiveness of using signal correlation to estimate the average power of the pilot data sequences loaded onto a subcarrier in an OFDM signal, we propose to load two distinct pilot symbol sequences with the same average power as the other data-modulated subcarriers, into the OFDM signal, one at each end of the signal spectrum, as depicted in Fig. 3.2, so as to estimate the DGD value accumulated in the received DDO-OFDM signal. The data are modulated in quadrature amplitude modulated (QAM) format. The generated OFDM signal is then modulated by a conventional RF-tone aided optical OFDM [101] modulator to form the DDO-OFDM signal for transmission. At the receiver, in order to estimate the average power of the designated pilot data sequence loaded at the first optical subcarrier of the received DDO-OFDM signal, a time-domain pilot signal is generated by loading the same designated pilot data sequence to the respective subcarrier, with other subcarriers padded to zeroes, via IFFT. The pilot data sequence can be stored in the monitoring module in advance, so as to alleviate the computation requirement. Signal correlation operation is then performed between this pilot signal and the received DDO-OFDM signal so as to estimate the average received power of the first designated pilot data sequence. The same procedure is repeated by generating another pilot signal, which corresponds to the designated pilot data sequence loaded to the last optical subcarrier of the DDO-OFDM signal, and correlating it with the received DDO-OFDM signal in order to estimate the average received power of the second designated pilot data sequence. Fig. 3.3 shows the respective simulated correlation spectra after the signal correlation procedures have been performed for the two designated pilot sequences, showing prominent correlation peaks and their peak magnitudes are the same under zero DGD value. Hence, with the known frequencies of those two pilot subcarriers, together with the estimated values of their respective amplitudes, via the proposed correlation procedures, the DGD value accumulated on the DDO-OFDM signal can be derived, via Eq.(3.8).

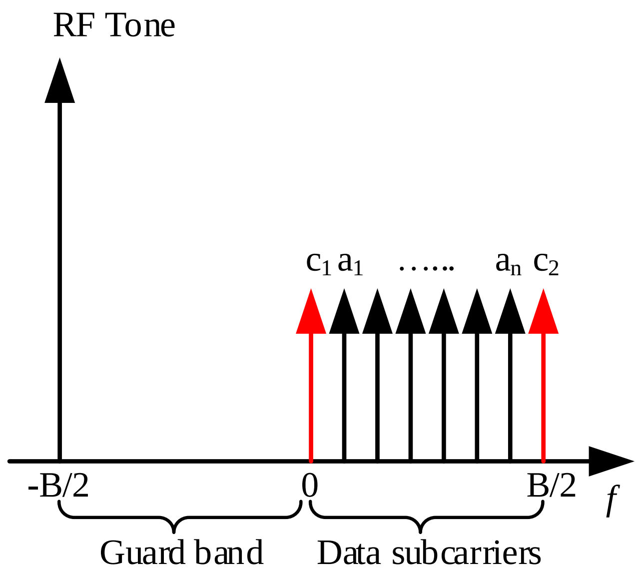

Fig. 3.2 Pilot and data arrangement in frequency domain. a1 to an (black) are normal data subcarriers, while c1 and c2 (red) are pilot subcarriers. B is the bandwidth of OFDM signal.

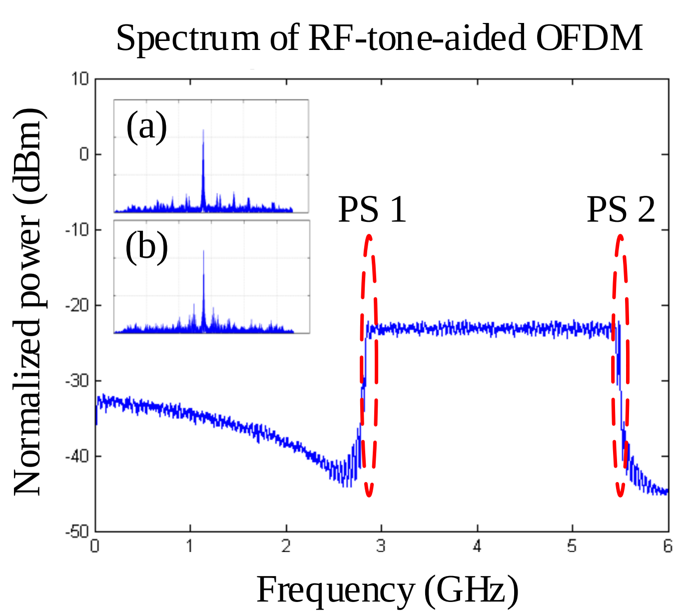

Fig. 3.3 Simulation result of frequency spectrum of direct detected RF-tone- assisted OFDM signal. The red circles mark the position of two inserted pilot subcarriers (PS). Insets are the correlation peaks for (a) pilot 1 and (b) pilot 2 when correlation is performed when DGD set to be 0 ps in simulation.

Here we use a searching algorithm to find the zero value of $g(\Delta\tau)$ in Eq.(3.9) when the frequency values and the power ratio are obtained.

$$g\left(\Delta\tau\right) = \cos(\pi f_1 \Delta\tau) - q \cdot \cos(\pi f_2 \Delta\tau) \tag{3.9}$$

A step is set first which defines the resolution of DGD calculation. $g(\Delta\tau)$ is calculated for a linear increment of $\Delta\tau$, until zero value occurs. The corresponding $\Delta\tau$ is the resolved DGD value. The computation complexity is determined by the resolution and monitoring range. For example, for a monitoring range of 45 ps and a resolution of 0.1 ps, the maximum number of searching attempts is 450, in the worst case. In the real-time implementation, if the frequencies of the pilot subcarriers are fixed, a simple lookup table method could be used to reduce the computation. The respective DGD values for each power ratio under certain resolution are pre-computed and stored in the look-up table. In the monitoring scheme, after the correlation procedure is performed and the power ratio is obtained, the respective DGD value could be directly retrieved, via the lookup table.

It is noted that deriving DGD value, via Eq.(3.9), has ambiguity, as it is a periodic function and has a series of solutions. A simple and effective solution is to limit the searching range of the possible DGD values. It is due to the fact that for signal with a certain bandwidth Δf, the maximum monitored DGD is determined by $1/(2\cdot\Delta f)$ (see Fig. 3.1).

The proposed pilot-correlated PMD monitoring scheme has a number of advantages. First, as the frequency spacing between two adjacent optical subcarriers in the DDO-OFDM signal is quite small, the use of the proposed pilot correlation procedure can estimate the average power of one particular pilot subcarrier without the need of any narrowband filter, with good accuracy. Moreover, the DGD value is derived, via the power ratio of the two pilot subcarriers, instead of their absolute power values, thus the channel response, which may influence the power estimation, can be compensated. Furthermore, the proposed scheme only requires one photodiode, followed by simple electronic correlation operations, which make it a low-cost and practical approach for PMD monitoring in a flexible optical network.

3.3 PMD monitoring in VSB DDO-OFDM system

The first proof-of-concept demonstration of the proposed code-correlation method of PMD monitoring scheme is in a vestigial side band (VSB) DDO-OFDM system. At the transmitter, the generated electrical OFDM signal was up-converted to an intermediate frequency first, and fed into an external intensity modulator. Then, the symmetry relationship between the two sidebands was broken by placing a fiber Bragg grating centered at one sideband right after the modulated optical signal, which generated a VSB DDO-OFDM signal. Fig. 3.4 illustrates how to use optical filter to generate VSB DDO-OFDM signal from an up-converted DSB DDO-OFDM signal.

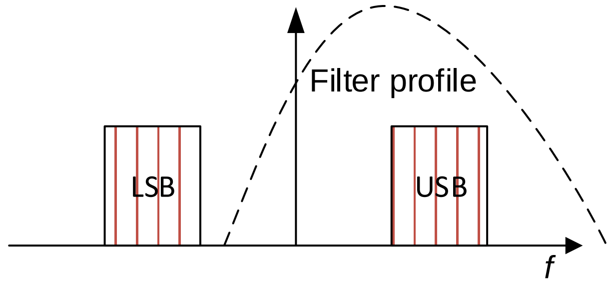

Fig. 3.4 Illustration of using FBG to generate VSB DDO-OFDM system

The goal of generating VSB DDO-OFDM signal is to remove the ambiguous power fading effect induced by the chromatic dispersion of fiber, such that the power fading is only induced by the PMD effect.

3.3.1 Experimental setup

Fig. 3.5 shows the experimental setup to verify our proposed PMD monitoring scheme. Traditional DDO-OFDM system using radio frequency (RF) up-converter was implemented. A total bit rate up to ~10 Gbps of OFDM signal was generated by an arbitrary waveform generator. The output electrical signal was then converted to a DDO-OFDM signal, via a 10GHz optical intensity modulator. The amplified optical signal was then filtered, via a fiber Bragg grating (FBG), with a 3-dB bandwidth of 17 GHz, so as to generate the VSB DDO-OFDM signal, which provided better robustness against fiber chromatic dispersion. PC2 was used to adjust polarization to equally split signal into two polarization mode of single mode fiber. A ProDelay^{TM} device from General Photonics was used as a DGD emulator. The optical attenuator before the second EDFA was to control the optical signal-to-noise ratio (OSNR). The optical signal was detected, via a P-I-N photodiode with 10-GHz bandwidth. The detected electrical signal was sampled and stored by a real-time digital sampling oscilloscope (DSO) and offline digital signal processing was employed to perform correlation between the designated codes with the received signal.

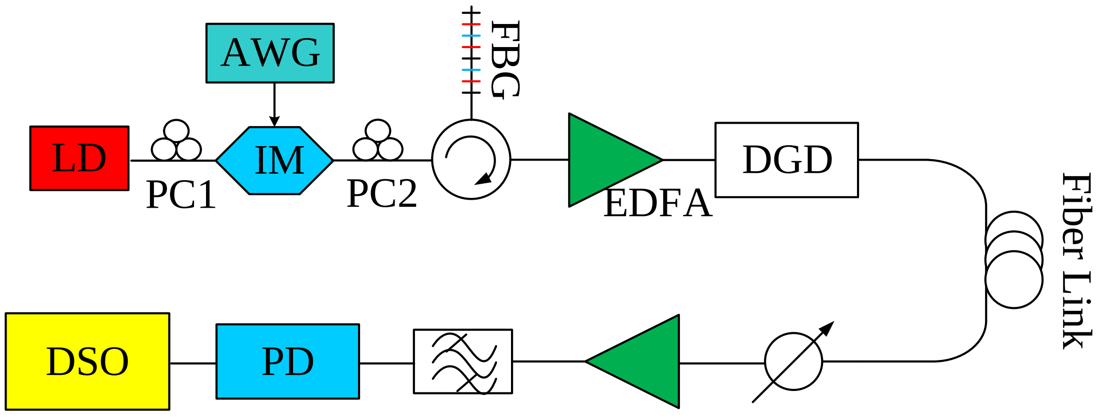

Fig. 3.5 Experimental setup. LD: laser diode; PC: polarization controller; IM: intensity modulator; DSO: digital sampling oscilloscope; VOA: variable optical attenuator.

3.3.2 Results

Fig. 3.6 shows the result of characterization measurements by setting the DGD emulator to values of 0.68 ps, 6.35 ps, 9.23 ps, 14.96 ps and 20.83 ps, under different OSNR values (0.1-nm bandwidth) of 15 dB, 20 dB, 25 dB and 30 dB. It could be noticed that our proposed scheme could successfully monitor the PMD value from 0 to 25 ps in DDO-OFDM transmission under different OSNR values. The average error was less than 2 ps.

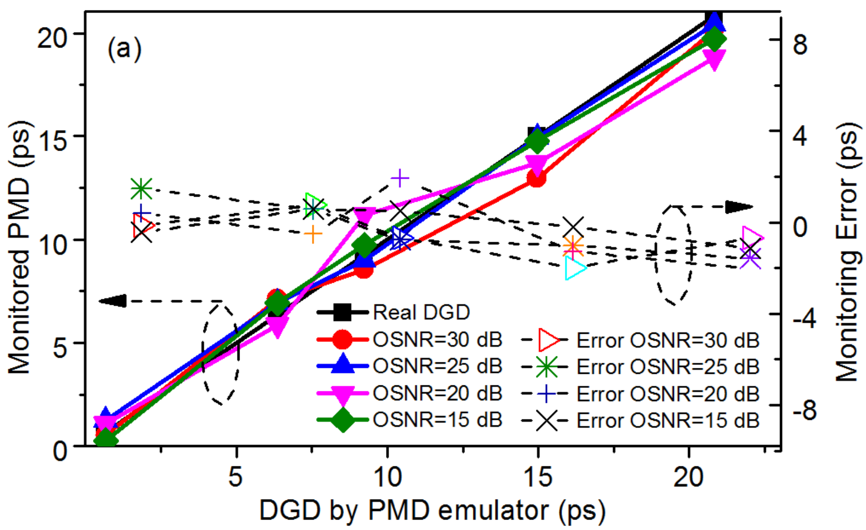

Fig. 3.6 Back-to-back measurement results and monitoring errors of DGD values from 0 to 25 ps, under OSNR values from 15 dB to 40 dB.

We have also performed measurements after transmission over 100-km standard single-mode fiber. The average monitoring error slightly increased to 2.2 ps, as shown in Fig. 3.7. This was mainly attributed to the inadequate filtering by the FBG, and much better result was expected if the FBG could have a narrower passband, close to 10-GHz bandwidth. Anyway, the result shows our proposed scheme is tolerant to chromatic dispersion.

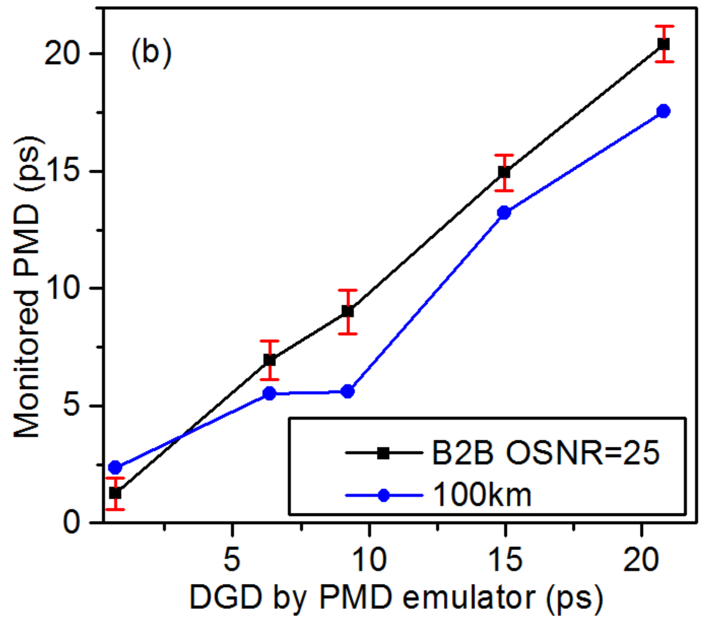

Fig. 3.7 Error bar of back-to-back monitoring at OSNR=25 dB and measurement results after 100-km transmission

3.4 PMD monitoring in SSB DDO-OFDM system

3.4.1 RF-tone aided DDO-OFDM system

The RF-tone aided DDO-OFDM system is first proposed by W. Peng in 2009 [101]. Apart from the conventional transmitter in direct-detection system which modulates the intensity of optical signal only, RF-tone aided DDO-OFDM uses in-phase/quadrature (IQ) modulator to generate optical OFDM signal. A virtual optical carrier generated by electrical method is sent to the receiver for beating with the signals. The benefit of this transmitter is that it can generate pure single sideband optical signal, thus it has better tolerance to chromatic dispersion than traditional DDO-OFDM system. Transmission experiment has demonstrated in 3,040 km [98] of single mode fiber link in RF-tone aided DDO-OFDM system.

3.4.2 Experiments and results

Experimental setup

Fig. 3.8 shows the experimental setup to verify our proposed PMD monitoring scheme. RF-tone-assisted gapped DDO-OFDM [101] was implemented. 256 subcarriers were used and 56 of them were modulated with the data in 16-QAM formats. A strong RF tone was inserted at the leftmost subcarrier as the virtual optical carrier. Two pilot sequences were modulated at the first and the last data subcarrier, respectively. The length of cyclic prefix length was set to be 5% of the OFDM symbol period. Altogether, 1024 symbols were generated. Electrical pre-emphasis equalizers were used to compensate the roll-off fading of the digital-to-analog converter. The OFDM signal was then synthesized, via an arbitrary waveform generator (Tektronix AWG7122C), with a sampling rate of 12 GSample/s. Consequently, a 10-Gb/s data OFDM signal was generated. Taking the guard band for DDO-OFDM into account, the generated OFDM signal had a total bandwidth of about 5.5 GHz. The real and the imaginary part of the output electrical OFDM signal were then converted to a single-sideband DDO-OFDM signal, via an optical IQ modulator, before being amplified by an erbium doped fiber amplifier (EDFA) to compensate the insertion loss of IQ modulator. A ProDelay™ device was used as a DGD emulator, whose tunable range was from 0 to 45 ps. After fiber transmission, the received optical signal was first attenuated by a variable optical attenuator (VOA), followed by an EDFA to adjust the OSNR. The optical signal was then detected, via a P-I-N photodiode with 10-GHz bandwidth. The detected electrical signal was sampled and stored by a real-time digital storage oscilloscope (DSO) (Tektronix DSA72004B). For each set DGD value, data were captured five times for averaging. Offline digital signal processing was employed to perform correlation between the designated pilot data sequences and the received signal. Then, the ratio of the estimated power, q, together with the frequency values of the two pilot sequences were used to calculate the DGD information using the proposed algorithm.

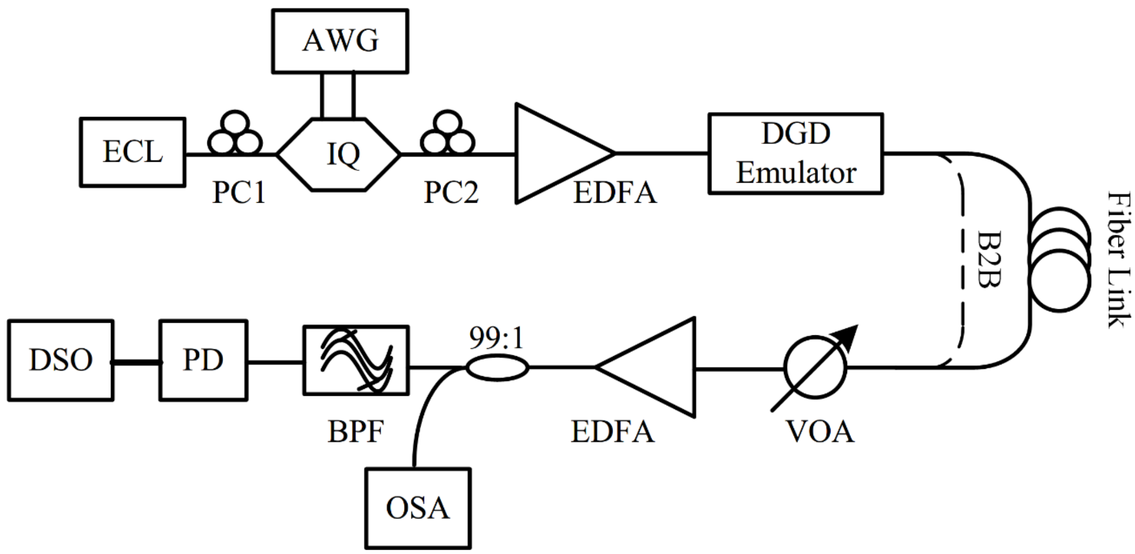

Fig. 3.8 Experimental setup. ECL: external cavity diode laser; AWG: arbitrary waveform generator; VOA: variable optical attenuator; OSA: optical spectrum analyzer; DSO: digital storage oscilloscope; PD: photodiode; PC: polarization controller; BPF: band-pass filter.

Impact of the insertion of two pilot subcarriers on the performance of the DDO-OFDM signal

First, we investigated the impact of the insertion of two pilot subcarriers on the performance of the DDO-OFDM signal. Fig. 3.9 shows the respective measured bit error rate (BER) performance over different OSNR values in the 100-km fiber transmission. Negligible impact due to the presence of the pilot subcarriers was observed from the results.

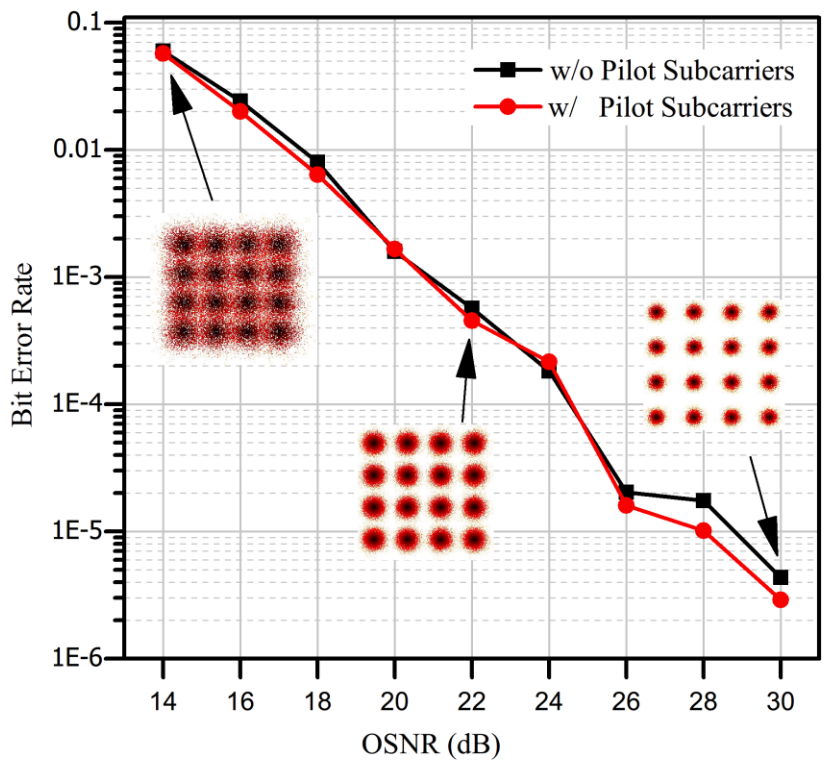

Fig. 3.9. BER performance for DDO-OFDM signal w/o and w/ pilot subcarriers insertion

Monitoring results

Then, we verified our proposed scheme in the presence of amplified spontaneous emission (ASE) noise. Fig. 3.10 shows the monitored DGD values versus the set DGD values, under four different OSNR (0.1-nm reference bandwidth) values of 15 dB, 20 dB, 25 dB and 30 dB. The received optical power at the photodiode was set to be -11 dBm in all measurements. As the additive ASE noise was uncorrelated with the pilot data sequence, their correlation results were much smaller than those between the pilot sequences and the signal, resulting in small fluctuations in the monitoring. The standard deviations of the monitoring errors at each OSNR value were all below 2 ps.

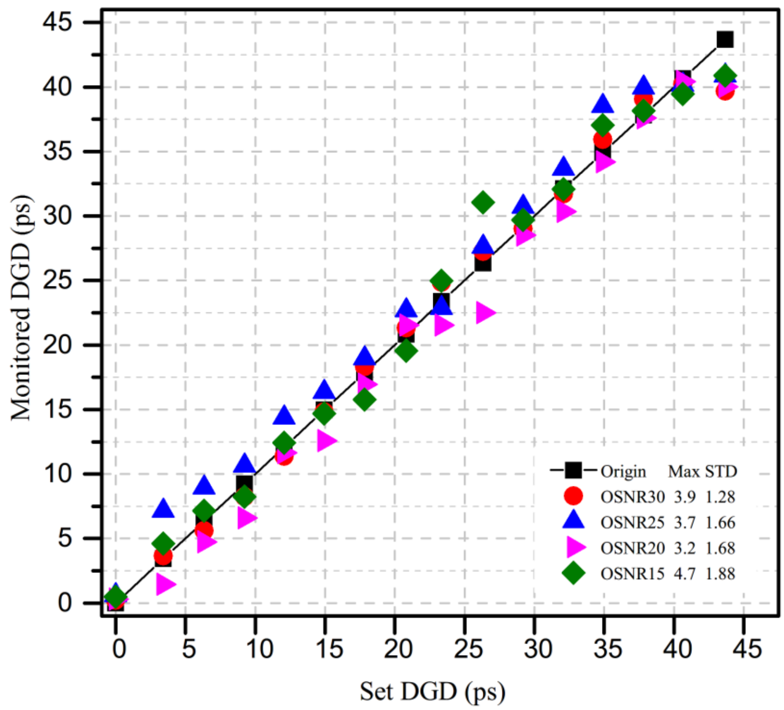

Fig. 3.10 Monitored DGD versus DGD value in the fiber link, under different OSNR values. “Max” stands for maximum monitoring error, while “STD” stands for standard deviation of monitoring error.

Fig. 3.11 shows the DGD monitoring results under different lengths of single mode fiber transmission and it was shown that CD induced power fading was negligible, which was attributed to the single-sideband of the DDO-OFDM signal. The standard deviations of monitoring errors were below 1.5 ps over the whole monitoring range.

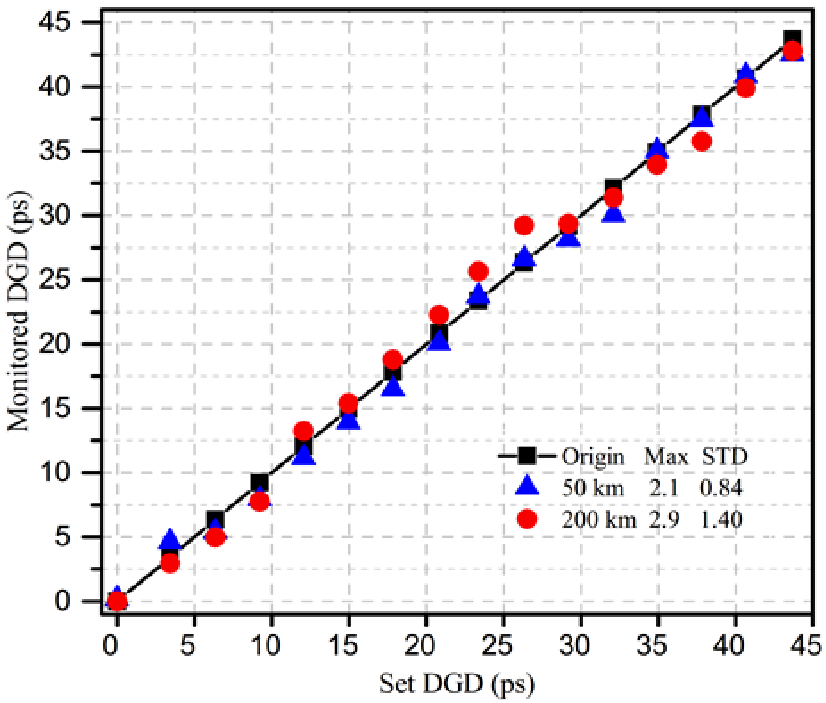

Fig. 3.11 Monitored DGD versus DGD value in the fiber link, with transmission length of 50 km and 100 km.

3.4.3 Discussions

In this section, the discussion is made in the following aspects: the feasibility of using low-bandwidth photodiode in the monitoring module, the monitoring scheme which is insensitive to the input angle of the state of polarization of the incoming optical signal, and the effect of polarization dependent loss on the first-order PMD monitoring. We show that, the cost of the code-correlated PMD monitoring scheme could be further reduced, and the monitoring accuracy could be increased at the same time.

Low bandwidth photodiode

Under normal optical signal detection, if the bandwidth of the photodiode is lower than the signal bandwidth, the out-of-band signal will suffer from large attenuation, which can be modeled as excessive filtering effect by a low pass filter. This filtering effect degrades frequency response to the converted electrical signal of photodiode. In order to employ a photodiode which has a much lower bandwidth than the signal bandwidth, it is required that the inserted pilot data sequence at higher frequency could still be detected by the signal correlation after severe signal attenuation due to much degraded frequency response of the photodiode. Besides, the correlation results have to be calibrated to obtain an accurate monitoring result.

In this investigation, the correlation result was measured using the same experimental setup, as shown in Fig. 3.5, except utilizing a photodiode with bandwidth of 1 GHz. The modulated OFDM signal has a bandwidth of about 5.5 GHz. Fig. 3.12 shows the correlation result of the pilot data sequences and the received data, when DGD was set to be 0 ps. It was shown that the correlation peaks were still salient, compared with the uncorrelated part. It was mainly due to the high peak to average value of the correlation result. However, the correlation peak value of the second pilot sequence was severely attenuated, with a factor of about 24, as shown in Fig. 3.12.

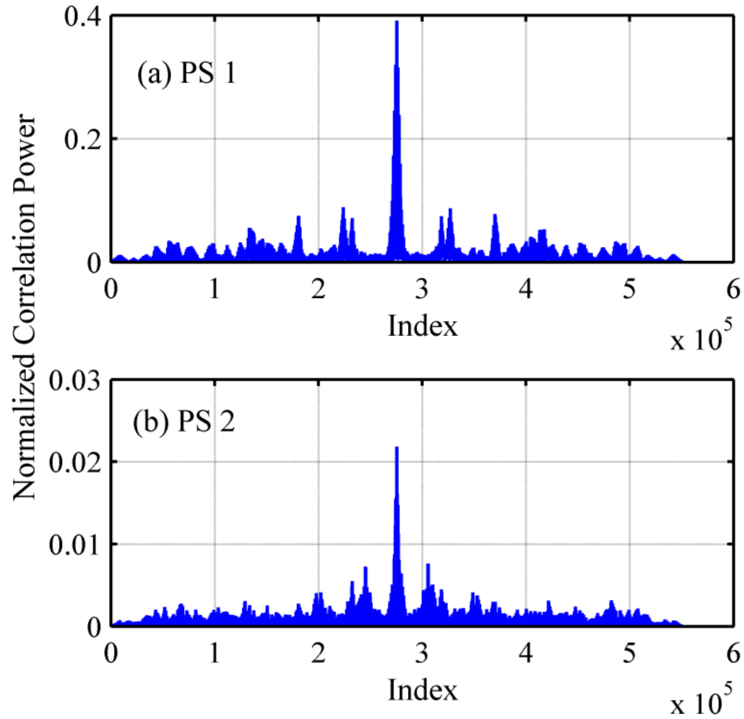

Fig. 3.12 Correlation peaks of (a) pilot subcarrier (PS) 1, (b) pilot subcarrier 2 with DGD = 0 ps. Photodiode of 1-GHz bandwidth is used.

With such excessive filtering at the high frequency region, the estimated values of a_1 and a_2, as in Eq.(3.6) and Eq.(3.7), will no longer be equal any more, even under zero DGD. Besides, the discrepancy is also dependent on the frequency response of the photodiode used, thus is device-specific. Therefore, the obtained correlation results have to be normalized by the reference power ratio of the two pilot subcarriers using the proposed pilot-correlation scheme, measured under zero DGD.

Numerical simulation was first performed so as to prove the feasibility of using low-bandwidth photodiode in the proposed PMD monitoring scheme. A 3-order Bessel filter with its bandwidth varied from 1 GHz to 10 GHz was employed to simulate the low-bandwidth photodiode's response, and it was used to filter the DDO-OFDM signal, having an effective bandwidth of 6 GHz (56 data subcarriers), before performing the signal correlation procedures to estimate the signal's DGD value. Fig. 3.13 shows the simulation results, in which the absolute values of the power ratios of the two pilot subcarriers decreased when the bandwidth of the photodiode increased until it exceeded that of the DDO-OFDM signal. Fig. 3.14 plots the respective adjusted power ratios after the calibration was applied. Negligible fluctuation in the respective adjusted power ratios was observed when the DGD value was lower than 35 ps, which revealed the feasibility and effectiveness of the calibration method.

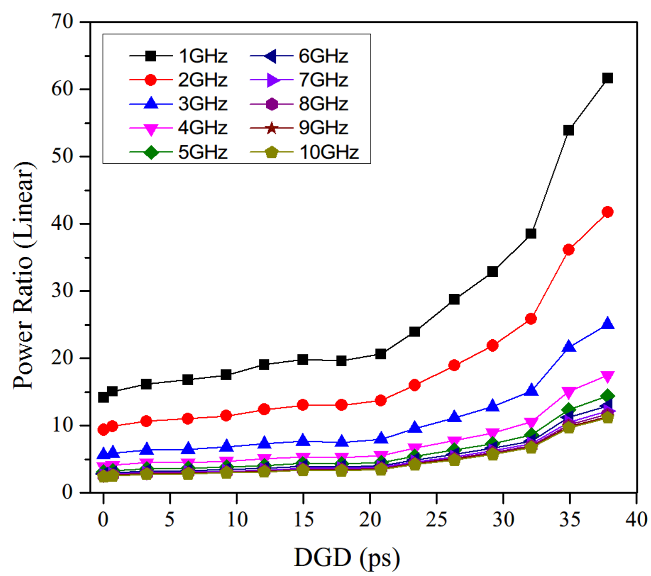

Fig. 3.13 Simulation results of power ratio of two pilot subcarriers w.r.t DGD values when the bandwidth of photodiode ranges from 1 GHz to 10 GHz (without calibration).

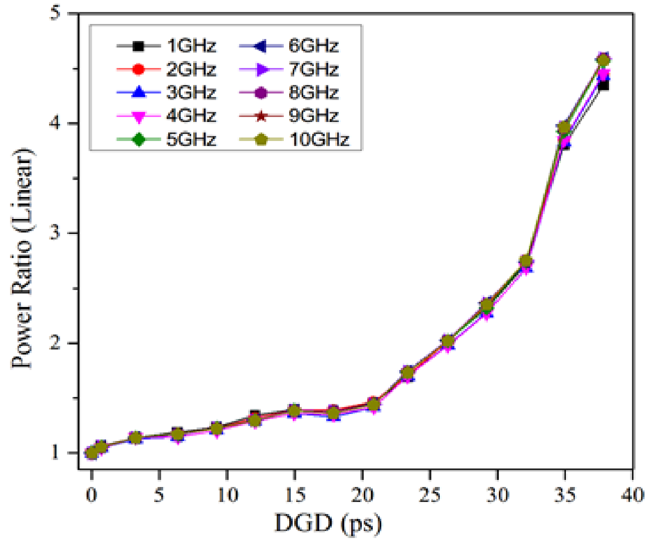

Fig. 3.14 Simulation results of power ratio of two pilot subcarriers w.r.t DGD values when the bandwidth of photodiode ranges from 1 GHz to 10 GHz. (With calibration).

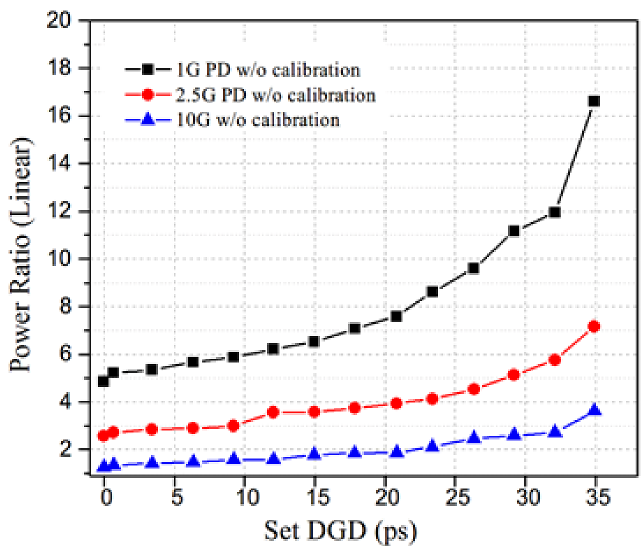

Fig. 3.15 Experimental results of power ratio of two pilot subcarriers w.r.t DGD values when the bandwidths of photodiode are 1 GHz, 2.5 GHz, and 10 GHz, respectively. (without calibration)

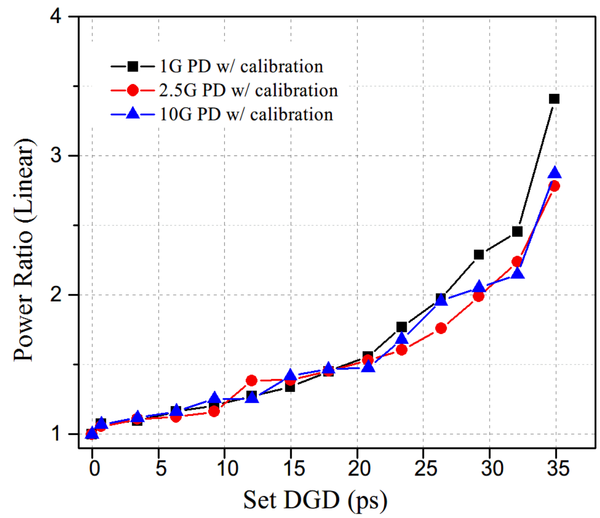

Fig. 3.16 Experimental results of power ratio of two pilot subcarriers w.r.t DGD values when the bandwidths of photodiode are 1 GHz, 2.5 GHz, and 10 GHz, respectively. (with calibration).

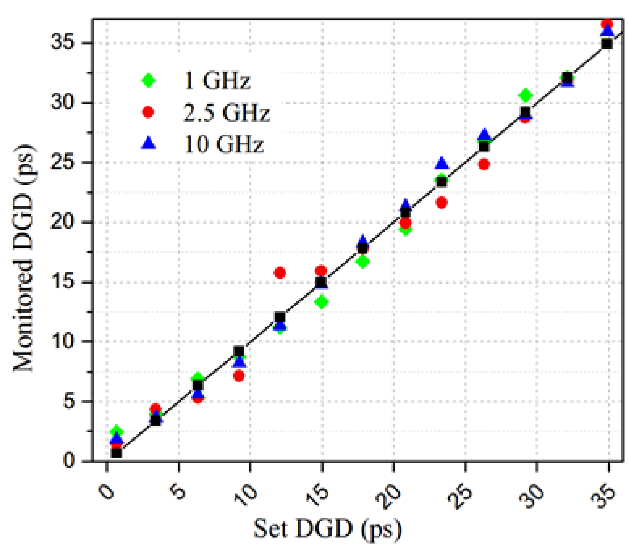

Fig. 3.17 Experimental results of monitored DGD values versus set DGD values when the bandwidths of photodiode are 1 GHz, 2.5 GHz, and 10 GHz, respectively. (With calibration)

Fig. 3.15 shows the experimental measurements of the power ratios of the two pilot subcarriers in the received DDO-OFDM signal with photodiode bandwidths of 1 GHz, 2.5 GHz, and 10 GHz, respectively, without calibration. Meanwhile, Fig. 3.16 shows the calibrated power ratios. The OSNR was preserved to be 25 dB in all cases. The received powers before the photodiodes were set to be optimum. The results show that the curves of the cases having calibration were very close to each other, proving the effectiveness of the proposed calibration method. Fig. 3.17 shows the DGD monitoring results based on the calibrated DGD values, using photodiodes of 1-GHz, 2.5-GHz and 10-GHz bandwidths, and they all showed good agreement between the set DGD values and the monitored DGD values. The standard deviations of monitoring errors ware below 2 ps, as well.

Input angle of state of polarization

All of the above investigations focus on the impact of the DGD induced by the fiber link on the optical signal. In such application, a polarization controller should be placed in front of a DGD element, to control the amplitude splitting ratio γ to be 0.5, such that the actual DGD effect on the optical signal equals the polarization mode dispersion of the DGD element. However, if the powers of the slow and the fast axes are not identical, that is, the input angle between the input signal and the PSP of the DGD element is not 45˚, the DGD effect on the optical signal is not identical to the exact value of the time difference between the two axes in the DGD element. In view of such phenomenon, a modified DGD monitoring scheme is proposed so that the monitoring results are independent of the value of the amplitude splitting ratio γ. It is more consistent with the practical case.

By squaring both sides of Eq.(2.3), we can obtain,

$$\left|H\left(\omega_k,\gamma,\Delta\tau\right)\right|^2 = 2\gamma\left(1-\gamma\right)\cos\left(\omega_k\Delta\tau\right)+\gamma^2+\left(1-\gamma\right)^2 \qquad (3.10)$$

which contains a constant component, $\gamma^2+(1-\gamma)^2$, thus makes the simple power ratio between the two pilot subcarriers inapplicable to derive the DGD information accurately. One feasible solution is to employ three pilot subcarriers with distinct pre-known symbols. Suppose there are three frequency components f_1, f_2, f_3, with their corresponding magnitudes, A_1, A_2, A_3, then we have:

$$A_1^2 = 2\gamma\left(1-\gamma\right)\cos\left(\omega_1\Delta\tau\right)+\gamma^2+\left(1-\gamma\right)^2 \tag{3.11}$$

$$A_2^2 = 2\gamma\left(1-\gamma\right)\cos\left(\omega_2\Delta\tau\right)+\gamma^2+\left(1-\gamma\right)^2 \tag{3.12}$$

$$A_3^2 = 2\gamma\left(1-\gamma\right)\cos\left(\omega_3\Delta\tau\right)+\gamma^2+\left(1-\gamma\right)^2 \tag{3.13}$$

By combining Eq.(3.11), Eq.(3.12) and Eq.(3.13) together, we have,

$$\frac{A_1^2 - A_2^2}{A_2^2 - A_3^2} = \frac{\cos\left(\omega_1\Delta\tau\right)-\cos\left(\omega_2\Delta\tau\right)}{\cos\left(\omega_2\Delta\tau\right)-\cos\left(\omega_3\Delta\tau\right)} \tag{3.14}$$

Consequently, no γ remains in Eq. (3.14) and thus the DGD value can be calculated insensitive to γ, with the magnitudes A_1, A_2, A_3, being retrieved by the proposed pilot-correlation procedures, as discussed in Section 3.2.3.

To verify the feasibility of this modified scheme using three pilot subcarriers, four different DGD values were tested experimentally, with three different arbitrary values of the input angle θ. Fig. 3.18 and Fig. 3.19 show the monitored DGD values versus set DGD values when two pilot-subcarriers and three pilot subcarriers were employed, respectively. The measured DGD values showed great variation in the former case (Fig. 3.18), while they showed little variance in the latter case (Fig. 3.19). We also conducted experiment verification by replacing the polarization controller with a polarization scrambler before DGD emulator, as in the experimental setup shown in Fig. 3.5. For each measurement, 10 random states of polarization ware altered by the polarization scrambler, and the DGD was measured with our proposed 3-pilot scheme. The measurement result, with its monitoring errors are shown in Fig. 3.20. Less than 3-ps monitoring error was observed. This confirmed the effectiveness of employing three pilot subcarriers in a DDO-OFDM signal to measure the DGD value of fiber under test insensitive to the input polarization.

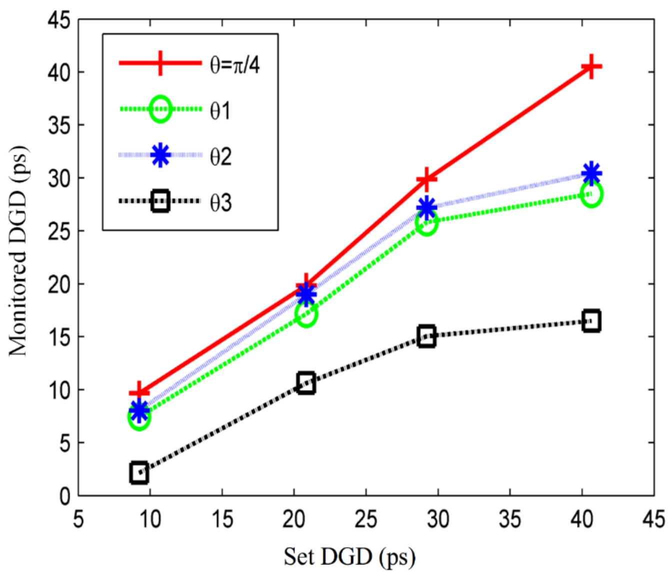

Fig. 3.18 Monitored DGD versus DGD of fiber link under different input angle for 2-pilot scheme.

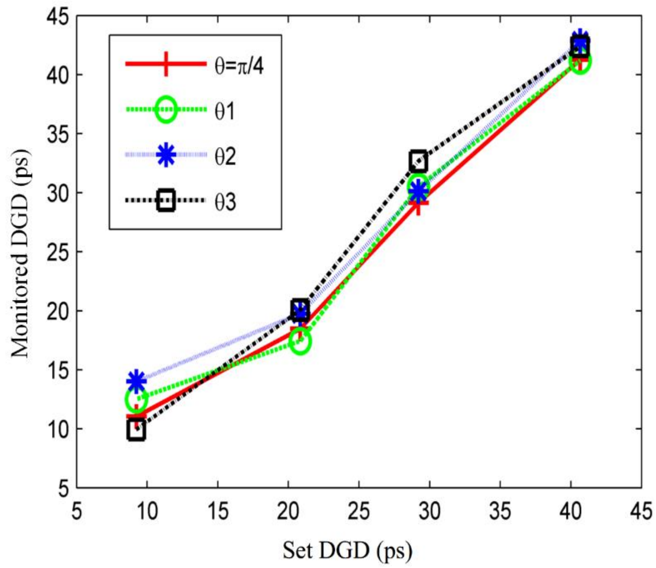

Fig. 3.19 Monitored DGD versus DGD of fiber link under different input angle for 3-pilot scheme.

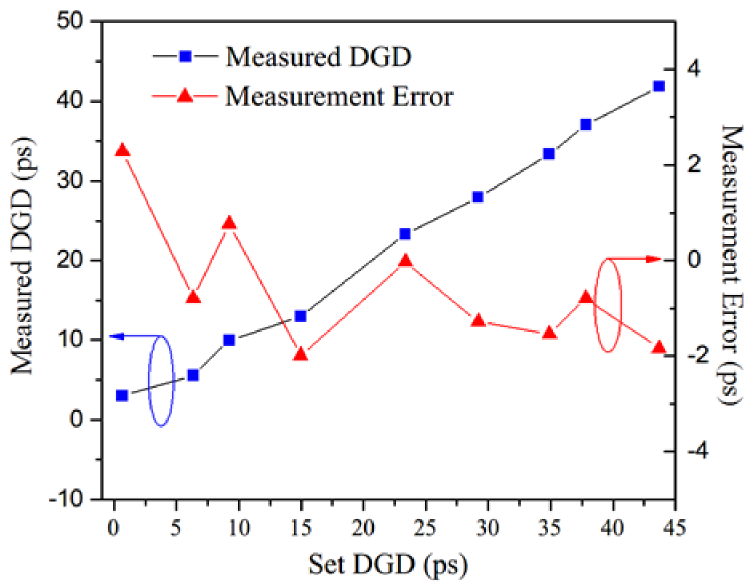

Fig. 3.20 Measured DGD and measurement error versus set DGD values.

Polarization dependent loss (PDL) effect

PDL originates from the polarization sensitive devices in the system. PDL itself can cause frequency independent optical power fluctuations and random OSNR variations, due to polarization state wandering during propagation [102]. Unlike the conventional RF power based PMD monitoring schemes, which are based on the absolute power of a particular RF tone, the fading introduced by pure PDL does not affect our proposed first-order PMD monitoring scheme, as it is cancelled in Eq.(3.8) by using the power ratio.

However, the mutual interaction of PMD and PDL may lead to additional system performance degradation since the two principal states of polarization are no longer orthogonal. To the best of our knowledge, there is no good solution reported to distinguish the PDL effect from the mutual interaction of PMD and PDL in most reported PMD monitoring schemes. Nevertheless, in [103], it has been pointed out that for the present fiber and devices, which have relatively small values of DGD and PDL parameters, the interaction between PDL and PMD would be significant only in ultra-long-haul transmission system, which is not the case for most of the DDO-OFDM applications. In general, a possible solution to alleviate the PDL effect is to add a polarization scrambler at the transmitter, which is widely adopted in various optical transmission system design to alleviate the PDL problem.

3.5 Implementation

The correlation can be performed by a digital correlator, then the power ratio of the outputs of two correlators is obtained. To get the DGD value, equation given by Eq.(3.9) needs to be solved. It is worth noting that there is a one-to-one correspondence between the power ratio and the calculated

DGD value. Therefore, we can use a lookup table (LUT) to replace complex equation-solving by the simple table query process. The block diagram of the implementation can been in Fig. 3.21. The three-pilot scheme is similar except one more correlator required and slightly more complicated operations of the correlation results.

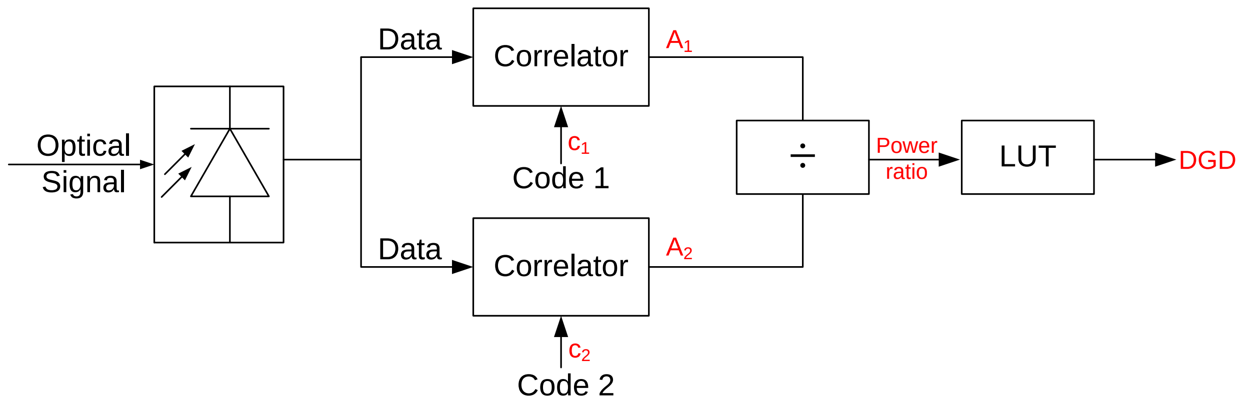

Fig. 3.21 Block diagram of the pilot-correlated PMD monitoring algorithm. LUT: lookup table.

3.6 Summary

In this chapter, we have experimentally proposed and extensively characterized a first-order PMD monitoring scheme for DDO-OFDM system. By inserting two or three pilot subcarriers to the DDO-OFDM signal, the accumulated DGD value of received DDO-OFDM signal can be accurately monitored. The DGD monitoring range for a 10-Gbit/s RF-tone-assisted DDO-OFDM system was measured to be about 45 ps. The standard deviation of the monitoring error was below 2 ps. By using the proposed pilot-correlation method, simple DGD monitoring is realized without using narrowband optical/electrical filter. No coherent receiver is required, as well. It has also been shown that a photodiode with bandwidth lower than the signal bandwidth can even be employed, at the expense of simple calibration. The low-complexity as well as high robustness against CD, OSNR and input angle to fiber, imply a strong potential of realizing practical PMD monitoring at the intermediate nodes in flexible optical networks.

Chapters 4 Phase noise estimation and compensation in CO-OFDM system

4.1 Introduction

4.1.1 Phase noise in CO-OFDM system

Coherent optical orthogonal frequency division multiplexing (CO-OFDM) is a promising technique enabling next-generation terabit-per-second, bandwidth-variable elastic optical network [104]. It exhibits a superb tolerance to the chromatic dispersion and polarization mode dispersion, but is very susceptible to laser phase noise and fiber nonlinearity. In general, laser phase noise induces a common phase error (CPE) to each OFDM symbol, which severely degrades the system performance if it is not properly estimated and compensated. Conventional compensation methods for CPE can be classified into two categories, namely analog approaches based on RF-pilot and digital approaches based on pilot subcarriers or blind estimation methods. Phase estimation using RF-pilot requires frequency guard bands and power overheads, thus reduces the spectral efficiency. Pilot subcarrier aided (PA) [59] is the most widely used CPE method, due to its simplicity and accuracy. Nevertheless, it occupies a relatively large number of subcarriers, which also reduces the spectral efficiency. Other non-data-aided CPE methods are mostly dependent on modulation formats and require extensive computation.

4.1.2 Bounding box versus CPE

At the receiver of a CO-OFDM system, after the coherent detection and conventional demodulation procedures, the *k*-th subcarrier in the *i*-th received OFDM symbol in time domain can be expressed as [59],

$$y_{ik} = x_{ik} \cdot h_k \cdot \exp(j\varphi_i) + n_{ik} \tag{4.1}$$

under the assumption that both frequency and timing are perfectly synchronized. In Eq.(4.1), the common phase error φ_i is independent of the subcarrier indexes and remains constant in the duration of one OFDM symbol. h_k is the channel impulse response and n_k is the additive Gaussian white noise in the channel. The constellation diagram in Fig. 4.1(a) illustrates the noise effect on the received sample after the compensation of the channel response h_k. The common phase error φ_i induces a common rotation to all the subcarriers in the OFDM symbol and thus the constellation diagram is skewed in shape.

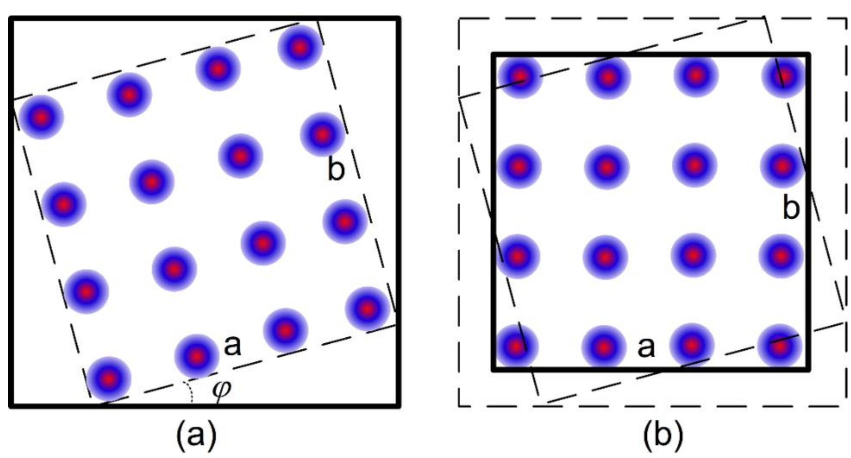

Fig. 4.1 Bounding box (solid line) of (a) a skewed rectangle and (b) a skew corrected rectangle

To use image processing techniques to estimate the common phase error φ_i, we first construct the 2-D points set X_i, using the real part and the imaginary part of y_{ik} in the i-th OFDM symbol.

$$\left(\Re(y_{ik}), \Im(y_{ik})\right) \in X_i, \tag{4.2}$$

where $\Re\{\ \}$ and $\Im\{\ \}$ denote the real and the imaginary parts, respectively. The bounding box of a two dimensional (2-D) graph is defined as the minimum rectangle in the horizontal and vertical direction (or axis-aligned) that covers all the pixels of the graph [105]. Fig. 4.1(a) shows the bounding box (solid line) of a skewed rectangle having a rotated angle of φ, while Fig. 4.1(b) shows the bounding box when the skew is corrected. It can be easily seen that the area of the bounding box is a function of the rotated angle φ,

$$s = ab + \frac{a^2 + b^2}{2}\left|\sin\left(2\varphi\right)\right| \tag{4.3}$$

where a and b are the respective length and width of the original rectangle without skew. Fig. 4.2 plots the normalized areas of the bounding boxes of different QAM orders in squared constellations, including 4-QAM (QPSK), 16-QAM, 64-QAM, oriented at different rotated angles. All of them (in dashed dot lines) exhibit the same periodic curve with a period of $\pi/2$, and reach their minimum values when the rotated angle equals $n\cdot\pi/2$, where n is an integer including 0. Fig. 4.2 also shows the cases for non-perfect rectangular constellation shape, say 32-QAM (in blue dashed line) and 128-QAM (in red solid line), and it is noticed that their minimum areas occur when the respective rotated angles are integer multiples of $\pi/2$, as well. The only difference is that their maximum areas do not occur at $\varphi = \pi/4$.

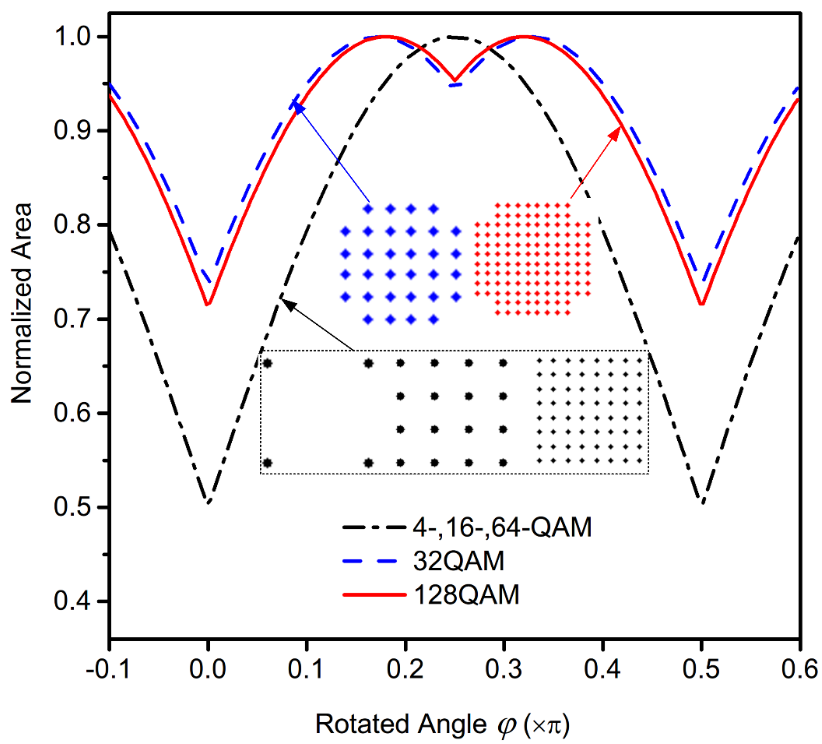

Fig. 4.2 Normalized area of bounding box w.r.t. the rotated angle in the constellation diagram of 4-, 16-, 32-, 64- and 128-QAM.

4.2 CPE compensation using MBB

In this section, we show our first attempt of using image processing techniques to estimate and correct the common phase error in CO-OFDM system. The algorithm is based on the area of the bounding box of the constellation diagram of the received data samples. We discussed the principles, the numerical simulation design and results to investigate the number of test phase and the tolerance to the laser linewidth, and the experimental results as well as a simplified modification of the proposed scheme.

4.2.1 Operating principles

The laser linewidth characterizes the variance of random phase noise to each symbol in the time domain. After the coherent detection and conventional demodulation procedures of in a CO-OFDM system, there remains the phase noise induced common rotation to all the subcarriers in one OFDM symbol [59]. Here, we consider a 16-QAM mapping, as an example for illustration. If we view the constellation diagram as a graph in the two-dimensional plane, determined by in-phase (I) and quadrature (Q) components, it can be regarded as a square with skew of an angle of θ, as shown in Fig. 4.3(a). In this way, the CPE estimation of the coherent OFDM is formulated as a skew detection problem, which has been a matured research area in image processing [106]. Considering the computation complexity and the feasibility in implementation, we employ a straightforward approach to estimate the CPE, via minimizing the area of the bounding box of the signal constellation. Given the constellation of a received OFDM symbol after channel estimation and equalization, the bounding box is defined as the minimum outer rectangle in horizontal orientation that can cover all the constellation points, as shown in Fig. 4.3 (b). First, the block of 16-QAM samples in the received OFDM symbol is rotated by N test phases, in the range of (0, $\pi/2$], in parallel. For each rotated block, the area of the bounding box s is calculated as,

$$\begin{aligned} s(\varphi_k) = l \cdot a = &\left\{\max\left[\Re\left(r \cdot e^{j\varphi_k}\right)\right] - \min\left[\Re\left(r \cdot e^{j\varphi_k}\right)\right]\right\} \\ &\cdot \left\{\max\left[\Im\left(r \cdot e^{j\varphi_k}\right)\right] - \min\left[\Im\left(r \cdot e^{j\varphi_k}\right)\right]\right\} \end{aligned} \tag{4.4}$$

where r is the received samples after channel equalization and φ_k is the k-th test phase. $\Re\{.\}$ and $\Im\{.\}$ represent the real and the imaginary parts of the complex number. l and a are the respective lengths of the two sides of the bounding box, as illustrated in Fig. 4.3 (b). The algorithm is based on calculating the area, *s*, covered by this bounding box under each test phase (see Fig. 4.3 (c)), which only requires very low computation complexity. The optimum estimated phase is determined by the test phase that minimizes the area *s*, i.e.

$$\hat{\theta} = \arg\min_{\varphi} \{ s(\varphi) \} \tag{4.5}$$

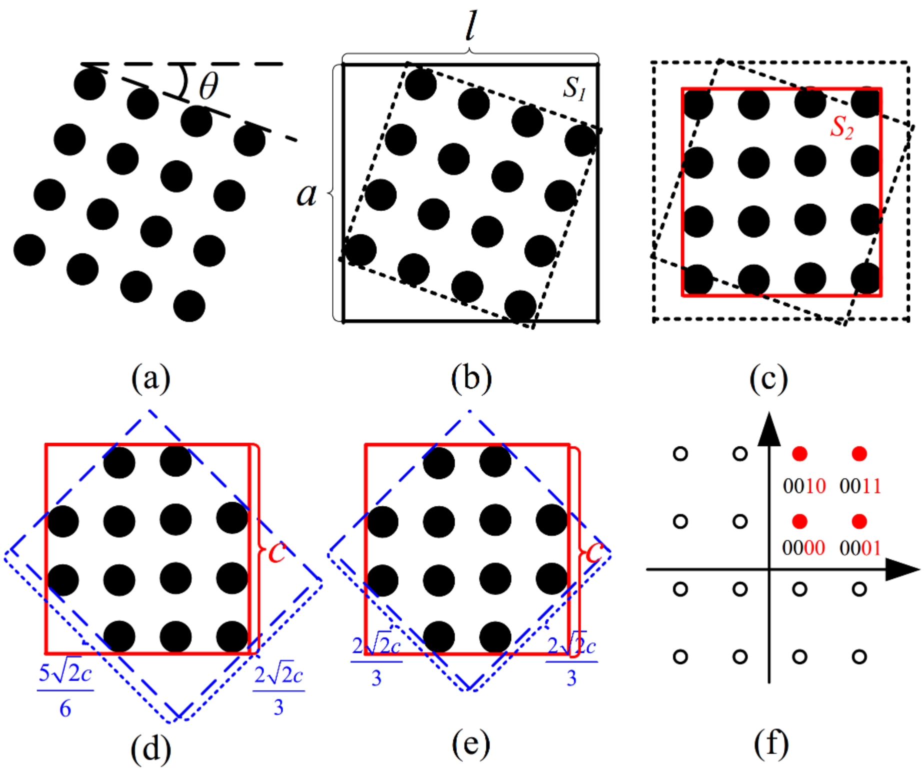

Fig. 4.3 Principles of using MBB to estimate the common phase error. (a) Constellation diagram of the received block. (b) The outer bounding box. (c) The minimum bounding box (red) of the original constellation diagram. (d) The case with three missing outer p

To eliminate the ambiguity induced by the square constellation diagram, a pilot subcarrier is inserted. However, the absolute angle of the pilot is not needed, as the quadrant information is enough to eliminate the ambiguity. Here we propose a new design of the pilot subcarrier. One pilot subcarrier is modulated with only complex symbols in the first quadrant of the constellation, so as to serve as the indicator of the quadrant. For example, if the modulation data format is 16-QAM, the pilot subcarrier is modulated with symbols of {1+*j*, 1+3*j*, 3+1*j*, 3+3*j*} in the first quadrant of the constellation, as shown in Fig. 4.3(f). This quadrant indicator occupies only the first two bits of the pilot subcarrier, and thus the other two bits on the pilot subcarrier can still be used to carry data. It is thus named as a quasi-pilot subcarrier. At the receiver, it only knows the pilot symbol should be in the first quadrant. After compensation, via the proposed minimum bounding box (MBB) algorithm, the quadrant of the pilot subcarrier is checked and used for ambiguity elimination. As will be shown later, one quasi-pilot is sufficient to dispel the uncertainty, thus the required overhead is quite small.

Besides, in case of the possible absence of the outermost symbols in the constellation, the proposed MBB algorithm can still correctly estimate the CPE. As depicted in Fig. 4.3 (d), even when three corner symbols are absent, the area of the correct bounding box in red (c^2) is still smaller than the blue one ($10c^2/9$). However, for the case of missing all four corner symbols (see Fig. 4.3 (e)), the area of the red bounding box is larger than that of the blue one ($8c^2/9$), thus estimation error may occur. This problem can be alleviated by increasing the number of subcarriers in one OFDM symbol. For instance, if there are 128 data-carrying subcarriers in one OFDM symbol, the possibility of missing all four corner symbols is $(12/16)^{128}=10^{-16}$, leading to a bit error rate of 1.28×10^{-14}.

4.2.2 Numerical simulations

To extend the work reported in [107], we have further carried out numerical simulations to investigate the effect of the number of test phases (B), in the proposed technique, compared with the number of pilot subcarriers with identical performance, in a CO-OFDM system. In our simulation, 128000 16-QAM symbols were loaded onto 128 subcarriers. 20 pilot subcarriers were equally distributed among these data subcarriers for CPE estimation. One more quasi-pilot subcarrier was inserted using the mapping method, as described above for CPE estimation using MBB method. All the pilot subcarriers and the quasi-pilot used were normalized to have equal average powers as the data subcarriers. The IFFT size was 256 with the other subcarriers padded to be zeros. The generated data was digitally sampled at a rate of 12 GSample/s. The length of the cyclic prefix was 12.5% of total subcarriers, thus the net data rate is ~21.4 Gb/s. The linewidths of the laser used for signal generation and that one used as local oscillator were both 100 kHz, emulated under the model of Wiener process.

Fig. 4.4(a) shows the bit error rates (BER) versus optical signal-to-noise ratio (OSNR) for coherent optical QPSK-OFDM and 16QAM-OFDM signal. The results showed a good match with the PA method. Linewidth tolerances of our proposed method MBB, together with the commonly used PA method were also simulated, at the required OSNR when the bit error rate was 10^{-3} in both cases. The result is shown in Fig. 4.4(b). The discrepancy in the linewidth tolerance for these CPE compensation methods is small and negligible.

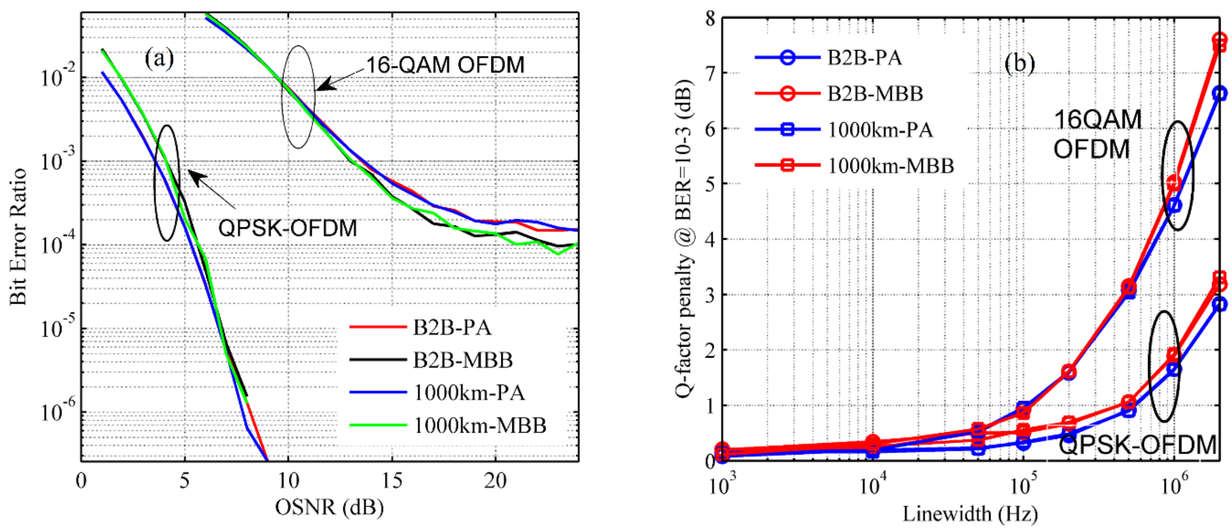

Fig. 4.4 Simulation results of (a) BER versus OSNR (b) Q-factor penalty w.r.t laser linewidth.

Fig. 4.5 shows the bit error rate (BER) versus the number of test phases (*B*) used in the CPE processing. The optical signal-to-noise ratio (OSNR) was set to be 13 dB, which corresponded to a BER of 10^{-3} when no laser phase noise is loaded in our simulation system. As shown, 8 and 15 test phases had comparable performance as the cases of 8 and 16 pilot subcarriers (PS), respectively. Note that the increase in the test phase only increased the computation complexity of offline processing and had no influence on the spectral efficiency. The total overhead in each OFDM symbol was only 2 bits (one half symbol for a 16-QAM signal). Compared with the cases of 8 or 16 pilot symbols when PA method was used, the overhead of the proposed MBB algorithm was reduced by 93.75% and 96.88%, respectively. As shown in Fig. 4.4(a), our proposed MBB method has comparable performance than the PA method, with very small penalty.

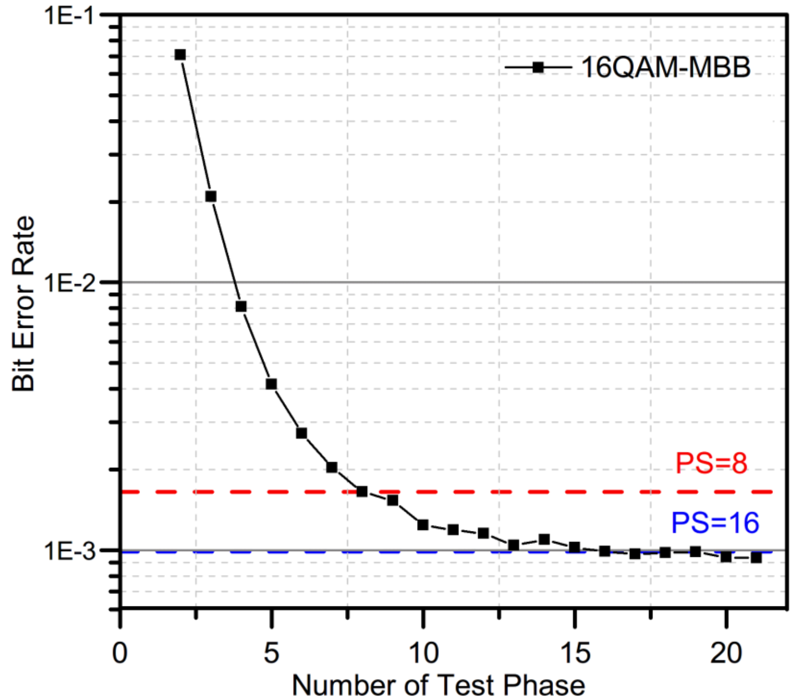

Fig. 4.5 Simulation results: BER versus the number of test phases B under the proposed MBB algorithm. OSNR=13dB. PS is the number of pilot subcarriers under the PA method.

4.2.3 Experiments

Fig. 4.6 shows the experimental setup to verify our proposed CPE estimation scheme using MBB algorithm. A conventional CO-OFDM system with all the parameters identical to the simulation was implemented. Two Emcore tunable lasers were used as the signal laser and the local oscillator, with equal linewidth of ~100 kHz, resulting in an equivalent linewidth of 200 kHz. The radio-frequency (RF) OFDM signal was generated by an arbitrary waveform generator (Tektronix 7122C) with a sampling rate of 12 GSample/s. The continuous wave from the signal laser was then modulated with the RF OFDM signal, as described above, via an optical IQ modulator. The generated optical OFDM signal was first amplified by an Erbium doped fiber amplifier (EDFA), followed by a variable optical attenuator (VOA), so as to emulate different OSNR values. The optical signal was then fed into a recirculating loop, which comprised a segment of 70-km single mode fiber, followed by an EDFA to compensate the loss in the loop. The received optical signal was detected by a conventional coherent optical receiver. The electrical signal was then sampled by a real-time oscilloscope (Tektronix 72004B) at a sampling rate of 50 GSample/s for offline digital signal processing. Conventional OFDM synchronization and frequency offset compensation method were employed.

First, we investigated the BER of the demodulated OFDM signal under the proposed MBB algorithm and the conventional PA method, at different OSNR values, in back-to-back (B2B) transmission. 16 pilot subcarriers were employed in the PA method. The number of test phases used in the MBB method was 15. These two parameters were used hereafter. As shown in Fig. 4.7, the MBB scheme has a comparable performance as the PA method.

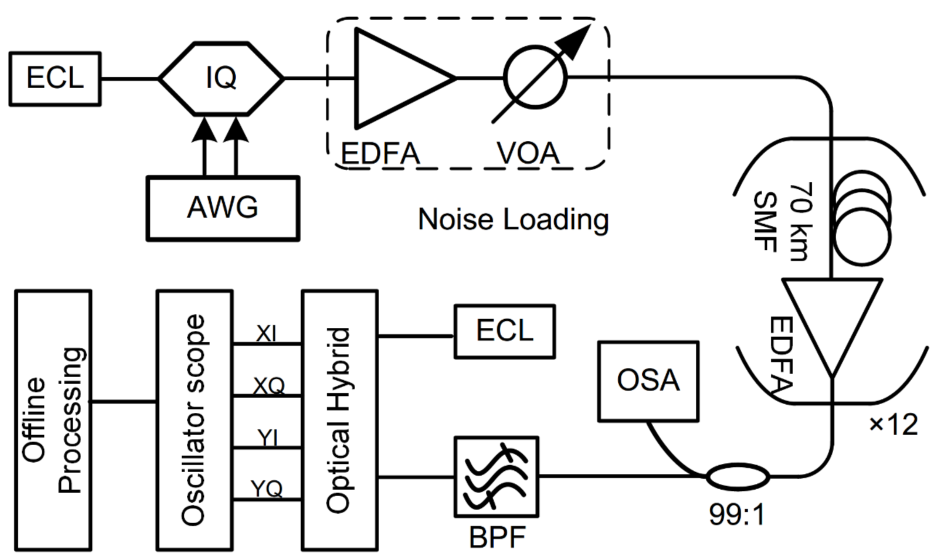

Fig. 4.6 Experimental setup. ECL: external cavity laser; AWG: arbitrary waveform generator; VOA: variable optical attenuator; OSA: optical spectrum analyzer; BPF: band pass filter.

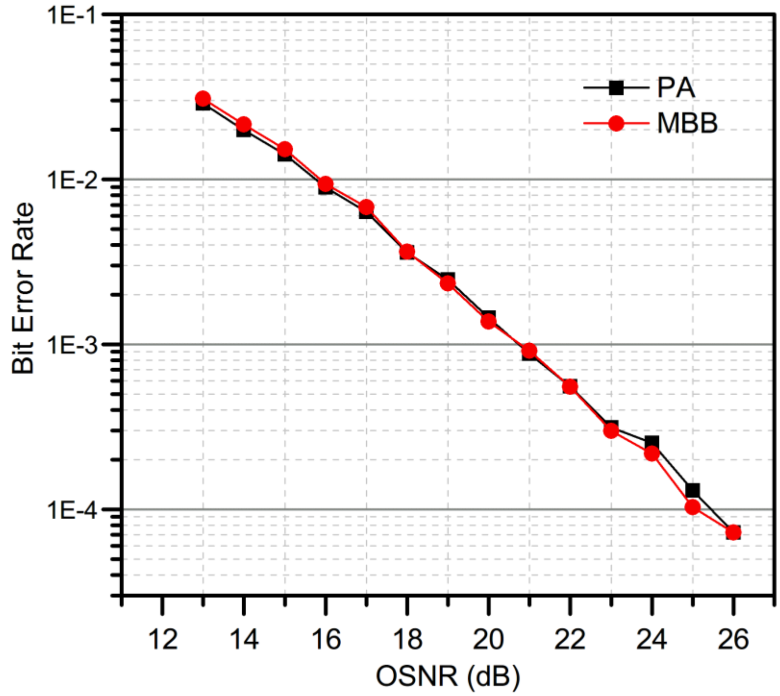

Fig. 4.7 Bit error rate performance of back-to-back transmission using PA and MBB method

To further investigate the tolerance of the proposed MBB method against fiber nonlinearity, a long haul transmission experiment was conducted. As seen in Fig. 4.6, a recirculation loop with 12 spans was used to emulate 840-km single mode fiber transmission. The input power of the CO-OFDM signal was altered from -4 dBm to +7 dBm, in a step of 3 dB. The Q factors were calculated, using both PA and MBB methods, from 50000 OFDM packets at each input power value. Fig. 4.8 shows that MBB method had 0.05 dB performance increase than PA method at the optimum input power of -1 dBm. Their performance is comparable as well.

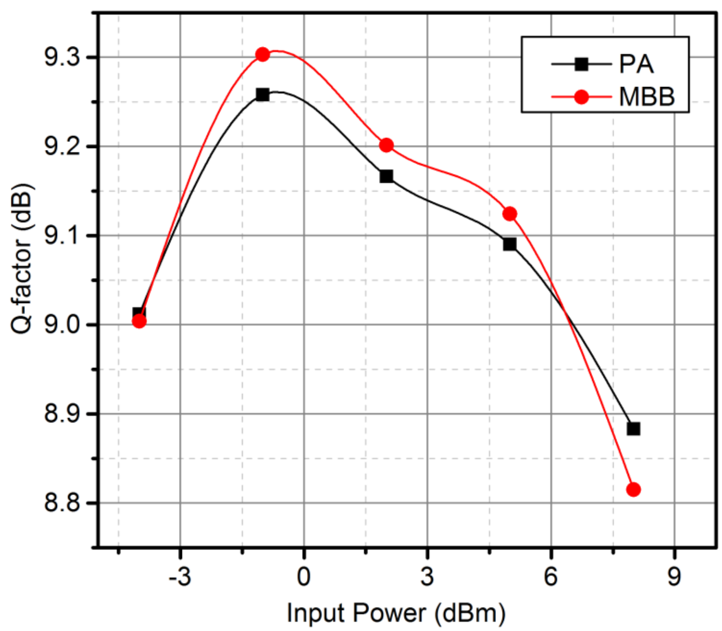

Fig. 4.8 Q factors versus input power with PA method and MBB method in 840- km single mode fiber transmission.

4.2.4 Discussions

It is obvious that the symbols located at the inner part of the signal constellation have no influence on the characterization of the outer bounding box as the bounding box is only determined by the outermost points. Therefore, the computation complexity can be further reduced, if some of the samples with the symbols lying at the inner part are removed in the MBB method. Here we consider omitting the samples whose distances to the origin in constellation diagram are smaller than a radius r. To estimate the optimized radius r of the clipping area, the received data is first normalized and the samples with their symbols lying inside the circular clipping are omitted before using the MBB method to estimate the CPE. Fig. 4.9 shows the Q-factor penalty and the processing-ratio at an OSNR of 25 dB versus the clipping area radius r, varying from 0 to 4.2, where the processing-ratio is defined as the ratio of the number of samples involved in MBB processing and the number of total OFDM symbols. It was shown that as long as the radius was less than ~3.8, the BER performance was not affected. When the radius for clipping was 3.8, only 25% of the samples were used, and the respective induced Q-factor penalty was less than 0.1 dB. In practical implementation, a rectangular clipping area is more preferred, as it would be more hardware-efficient to use comparators to process the clipping.

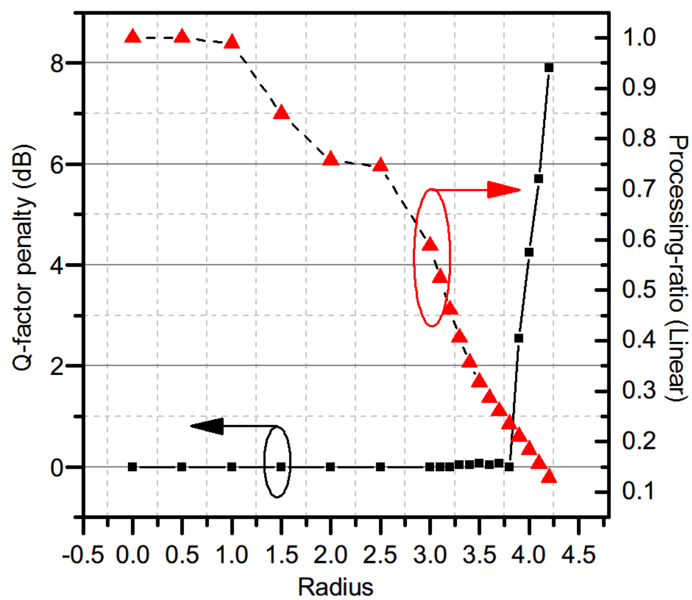

Fig. 4.9 Q-factor penalty when clipping with different radius r. OSNR=25 dB.

4.2.5 Conclusion

In this section, we have proposed a novel CPE estimation method based on MBB, which is a common image processing technique. It has been proved, via numerical simulations and experiments, that it gives substantial improvement in spectral efficiency and comparable performance over the conventional PA method.

4.3 CPE compensation using BBB

In Section 4.2, we have successfully demonstrated the feasibility of using the bounding box to solve the CPE problem in CO-OFDM system. However, the computation complexity, as well as the accuracy of the algorithm are still under investigation. In this section, we propose a novel CPE algorithm, which also depends on the bounding box of the constellation diagrams but in another form, to improve the accuracy and in the meantime, reduce the computation complexity. We name this creative approach as BBB algorithm. A detailed complexity comparison has been made in this section, as well.

4.3.1 Operating principles

4.3.1.1 Best-fit bounding box

Unlike the conventional definition of bounding box proposed in which is limited to the upright direction [108], the best-fit bounding box is defined as the minimum rectangle that covers all the pixels in the graph in any possible direction. It can be obtained through the convex hull of the graph. In computational geometry, the 2-D convex hull of a finite point set X_i is the smallest 2-D convex polygon that contains X_i. For instance, the points connected by red solid line in Fig. 4.10(b) are the corresponding convex hull of the set of received points. It has been theoretically proven that the smallest enclosing rectangle of a polygon has a side collinear with one of the edges of its convex hull [75].

Then, the rotating calipers algorithm [74] is used to find the best-fit bounding box. Each edge of the convex hull is rotated and aligned along a major axis, say x-axis. Next, the axis-aligned bounding box of the rotated convex hull is obtained, as illustrated in Fig. 4.10(c), and its area is then calculated. After applying the same procedures to all edges of the convex hull, the case with the minimum axis-aligned bounding box area is selected and the respective rotated angle from the initial state is the estimated CPE angle, as depicted in Fig. 4.10(d), for example.

Compared with the previously proposed MBB method, the proposed BBB algorithm has the reduced computation complexity and increased accuracy. In the MBB algorithm, all the constellation points are rotated under each considered test phase and the respective bounding box area is calculated. It requires extensive hardware resources in the real-time implementation, especially if the number of test phases is large for higher resolution. However, in this proposed BBB algorithm, only the points on the convex hull are involved in the computation, thus the requirements for the real adders and multiplexers can be largely reduced. Meanwhile, the total number of rotation is determined by the number of edges of the convex hull, which is also a small number, according to the limited number of total points in the convex hull, especially for high order QAM mapping. Fig. 4.11(a) plots the sizes of convex hull of 512 OFDM symbols, and each symbol has 128 data subcarriers loaded with 16-QAM signals. The convex hull size ranges from 7 to 20, and has a mean value of 12.87 with a standard deviation of 1.90. Fig. 4.11(b) shows the average size of convex hull of 50000 OFDM symbols with different signal-to-noise ratio (SNR) value. It shows that the size of convex hull is not sensitive to the noise level. The number of complex multiplexers required in the rotating caliper algorithm equals the square of the size of the convex hull, as each edge needs to be traversed and the all points in the convex hull are involved. In addition, the BBB method can always find the best-fit bounding box, thus alleviates the resolution limitation, achieving better accuracy.

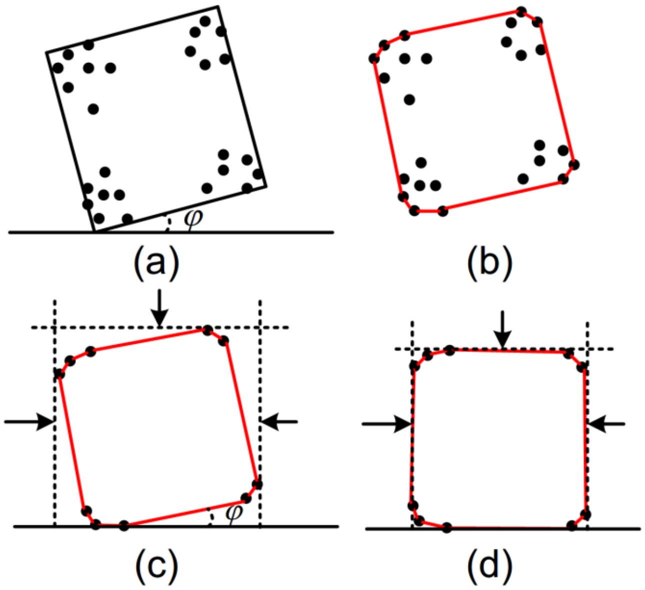

Fig. 4.10 Principles of using best-fit bounding box to estimate the common phase error. (a) constellation diagram of the received block and its best-fit bounding box; (b) the convex hull of the constellation points (connected through red solid line)); (c) rotate the convex hull by alwith the each slope angle and use caliper to calculate area for one certain slope angle; (d) the case when the minimum axis-aligned bounding box area is found.

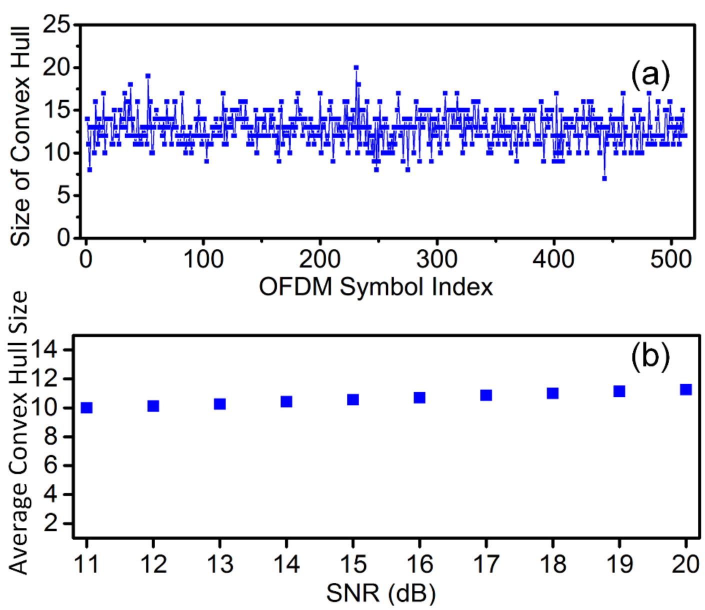

Fig. 4.11 (a) Size of convex hull in each OFDM symbol with 128 data subcarriers. (b) Average size of convex hull of 50000 OFDM symbols with different SNR.

In general, the common PA method has the least computation complexity, as it only calculates the phase average among all the pilot subcarriers. All the blind approaches increase the complexity, but gain a conspicuous improvement in the spectral efficiency. We have shown that the MBB method has much reduced complexity than the conventional blind phase searching algorithm in [108]. The computation complexity of the convex hull in the proposed BBB method is as low as $O(N*\log(H))$, theoretically [77], where N is the total number of points and H is the expected size of convex hull. If the number of points in one OFDM symbol is large enough, an order of magnitude reduction in computation time can be achieved [105]. Moreover, a simple heuristic is often used as pre-processing before calculating the convex hull in the practical implementation, which quickly excludes many points that would be less likely to be candidates of the convex hull [109]. In this way, an expectation of linear processing time has been achieved in [110]. The detailed complexity analysis is depicted in Section 4.3.2.

4.3.1.2 Modified bounding box algorithm

When using bounding box based method to correct the skew angle, one challenging factor that may influence the accuracy is the possible presence of outliers, which are defined as the sampled points that lie distant from the outermost constellation symbols. It may be attributed to the random properties of the amplified spontaneous emission (ASE) noise or the phase noise induced higher-order effect, i.e., inter-channel interference. For instance, Fig. 4.12(a) shows a few outliers (marked inside red circles) on the 16-QAM constellation diagram and they will be considered when the convex hull is generated. After applying the BBB method, the constellation diagram can be still de-skewed, as shown in Fig. 4.12(b), thus the effects of these outliers are insignificant. However, for the case depicted in Fig. 4.12(d), the presence of the outliers (marked inside red triangles) severely affects the CPE estimation using the BBB method and large estimation error is resulted, as shown in Fig. 4.12(e). Therefore, the outliers have to be removed to increase the estimation accuracy.

In [111], Rossen et al. discussed several algorithms for optimal outlier removal based on different criteria, including minimizing diameter, enclosing rectangle or convex hull. However, the complexities of these algorithms are relative high for our application. Here, we propose a simplified method similar as the minimizing enclosing rectangle approach in [111], named as modified BBB (mBBB) method. After applying the BBB method on the input constellation diagram, the points located in the four region are defined by

$$\begin{gathered}\{P_1(x,y)\,|\,\alpha x_{\max} \le x \le x_{\max}\},\{P_2(x,y)\,|\,x_{\min} \le x \le \alpha x_{\min}\},\\ \{P_3(x,y)\,|\,\alpha y_{\max} \le y \le y_{\max}\},\{P_4(x,y)\,|\,y_{\min} \le y \le \alpha y_{\min}\}\end{gathered} \tag{4.6}$$

where x and y are the real and imagine part of the constellation points respectively. α is a coefficient which is optimized as 0.98 in our simulation. The numbers of points in these four region could be used as estimation of the density. If the points in any region are less than a threshold number (2 was used in our work), this region is judged as containing outliers and all the points in this region are removed then another BBB procedure is performed. Otherwise, there is no outliers thus no need to perform additional BBB process. Fig. 4.12(b) & (e) illustrate the denoising process of mBBB method.

Meanwhile, the ASE and inter-channel interference both have a Gaussian effect on the distribution of constellation points. As long as α is not too large, this process is reliable to improve the performance. Fig. 4.12(c) and (f) shows the constellation diagram after applying the edge de-noisng algorithm. The outliers are successfully removed and the CPE in both cases are compensated perfectly. One step of the edge denoising proccedure in mBBB is enough due to the relatively large noise tolerance of the BBB algorithm.

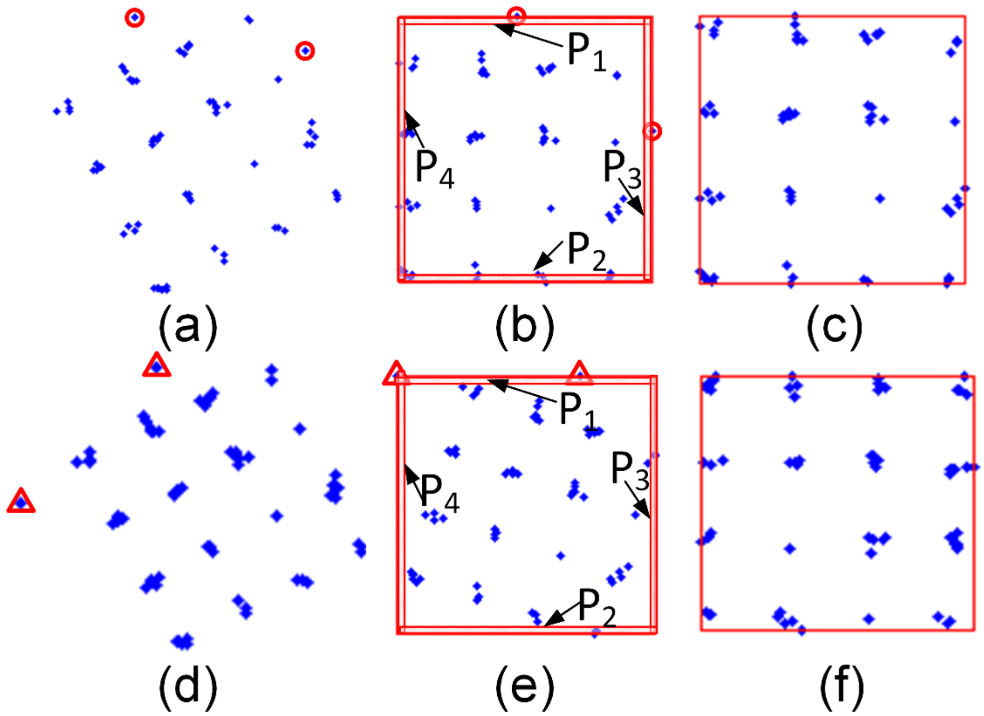

Fig. 4.12 Illustration of outliers in the constellation diagram. (a) & (d) outliers in a 16-QAM constellations (circle and triangle); (b) & (e) the de-skewed constellation diagrams and their bounding boxes via BBB method; (c) & (f) the constellation diagrams after applying edge de-noising algorithm.

In the end of this section, it is worth noting that the ambiguity problem in [108] is also a critical issue in the BBB algorithm. Therefore, a two-bit quasi-pilot is still necessary here. The quasi-pilot design is the same as in [108].

4.3.2 Performance analysis

In this section, we investigate the performance of the proposed best-fit bounding box method. The noise tolerance, including the robustness to ASE noise and the variance of laser phase noise, which is characterized by laser linewidth, is investigated in detail. Meanwhile, an exhaustive analysis on the computation complexity has been made to take the practical implementation into consideration.

Noise tolerance

To have an accurate CPE estimation using image processing technique, sufficient samples are required to obtain a reliable bounding box. Similar to the PA method, the number of data samples in one OFDM symbol contributes to the estimation accuracy and noise tolerance. Here, we performed numerical simulations to investigate the noise tolerance with different number of samples used in the CPE estimation. One million OFDM symbols with a FFT size of 256 was generated. 120 of the subcarriers were modulated with 16-QAM data. The phase noise is inserted by multiplying the phase of time-domain symbols with a random distribution under Wiener-Levy process [56]. At the receiver, N samples with equal spacing were used to form the 2-D constellation graph and estimate the CPE.

Fig. 4.13 and Fig. 4.14 show the simulation results of the root mean square error (RMSE) of CPE estimation for 16QAM-OFDM signal using the MBB and the BBB methods, respectively, under different SNR values. The mean value of the phase noise in the duration of one OFDM symbol was used as reference. The value of N was changed from 20 to 120 in both cases. It showed that if more samples in the OFDM symbol were used to estimate the CPE using the BBB method or the MBB method, the RMSE could be reduced and the noise tolerance was increased. In most cases, less than 0.1 rad of RMSE could be achieved when the SNR was higher than 10 dB. It was also shown that the BBB method achieved a lower average RMSE than the MBB method, indicating the increased accuracy. Fig. 4.14 shows that the mBBB method could further effectively reduce the RMSE of CPE estimation.

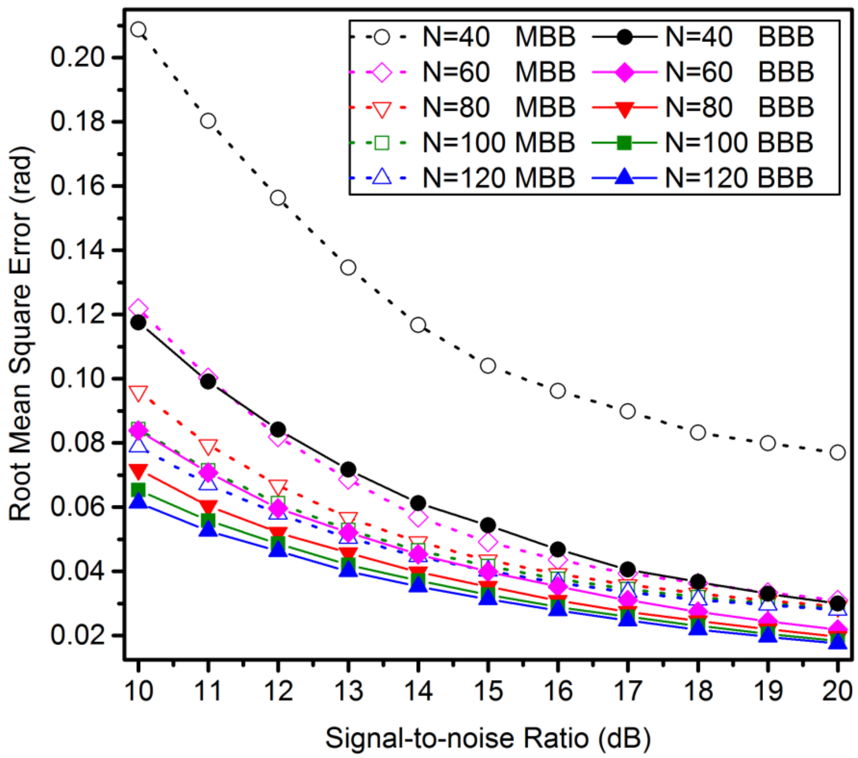

Fig. 4.13 Root mean square error of CPE estimation under different signal-to-noise ratio. N is the number of samples involved in the calculation of CPE using MBB method. Number of test phases used in MBB method is 20.

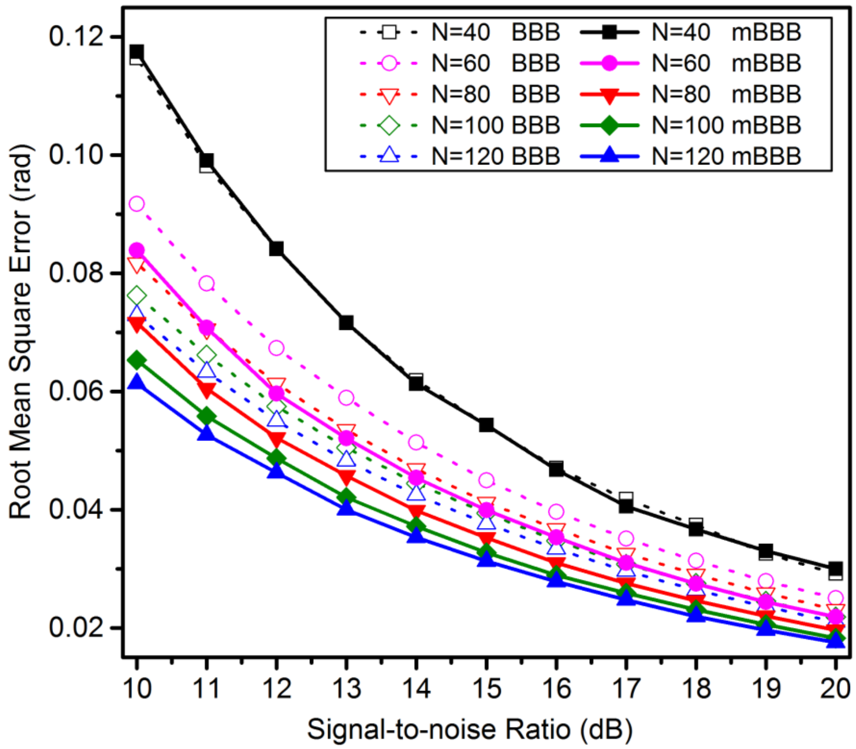

Fig. 4.14 Root mean square error of CPE estimation under different signal-to-noise ratio. N is the number of samples involved in the calculation of CPE using BBB method.

Linewidth tolerance

Another noise effect that may limit the performance of the proposed CPE estimation methods is the variance of laser phase noise, characterized by the laser linewidth. We have compared the tolerance against the laser phase noise for both QPSK-OFDM and 16QAM-OFDM signals, via simulations. The results, as depicted in Fig. 4.15, showed very similar laser linewidth tolerance among the cases of PA method, MBB method, and BBB method with or without edge de-noising.

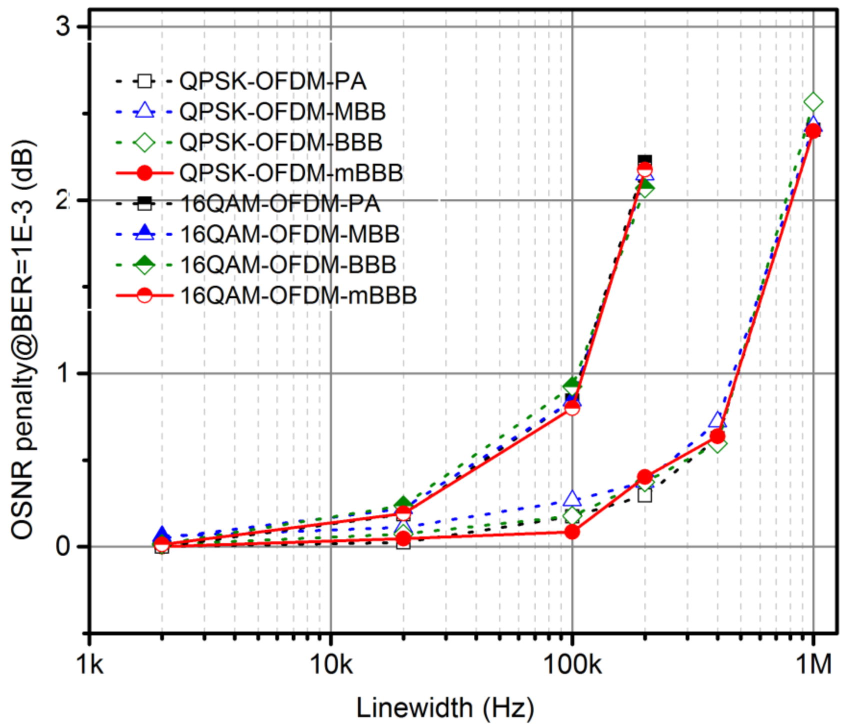

Fig. 4.15 OSNR penalty at BER=1E-3 for PA, MBB, BBB and mBBB algorithm.

Computation Complexity

With the help of pilot subcarriers, the pilot-aided method does not require much computation. At the receiver, the phases of the pilot subcarriers are averaged as the estimation of common phase error.

The minimum bounding box algorithm in [108] can be regarded as a modified blind phase searching (BPS) algorithm [112], which is a commonly used carrier phase recovery algorithm in single-carrier system. The comparison between MBB and BPS has been made in [108] and here we list the result in Table. 4.1.

The Rotating Calipers method after the convex hull is obtained in the proposed best-fit bounding box algorithm has the similar complexity as MBB, but with much reduced (up to ~10 times) required sources as shown in Section 4.3.1. However, the major complexity lies in the calculation of convex hull. Fortunately, as a key enabling algorithm in most image processing techniques, the calculation of convex hull has been well investigated and the complexity has been reduced to $O(N*log(N))$ via Graham Scan Algorithm [76] or even $O(N*log(H))$ via Chan's algorithm [78] if the number of points in the convex hull H is preset. In the Graham Scan Algorithm, there is an initial radial sorting process which needs a so-called "is-left" decision to decide the whether one point is in the counter-clock or clock-wise direction of the line determined by the origin and previous point [76]. This "is-left" process consists of 5 real additions and 2 real multiplications. After the sorting, each point is checked to determine whether it is in the convex hull by the same "is-left" calculation. In this step, each point is processed twice at most. Hence, $N*log(N)+2N$ "is-left" operations are required in total. Chan's algorithm can speed up this process to be $N*log(H)+2N$, and the preliminary process in Chan's algorithm is also the "is-left" operation. The mBBB algorithm needs more comparators and another BBB procedure more if outliers are found in the current convex hull. The hardware requirement of the worst case is also listed in Table 4.1.

Table 4.1 Hardware complexity comparison

	Multiplexer	Adder	Comparator	Decision
PA	*2*	*2K*	*0*	*0*
BPS	*6M·B+4M*	*6M·B-B+2M+2*	*M·B*	*M·B+M*
MBB	*4M·B+4M+B*	*2M·B+2B+2M*	*4M·B+B*	*0*
BBB	*5M(log(H)+2) + 4H·H+H+4M*	*2M(log(H)+2)+ 3H·H+H+2M*	*3M+3H·H*	*0*
mBBB	*2BBB_multi*	*2BBB_adders*	*2BBB_camp+8M*	*0*

* K is the number of pilot subcarriers; M is the number of samples in one OFDM symbol; B is the number of test phase in BPS and MBB; H is the expected size of convex hull.

Table 4.1 shows the comparison of the computation complexity between the proposed BBB algorithms and the PA, MBB and blind phase searching (BPS) algorithm. To be more specific, in our simulations and experiments, M = 128, B = 16, H = 16. Then the number of real multiplexers used in BPS, MBB, BBB and mBBB algorithms are 12800, 8720, 5392, and 9880, respectively. Meanwhile, the number of real adders used in BPS, MBB, BBB and mBBB are 12530, 4384, 2576 and 4472, respectively. It is clearly seen that the newly proposed BBB algorithm has 38.17% and 41.24% reduction in the requirement of real multiplexers and adders compared with previous MBB algorithm. Due to the additional BBB process, mBBB requires a little more hardware resource than MBB algorithm in the worst case, but still much less than BPS algorithm.

4.3.3 Experiments

Fig. 4.16 shows the experimental setup to verify the proposed CPE estimation schemes. The size of inverse fast Fourier transform (IFFT) was 256. Pseudo random binary sequence was mapped to 16-QAM symbols and loaded into 128 subcarriers. 16 pilot subcarriers were equally inserted in the 128 data subcarriers. Another one quasi-pilot subcarrier using the above mentioned mapping method was inserted in the front of the data subcarriers. The rest subcarriers were padded to be zero. The OFDM signal sequence was generated offline by personal computer and loaded to an arbitrary waveform generator (Tektronix 7122C) to generate radio-frequency (RF) OFDM signal with a sampling rate of 12 GSample/s.

Two narrow-linewidth tunable lasers were used as the signal laser and the local oscillator, with equal linewidth of ~100 kHz, resulting in an equivalent linewidth of ~200 kHz. The continuous wave from the signal laser was then modulated with the RF OFDM signal, as described above, via an optical IQ modulator. The generated optical OFDM signal was first amplified by an Erbium doped fiber amplifier (EDFA), followed by a variable optical attenuator (VOA), so as to emulate different OSNR values. The optical signal was then fed into a recirculating loop, which comprised a segment of 70-km single mode fiber, followed by an EDFA. The received optical signal was detected by a conventional coherent optical receiver. The electrical signal was then sampled by a real-time oscilloscope (Tektronix 72004B) at a sampling rate of 50 GSample/s for offline digital signal processing. Conventional OFDM synchronization and frequency offset compensation method [16] were employed. The channel estimation was implemented through training sequences.

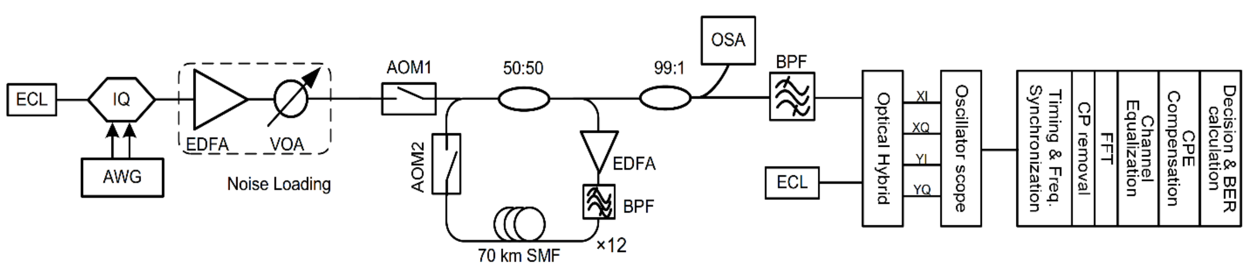

Fig. 4.16 Experimental setup. ECL: external cavity laser; AWG: arbitrary waveform generator; VOA: variable optical attenuator; AOM: acousto-optic modulator; OSA: optical spectrum analyzer; BPF: optical band pass filter.

First, we characterized the back-to-back (B2B) experiment. The bit error rate was calculated with different CPE methods at each optical-to-noise ratio (OSNR) value. Fig. 4.17 shows the bit error rate (BER) versus OSNR using the common PA method with the number of pilot-aided subcarriers ranging from 2 to 16, as well as that employing BBB method to compensate CPE with and without modification. The result shows that the BBB method had a comparable performance as the PA method with 16 pilots. Using the same experiment data set, we applied the MBB method with different number of test phases from 4 to 16 and the results were compared with that using the BBB method, as shown in Fig. 4.18. It could be clearly seen that the modified BBB method achieved the best performance. This could be attributed to that the BBB method does not have any limitation on resolution, as discussed.

To further investigate the tolerance of the proposed MBB and BBB methods against fiber nonlinearity, an 840-km transmission experiment was conducted. As seen in Fig. 4.16, the long-haul transmission was emulated, via a recirculation loop with 12 spans of 70-km single mode fiber. The input power into the recirculation loop was altered from -4 dBm to +7 dBm, in a step of 3 dB. The Q-factors were calculated, using PA, MBB and BBB methods, from 50000 OFDM packets at each input power value. Fig. 4.19 shows that the BBB method has a slightly performance improvement in the linear regime while its nonlinear tolerance was not as good as the PA or the MBB method. However, when the modified BBB was applied, the Q-factor improvement was significant, which was about 0.08 dB better than that with BBB method. Compared with the PA method, the Q-factor improvement at -1 dBm input power was ~0.15 dB. The results showed that the proposed BBB method has a comparable performance as the common PA method.

In general, conventional PA method has the least complexity, as it only calculates the phase average among all the pilot subcarriers. Nevertheless, our proposed BBB methods use a non-data aided approach to achieve comparable performance and much increased spectral efficiency than the conventional PA method, but at an expense of increased computation complexity. The computations involved are the common process adopted in image processing and hardware implementation friendly.

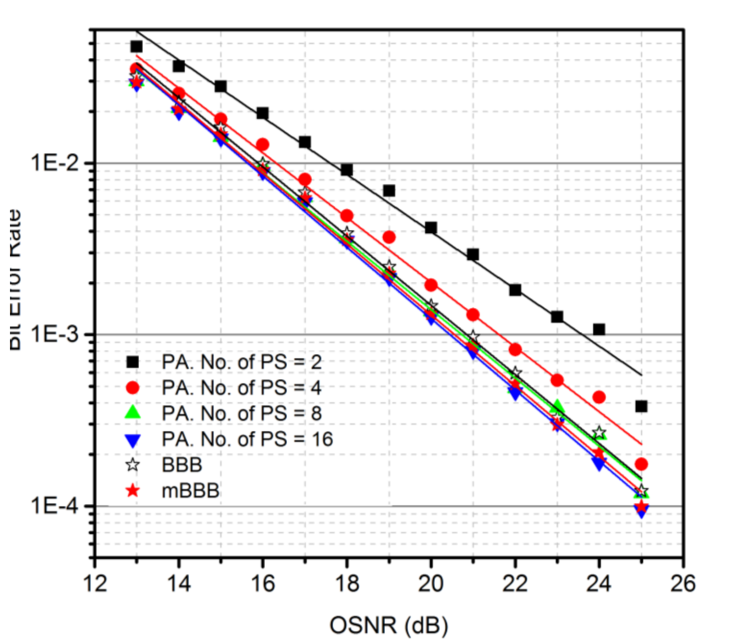

Fig. 4.17 Bit error rate versus OSNR. PA and BBB methods are used. Numbers of pilot subcarriers (PS) used in PA method are 2, 4, 8, and 16.

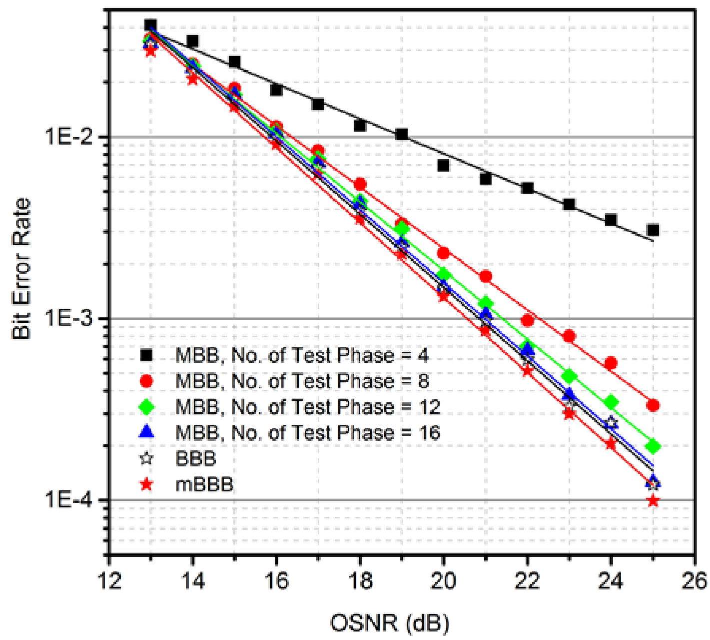

Fig. 4.18. Bit error rate versus OSNR. MBB and BBB methods are used. Numbers of test phase used in MBB method are 4, 8, 12, and 16.

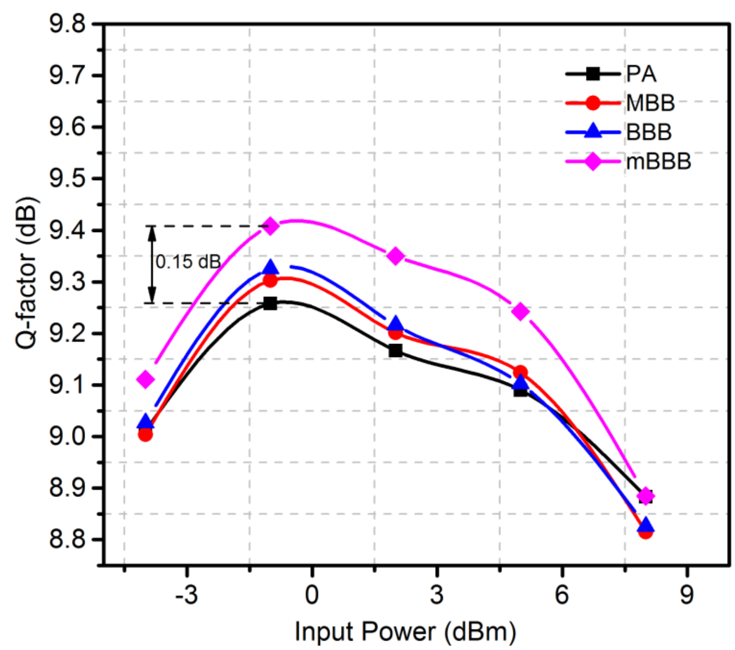

Fig. 4.19 Q-factor versus input power with PA method, MBB method, BBB method and mBBB method in 840-km single mode fiber transmission.

4.3.4 Conclusion

In this section, we have proposed a novel CPE estimation method based on the bounding box of the constellation diagram of the received samples in an OFDM symbol. The best-fit bounding box method have been investigated and characterized. A practical accuracy improvement algorithm has also been proposed. Both numerical simulations and experiments have shown that the proposed methods can realize substantial improvement in spectral efficiency and comparable performance, as compared with the common PA method. The performance of newly proposed BBB & mBBB methods outperform the performance of MBB method.

4.4 ICI compensation using match filters

4.4.1 Operating principles

As discussed in the previous section, laser phase noise can be modeled as a Wiener process with low-pass Gaussian distributed power spectral density (PSD). Hence, only several neighboring subcarriers are dominant [113]. The received data in one subcarrier can be seen as a weighted sum of several pairs of localized subcarriers. This low-pass property provides the possibility to use digital equalizers to compensate the ICI effect in CO-OFDM system.

The above discussions pave the way for the mitigation of ICI. Fig. 4.20(a) shows the equalization process at the CO-OFDM receiver side (inverse FFT (IFFT) and cyclic prefix (CP) removal are not shown). An ICI mitigation step can be added after CPE correction. The estimation of the filter coefficients here is based on least-mean-square (LMS) method. Fig. 4.20(b) shows the process of two algorithms of DSP filter coefficients estimation, i.e., decision-feedback (DF) [114] and feed-forward (FF) [113]. In DF, only a small number of pilots are needed to compensate the CPE for the tentative decision of the other subcarriers, which are then used for the filter coefficients estimation. The justification of using this DF algorithm is that only a small portion of the tentative decided symbols are erroneous [114]. Instead, more pilots are necessary in FF algorithm so as to achieve a comparable performance as DF. The sacrifice of transmission rate of FF reduces the computing complexity, compared to DF, since no decision-feedback is required. Moreover, the ICI mitigation step in DF can also function as CPE corrector, hence removing the CPE correction step before ICI mitigation. In this paper, we only use a 3-tap FIR filter for ICI mitigation. Only the interference induced by a pair of adjacent subcarriers is considered as aforementioned.

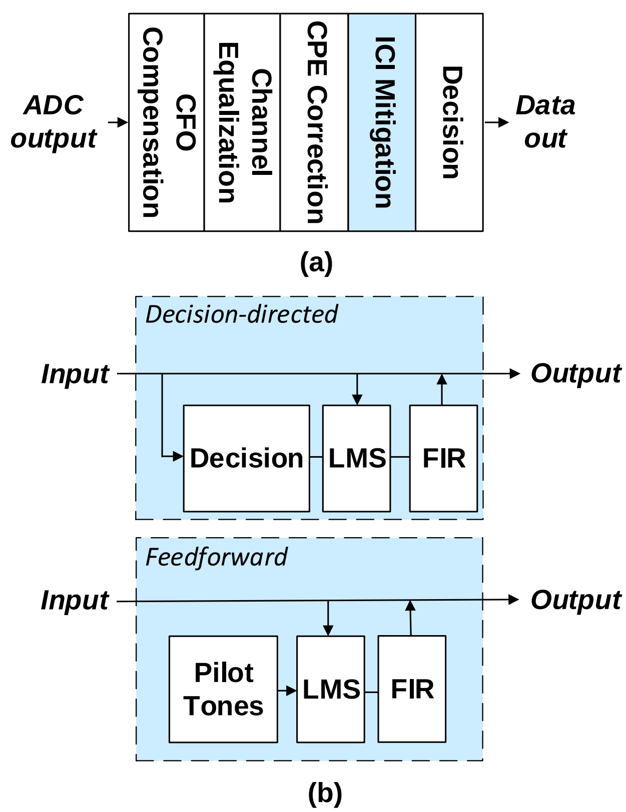

Fig. 4.20 (a) DSP process; (b) ICI mitigation process

4.4.2 Experiments and results

Experiments have been conducted to verify the effectiveness of the proposed scheme in mitigating ICI induced by PN. Fig. 4.21 depicts the experimental setup. The output of an external cavity laser (ECL) was modulated by an optical I-Q modulator, driven by the electrical signal from a Tektronix arbitrary waveform generator (AWG), operating at 12 GSample/s. The OFDM waveform was generated offline in MATLAB with a FFT size of 256, of which 128 was modulated with quadrature phase-shift keying (QPSK) data. A CP of 32 samples was added. Each OFDM symbol comprised 20 training symbols as the channel estimator and 512 data symbols. The OFDM data in the time domain after IFFT was then multiplied by a sequence of digitally generated random complex numbers so as to emulate the effect of PN [115]. The number sequence was specially designed, according to the model of PN.

The modulated signal was then fed into a piece of 20-km single mode fiber (SMF). A variable optical attenuator (VOA), followed by an Erbium doped fiber amplifier (EDFA) were used to control the signal power and the optical signal-to-noise ratio (OSNR). A portion of the signal was then split off to an optical spectrum analyzer (OSA) to monitor the OSNR, while the rest of the signal was fed into an optical coherent receiver for detection. A 0.88-nm bandwidth optical bandpass filter was inserted to filter out the out-of-band noise at the coherent receiver. A polarization controller was placed before the coherent receiver to align the input signal to only one polarization of the coherent receiver. The output of the coherent receiver was captured with a digital sampling analyzer (DSA) and was offline processed under MATLAB. The number of pilot tones for ICI mitigation in FF algorithms was set to be 24, while in the case of DF, 8 subcarriers were used as pilot tones for CPE correction, prior to tentative decisions. The BER was calculated by counting the number of errors over 5000 data symbols.

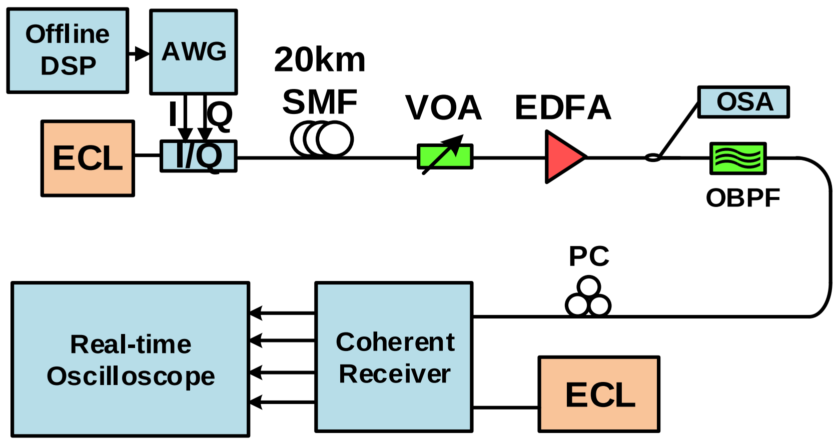

Fig. 4.21 Experimental setup. ECL: external cavity laser; AWG: arbitrary waveform generator; VOA: variable optical attenuator; OSA: optical spectrum analyzer; OBPF: optical band pass filter; PC: polarization controller.

Fig. 4.22 shows the experimental results of PN mitigation under difference OSNR values, different laser linewidths (100 kHz, 1 MHz, 2 MHz), and different ICI mitigation schemes (ICI-DF, ICI-FF). The results were compared to that with only CPE correction. It could be seen that when the 3-dB laser linewidth was 100 kHz, the ICI mitigation algorithm achieved nearly no obvious improvement in BER performance. However, when the laser linewidth was increased to 1 MHz, the performance improvement was quite obvious. The required OSNR at BER=10^{-3} was reduced by about 3 dB. When the laser linewidth was 2 MHz, the BER performance without PN mitigation even could not reach the level of 10^{-3}, while the OSNR requirement to reach this threshold was 12 dB. Therefore, the proposed method was remarkably effective in mitigating the PN. On the other hand, the performances of the ICI mitigation schemes using DF and FF were almost the same.

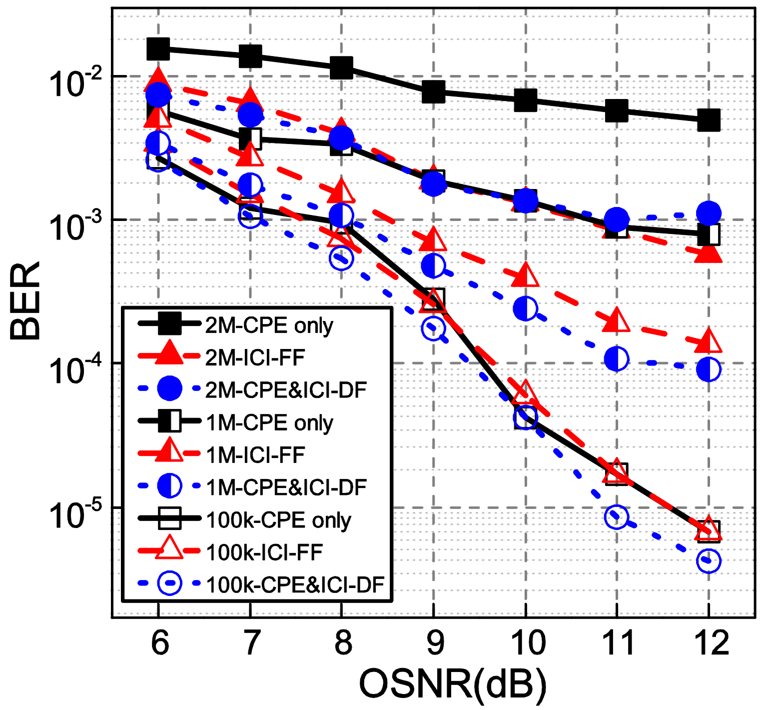

Fig. 4.22 Experimental results (legend: laser linewidth in Hz-DSP algorithm-DF or FF).

4.4.3 Simulation results and discussions

We have also simulated the performance of the proposed algorithm in jointly combatting the ICI induced by RFO and PN. The setup for the emulative study was the same as that in the experiment. The OSNR was fixed at 8 dB. The ICI mitigation scheme adopted was FF, which saved CPE estimation in DSP. Hence the comparison of DSP algorithms was between the cases of only CPE correction and only ICI mitigation. The laser linewidth was set to be 1 MHz, as well as 0 Hz (i.e., ideal single tone laser), as the benchmark of merely RFO mitigation, respectively. The RFO was varied from 0 to 5 MHz (negative RFOs were neglected due to the symmetry of the EVM performance). Fig. 4.23 depicts the EVM values of the given linewidth and RFO under different DSP algorithms.

When the laser linewidth was set at 0 Hz, the differences of the EVM values between the cases with and without ICI mitigation proved that the proposed ICI mitigation method could sufficiently compensate the ICI induced by RFO. When the laser linewidth was 1 MHz without ICI mitigation, the EVM deteriorated drastically when RFO increased. With the help of ICI mitigation, EVM could be largely reduced, indicating a remarkable mitigation of ICI induced by RFO. Specially, when the case laser linewidth was 1 MHz and RFO was 0 Hz, the 5% decrease of EVM achieved by ICI mitigation should be attributed to the mitigation of PN. When the RFO was 3 MHz with no PN, the EVM reduction brought by RFO compensation only was 3%. The ICI mitigation algorithm could reduce the EVM by about 8% in case of 3-MHz RFO and 1-MHz linewidth, indicating that the ICI induced by PN and RFO were simultaneously mitigated.

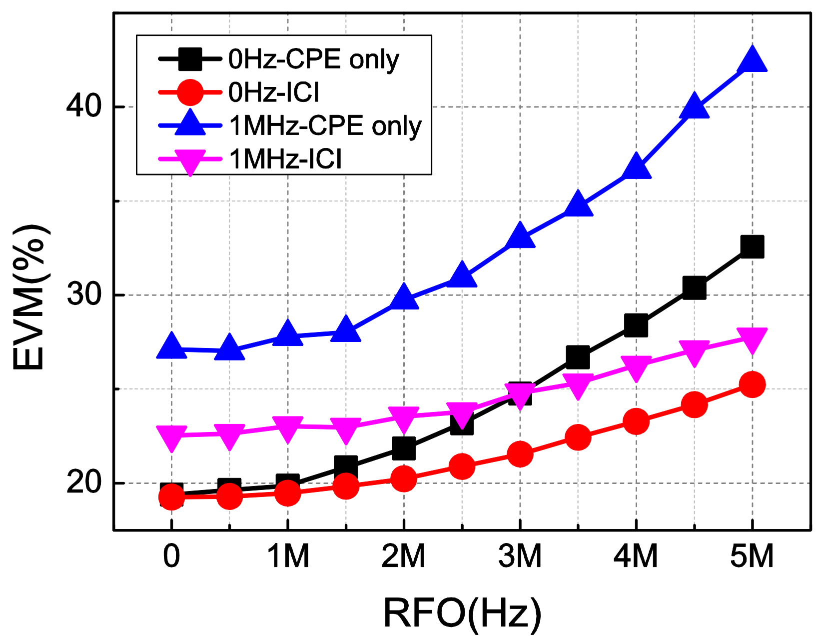

Fig. 4.23 Simulation results (legend: laser linewidth -DSP algorithm).

4.4.4 Conclusion

In this section, we have proposed and experimentally demonstrated a new ICI mitigation method, which can mitigate the performance penalty caused by laser phase noise. It is further shown that when there exists residual carrier frequency offset, the ICI caused by PN and RFO can be simultaneously mitigated.

4.5 Summary

We have proposed two novel CPE estimation methods based on the bounding box of the constellation diagram of the received samples in an OFDM symbol. The best-fit bounding box method has been investigated and characterized. A practical accuracy improvement algorithm has also been proposed. Both numerical simulations and experiments have shown that the proposed methods realize substantial improvement in spectral efficiency and comparable performance, as compared with the common PA method. A digital-equalization-enabled ICI compensation method has also been proposed for CO-OFDM system in this chapter.

Chapters 5 Blind modulation formats using image processing techniques

5.1 Introduction

Recently, management of optical networks is progressing more flexible and software-defined. Fully programmable bandwidth variable transponders are adaptive to the data rate and the modulation format, based on the transmission length and channel state information so as to increase the spectral efficiency and assure the quality of service. In particular, it is highly desirable to have the receivers being able to automatically recognize the signal's modulation format, hence proper digital signal processing (DSP) algorithm can be applied to achieve the optimum performance for the received optical signal. Another application that requires modulation format recognition (MFR) is the coherent burst mode transmission system, in which the coherent receiver is required to respond to the fast channel switching.

Several MFR schemes have been recently proposed, recently. In [85], the polarization demultiplexed power distribution was used to identify the modulation formats, but it highly depended on the optical signal-to-noise ratio (OSNR), thus an additional OSNR monitoring module was required [86]. In [84], the feature of directly detected amplitude histogram was applied to an artificial neural network (ANN). With enough training process, the ANN could recognize modulation formats. However, it required too much training, especially when the channel impairments like chromatic dispersion (CD) and polarization mode dispersion (PMD), were taken into consideration. The Stokes space based algorithms were promising as they were inherently tolerant to the carrier phase noise, the frequency offset as well as polarization mixing [87, 88]. However, these methods were based on the computation-extensive iterative K-means or expectation maximization methods, which hindered their practical implementation.

To support fast switching in both software-defined network and burst-mode transmission systems, the modulation format recognition time is a critical issue. Therefore, the complexity of the MFR algorithm needs to be as small as possible. In this chapter, we summarize our work on using image processing techniques to recognize modulation formats in a fiber-optic transmission system. It shows a great reduction in the complexity and provides a creative tool set for the digital signal processing in optical communication systems.

5.2 MFR based on CCA

5.2.1 Introduction

In this section, we show a novel modulation format recognition algorithm based on connected component analysis in binary image processing and the corresponding simulation and experiment demonstration. It shows high accuracy and much reduced complexity than conventional clustering-based methods.

5.2.2 Principles

At the coherent receiver, it is common to perform analog-to-digital conversion, chromatic dispersion compensation and timing recovery, before handling the modulation format [36]. After these pre-processing, in our proposed blind modulation recognition scheme, the dual polarizations signal in the Jones space is first converted to the Stokes space, by [87]

$$\left[s_0, s_1, s_2, s_3\right]^T = \left[\left|X\right|^2 + \left|Y\right|^2, \left|X\right|^2 - \left|Y\right|^2, 2\Re\left\{XY^*\right\}, 2\Im\left\{XY^*\right\}\right]^T \tag{5.1}$$

where X and Y represent the two orthogonal polarizations, while $\Re\{\ \}$ and $\Im\{\ \}$ stand for the real and the imaginary parts of a complex number, respectively. $[.]^T$ is the matrix transpose operation. As the absolute phase information has been removed in the transformation, the laser frequency offset and carrier phase noise have no effects in the Stokes space. From (5.1), we can conclude that phase-shift-keying (PSK) signals distribute on the plane s_1=0 in the Stokes space as they have constant amplitudes, while the quadrature amplitude modulation (QAM) signals distribute in several discrete and symmetric planes that are parallel with plane s_1=0.

If we project the 3-dimentional (3-D) Stokes vector space to a 2-D plane which is parallel to the s_2-s_3 plane, we obtain the constellation diagram, as shown in Fig. 5.1(d)-(f) for BPSK, QPSK and 8PSK, respectively. For the QAM signals, the amplitude is not constant, and its distribution on the 3-D Stokes space is complicated. Fig. 5.2(e) illustrates the distribution of a polarization multiplexed (PM) 16QAM signal, which has 60 clusters of points. As seen in Fig. 5.2(g), simply projecting these points to s_2-s_3 plane cannot differentiate each constellation point easily, even at relatively large signal-to-noise ratio (SNR), due to the small Euclidean distance. In principle, 16QAM has three different amplitudes, thus the theoretical values of s_1 after transformation and normalization are {-4/9, -2/9, 0, 2/9, 4/9}. This distribution can be clearly seen, if we rotate Fig. 5.2(e) with a certain angle of view, as in Fig. 5.2(f). If we only project the outermost two symmetric planes (p_2 and p_2') to the s_2-s_3 plane, a simple four-point constellation (Fig. 5.2(h)) can be obtained.

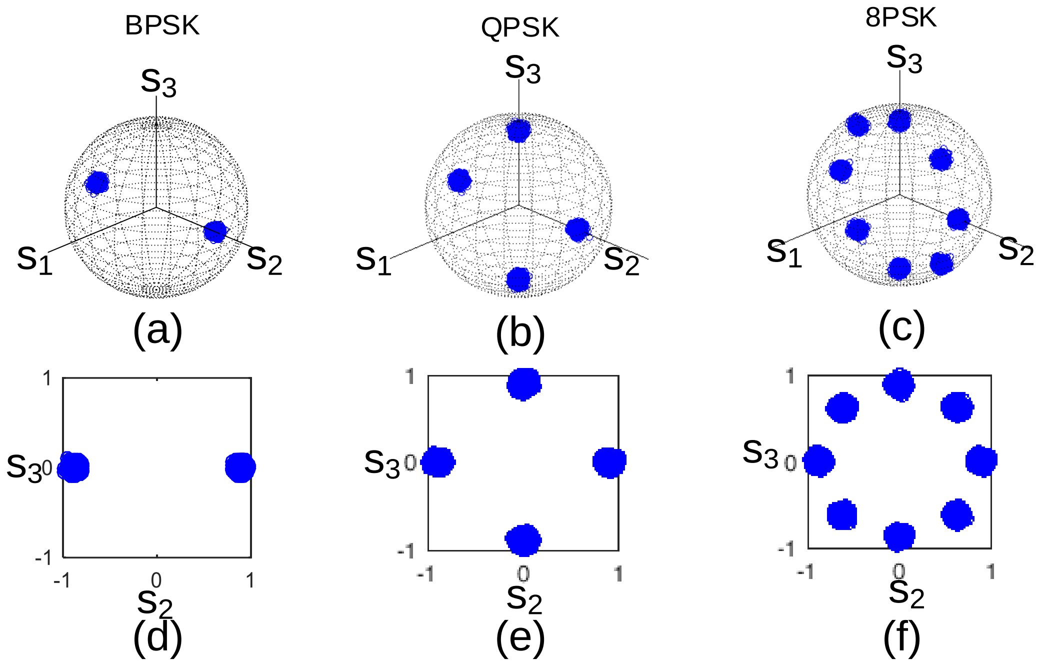

Fig. 5.1 Stokes representation of PSK signals

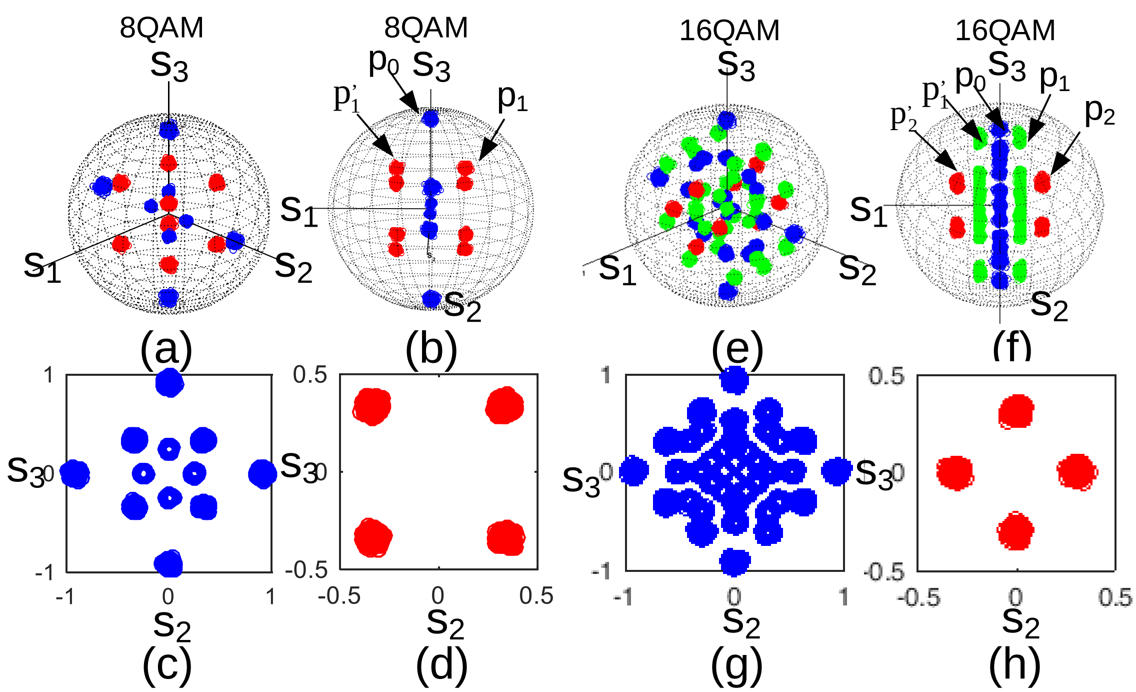

Fig. 5.2 Stokes representations of QAM signals

Fig. 5.4(a) illustrates the flow chart of our MFR algorithm. Polarization tracking is performed first, after the Stokes conversion and normalization of s1 to s3 values with s0. The method proposed in [116] is utilized, by which a least square fit plane is found with only several hundreds of received data points, whose normal identifies the state of polarization (SOP). A 3×3 rotation matrix is generated based on the normal of least square fitting plane and used to recover the initial polarization of received data. It is worth noting here the simple polarization tracking does not equal to the conventional polarization de-multiplexing because no equalization is performed. Besides, the normal can be used as the initial coefficients of the subsequent polarization de-multiplexing equalizers. Afterward, the data slicing is performed based on the s1 value of the received symbol. Only the outermost plane of the 8QAM and the 16QAM are selected for the projection as in [117]. The plane flag is obtained based on which part of data are chosen, whose value is 0, 1, 2 for PSK, 8QAM, and 16QAM signals, respectively. The last step of pre-processing is the Voronoi diagram based density filtering [117]. The Voronoi diagram of the points in the projected plane is generated, and the inverse of the each Voronoi cell's area is used to estimate the density of each point. After normalization of the area to be within (0, 1], a threshold is defined and the points with their estimated density below the density threshold are removed, as seen in Fig. 5.3(a) & (b).

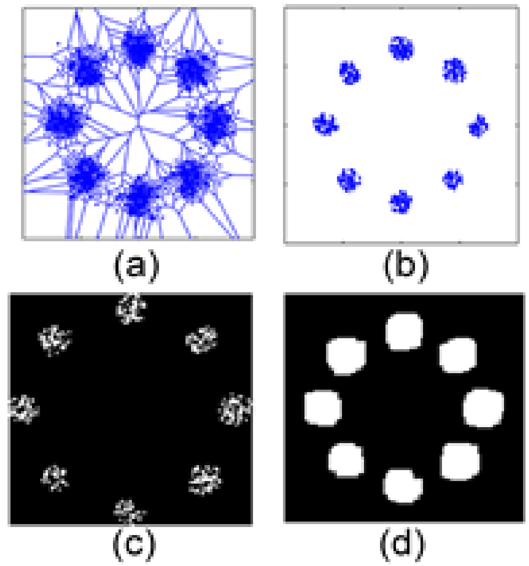

Fig. 5.3 (a) Voronoi diagram of the s_2-s_3 projection of a PM-8PSK signal with SNR = 18 dB; (b) filtered constellation diagram; (c) converted binary graph; (d) binary graph after averaging filter.

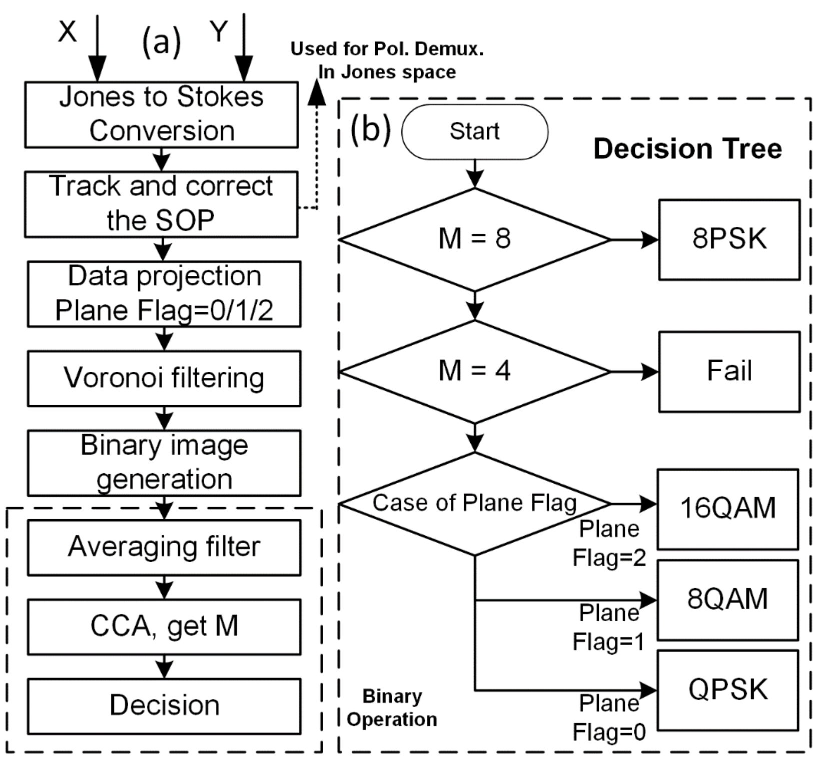

Fig. 5.4 (a) Flow chart of the algorithm (b) Decision tree.

Now it comes to the image processing process. First, a binary graph is generated dependent on the survived points in the previous preprocessing step. The survived points are normalized with both s_2 and s_3 within (0, N], where N is an integer and defines the resolution of generated binary image. Each data point after the density filtering is now filled into one of the $N \times N$ grids. If there is any point falling into the grid, the grid is assigned with value "1", otherwise it is "0". The gridding procedure is analogous to the "quantization" in digital communication system, and can be easily implemented via rounding operations on the normalized data points. The second step is average filtering. It is highly required before the next step as it can smooth the data set in the binary image and increase the recognition accuracy. It is simply a bidirectional 2-D smoothing filter applying on the binary graph. Fig. 5.3(d) denotes the effect after AF. The final step is the connected component analysis (CCA) [118]. It regards one pixel together with its adjacent 4 or 8 pixels as connected component. Here we utilize the 8-connectivity as defined in (2.26). The algorithm traverses all the pixels and outputs the number of subsets in which each pixel is connected with neighboring pixels. Detailed implementation of the algorithm can be found in [118], which runs in $O(n)$ time. After that, the number of data set is used as an identifier of different modulation formats. Fig. 5.4(b) illustrates the decision tree based on number of data set.

It is difficult to support 32QAM or even higher order QAM in the Stokes space based MFR algorithms. In the Stokes space based MFR algorithms, the highest order of QAM they could support was also 16. It was because the total number of clusters in the Stokes space would become too large when the order of QAM was higher than 16, making it difficult to distinguish its constellation points. For example, the number of 16-QAM signal in the Stokes space has reached 60. As pointed out in our previous work of CCA-based MFR algorithm, simply projecting the 60 clusters to the 2-D plane makes the image processing fail to work. That is why we have to select the points in the outermost to do the projection.

However, only using the outermost points has its shortcomings due to much fewer points in the 3-D Stokes space being projected. This increases the required number of data symbols for successful MFR and thus increases the computation complexity. On the other hand, when the order of QAM signal becomes larger, even though we can use the same data slicing method to do the projection, but the threshold of slicing for different modulation formats will be much closer, thus more vulnerable to the noise.

5.2.3 Simulations and results

We have performed numerical simulations for the proposed MFR. 32-Gbaud PM-QPSK, PM-8PSK and PM-16QAM signal were generated and passed through a channel with additive Gaussian white noise. The converted binary image had a size of 100*100 pixels. The threshold for the Voronoi filtering and the size of averaging filter were optimized and kept identical for each modulation format. First, the OSNR value was varied from 10 dB to 30 dB, with a step of 0.2 dB, each having 500 independent implementations. The correct recognition rate was then calculated. Fig. 5.5(a) and (b) show the correct recognition rate under different OSNR values, and different number of points involved in the MFR. The OSNR, in the latter case, was set to be 15 dB, 22 dB, and 22 dB for QPSK, 8PSK and 16QAM, respectively. It could be noticed that only ~4000 symbols were required to correctly recognize QPSK and 8PSK, while 16QAM needed ~10000 symbols. This might be attributed to the small part of the received symbols on the slicing plane. It was worth noting that the number of symbols required was much fewer than those in the previously reported schemes (4-12×10^4 symbols in [85] and 8×10^4 symbols in [87]).

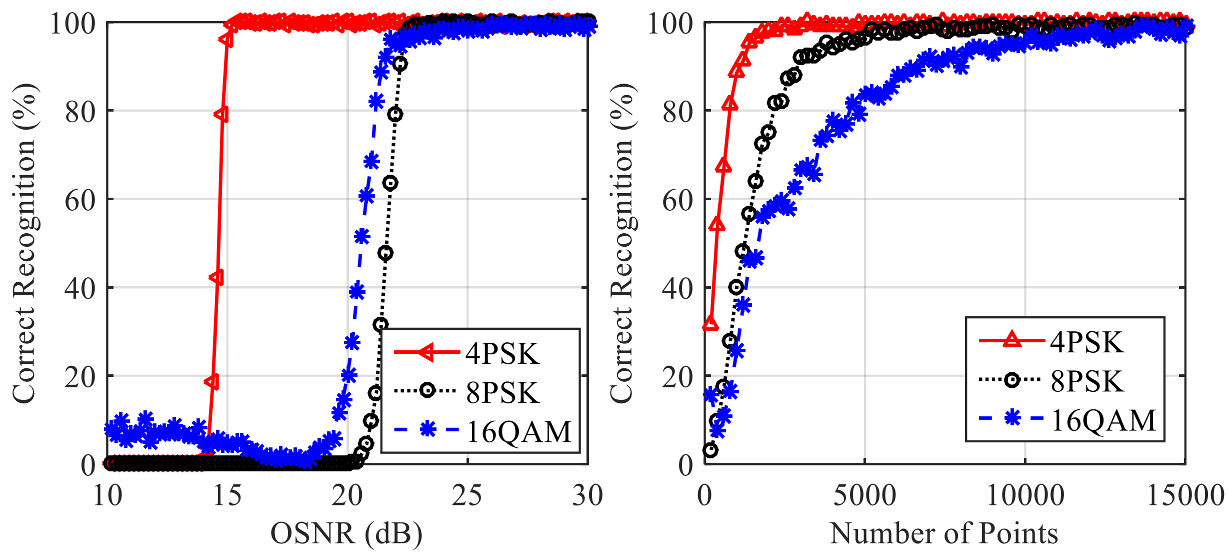

Fig. 5.5 Simulation results. (a) Correct recognition rate under different OSNR values; (b) Correct recognition rate under different number of points.

5.2.4 Experiments and results

Fig. 5.6 shows the experimental setup. 32-Gbaud PM QPSK (128 Gbps) and 16QAM (256 Gbps) signal were generated from a programmable pattern generator (PPG) to modulate a 1550-nm continuous-wave from an external cavity laser (ECL), via an in-phase and quadrature modulator. Polarization multiplexing was realized via a polarization multiplexer, which comprised a polarization beam splitter (PBS) to half the signal into two branches, an optical delay line to remove the correlation between *x*- and *y*-polarizations and a polarization beam combiner (PBC) to re-combine the signal. The noise was loaded with an 80/20 coupler and a noise source. At the receiver, a tunable optical filter with the 3-dB bandwidth of 0.35 nm was used. Another ECL was used as the local oscillator (LO). A polarization-diversity 90-degree hybrid was used to realize the polarization- and phase-diversity coherent detection of the LO and the received optical signal before balanced detection. The received signal was then sampled at 80 GSamples/s for offline signal processing. 4000 (10000) symbols for QPSK (16QAM) were used for MFR.

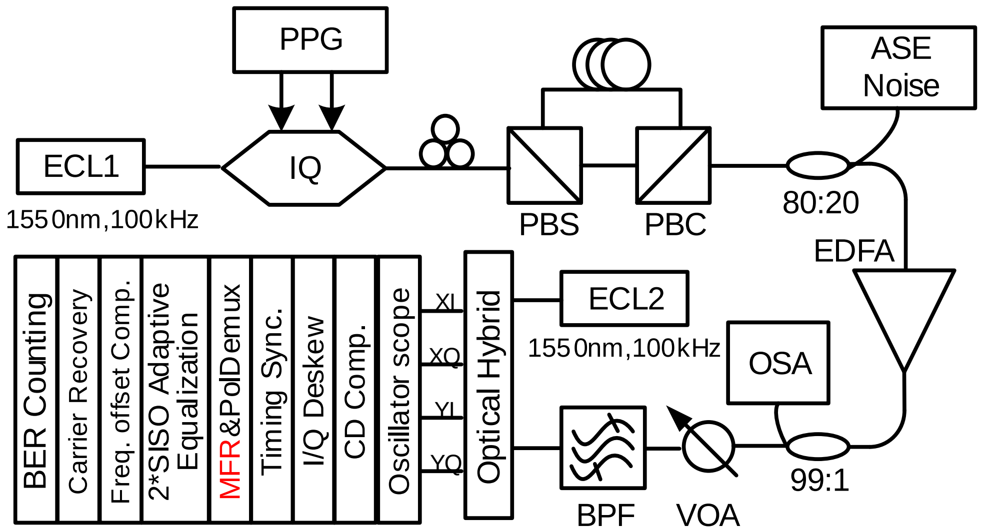

Fig. 5.6 Experimental setup. ECL: external cavity laser; (b) PPG: pulse pattern generator; PBS: polarization beam splitter; PBC: polarization beam combiner; VOA: variable optical attenuator; BPF: band pass filter; CD: chromatic dispersion; Sync.: synchronization; SISO: single input single output; Freq.: frequency.

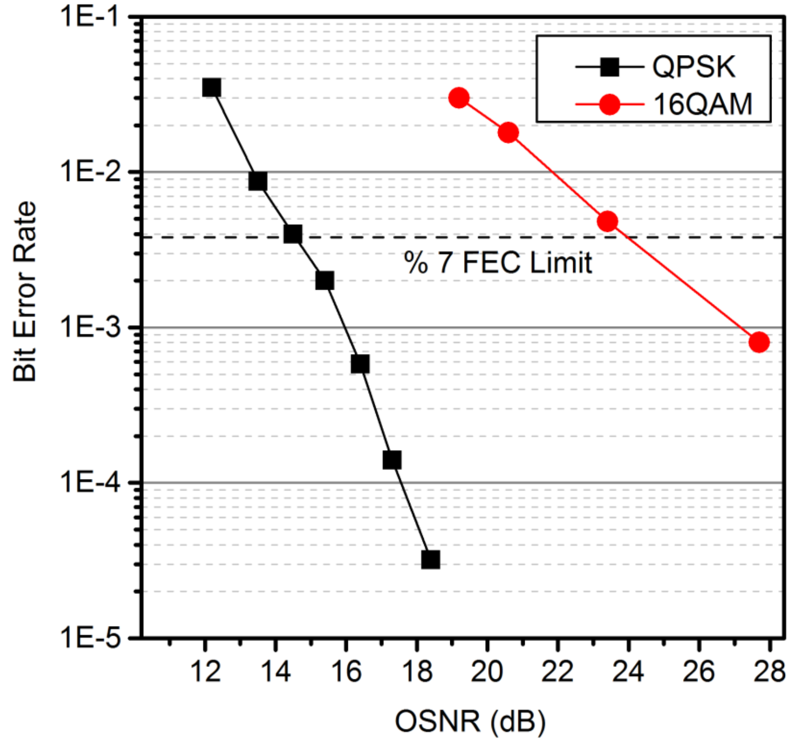

Fig. 5.7 Bit error rate performance with different OSNR (0.1-nm bandwidth)

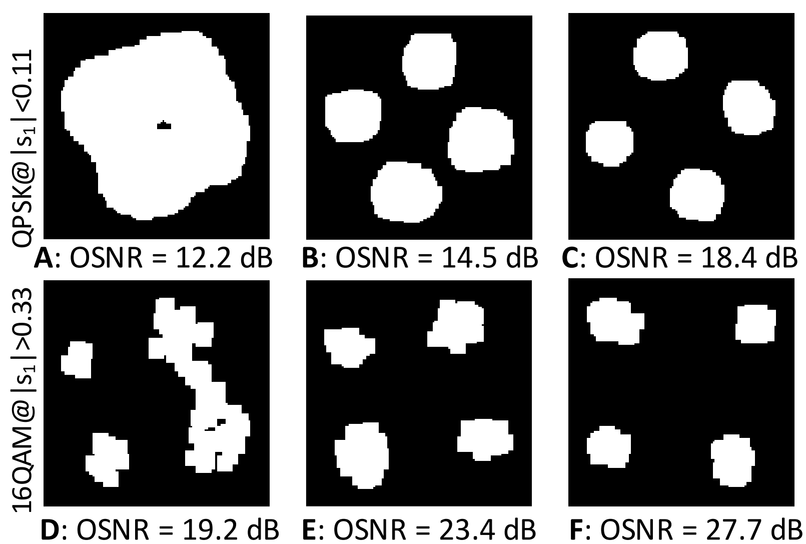

Fig. 5.8 Recognition results of PM-QPSK (up row) and PM-16QAM (lower row) signals.

Fig. 5.7 and Fig. 5.8 show the experiment results. The bit error rate performances and the final binary images before CCA algorithm were shown. The modulation format of the signal with an OSNR value at around 7% forward error correction limit could be recognized correctly. The experimental results agreed with simulation results very well.

5.2.5 Conclusion

In this section, a new low-complexity modulation format recognition method based on connected component analysis technique in computer vision have been proposed and verified, via simulations and experiments, to distinguish between PM-QPSK and PM-16QAM signals.

5.3 Characterization

In this section, we discuss the principle of the previous MFR algorithm in more detail. Extensive characterization of three key parameters in the algorithm, namely the threshold of density filter (DF), the size of averaging filter (AF) and the number of points required under different OSNR values in the MFR process has been investigated via numerical simulation. Simulation results show that there exists a common parameters set that support all the modulation formats we try to recognize. A brief complexity comparison with other Stokes based recognition algorithms has been made and the image processing techniques show advantages in computation complexity. Hence, the CCA based blind MFR algorithm proves to be a robust and practical method in the MFR algorithms.

5.3.1 Parameters optimization

In this section, we perform numerical simulations to investigate the three parameters aforementioned. Fig. 5.9 shows a simplified block diagram of the system configuration. 32 Gbaud optical PM-QPSK, PM-8PSK, PM-8QAM and PM-16QAM signals were generated via a general IQ modulator. Only chromatic dispersion and power loss were taken into consideration in the fiber transmission model. The Erbium-doped fiber amplifiers (EDFA) module was used to adjust the signal OSNR value (normalized into 0.1nm) under the assumption of additive Gaussian white noise model. The polarization of the optical signal varied randomly to emulate polarization walk-off in the fiber. The linewidths of both the laser in the transmitter and the local oscillator were set to be 100 kHz. The carrier frequency offset between the local oscillator and the transmitter side was set to be 10 MHz. After coherent detection and digitization, the signal was first converted into Stokes space via (5.1), followed by chromatic dispersion compensation and timing recovery. After that, our proposed MFR algorithm was applied.

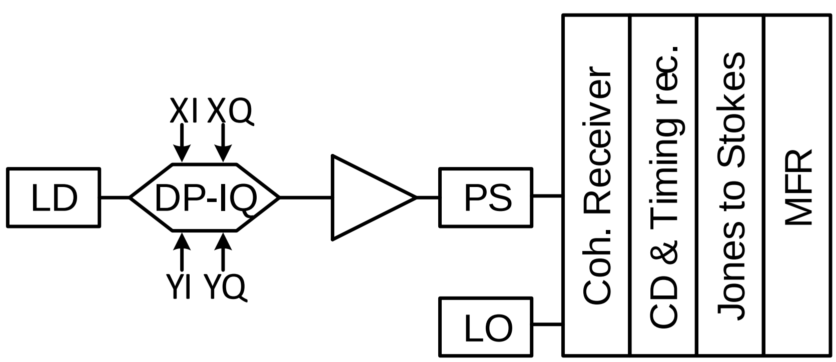

Fig. 5.9 Simulation setup. LD: laser diode; IQ: in-phase/quadrature modulator; PS: polarization scrambler; Coh.: coherent; rec.: recovery; Pol.: polarization.

In the simulation, 500 independent data packets for each case under investigation were tested by our proposed MFR algorithm, and the rate of successful recognition was calculated and used to evaluate the effect of certain parameter. We investigated the successful rate with respect to the threshold of DF, the size of AF, and the symbol length in the data packets, respectively. In each case, a reasonable range of OSNR values according to the modulation format were considered. The parameters of our MFR algorithm used in the simulation are listed in Table 5.1.

Table 5.1 Simulation parameters

MF	N	OSNR (dB)	DF	AF	SL	$\|s_1\|$
QPSK	100	13-18	0.05-1	1-20	200-10k	< 0.1
8QAM	100	18-24	0.05-1	1-20	200-10k	0.3-0.4
8PSK	100	22-28	0.05-1	1-20	200-10k	< 0.1
16QAM	100	24-30	0.05-1	1-20	200-20k	> 0.4

MF: Modulation format; DF: density filter; AF: averaging filter; SL: symbol length

Fig. 5.10 shows the successful recognition rates of the four tested modulation formats with the threshold of DF ranging from 0 to 1. The AF size was set to be 7 in each case. In principle, the signal with lower OSNR value required higher DF threshold for successful recognition, which could be noticed in Fig. 5.10. There was a valid range of DF thresholds for each modulation format under a certain OSNR value, which became larger as the OSNR increased. As seen from Fig. 5.10 even for a smaller OSNR value that was close to the boundary of successful recognition, there was a clear common set of DF values that supported successful recognition rate larger than 95%, for each modulation format. Meanwhile, as seen in Fig. 5.11, the AF dependency of these modulation formats exhibited a similar trend. The DF threshold was set to be 0.65. The recognition rate with small AF size (smaller than 4 in Fig. 5.11) was quite low until AF with enough size was applied. However, when the AF size was larger than a certain threshold, the CCA algorithm gave smaller output, as some of the subsets overlapped. This AF threshold increased with OSNR value, due to clearer and smaller size of the subset in the binary image at higher OSNR. These common value sets for every modulation format could be useful for practical implementation. Fig. 5.12 shows the required symbol length under different OSNR values. Only 16QAM required more than 10000 data symbols for a successful rate larger than 95%, while 3000 symbols were already enough for the rest of the three modulation formats to achieve the same successful rate.

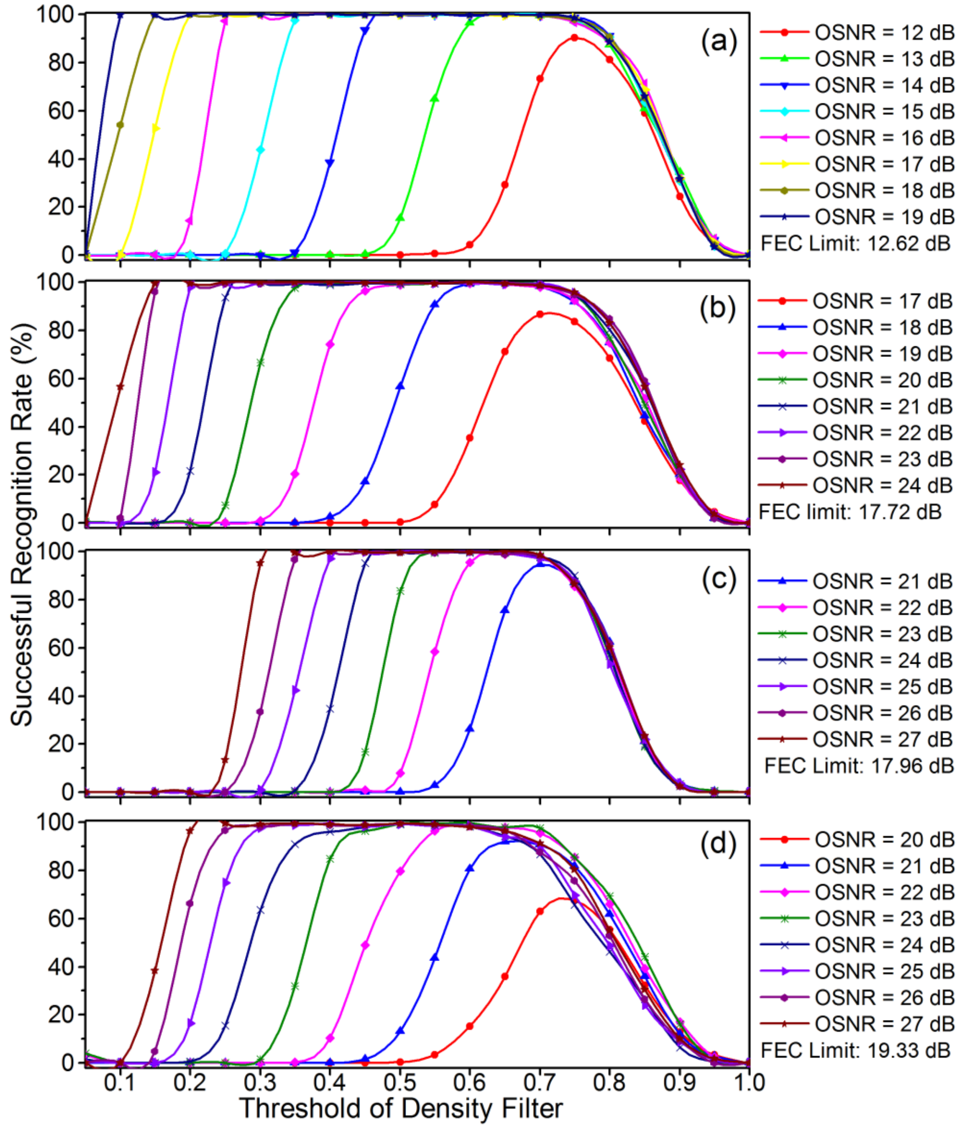

Fig. 5.10 Successful recognition rate w.r.t different thresholds of density filter. for (a) QPSK, (b) 8QAM (c) 8PSK and (d) 16QAM

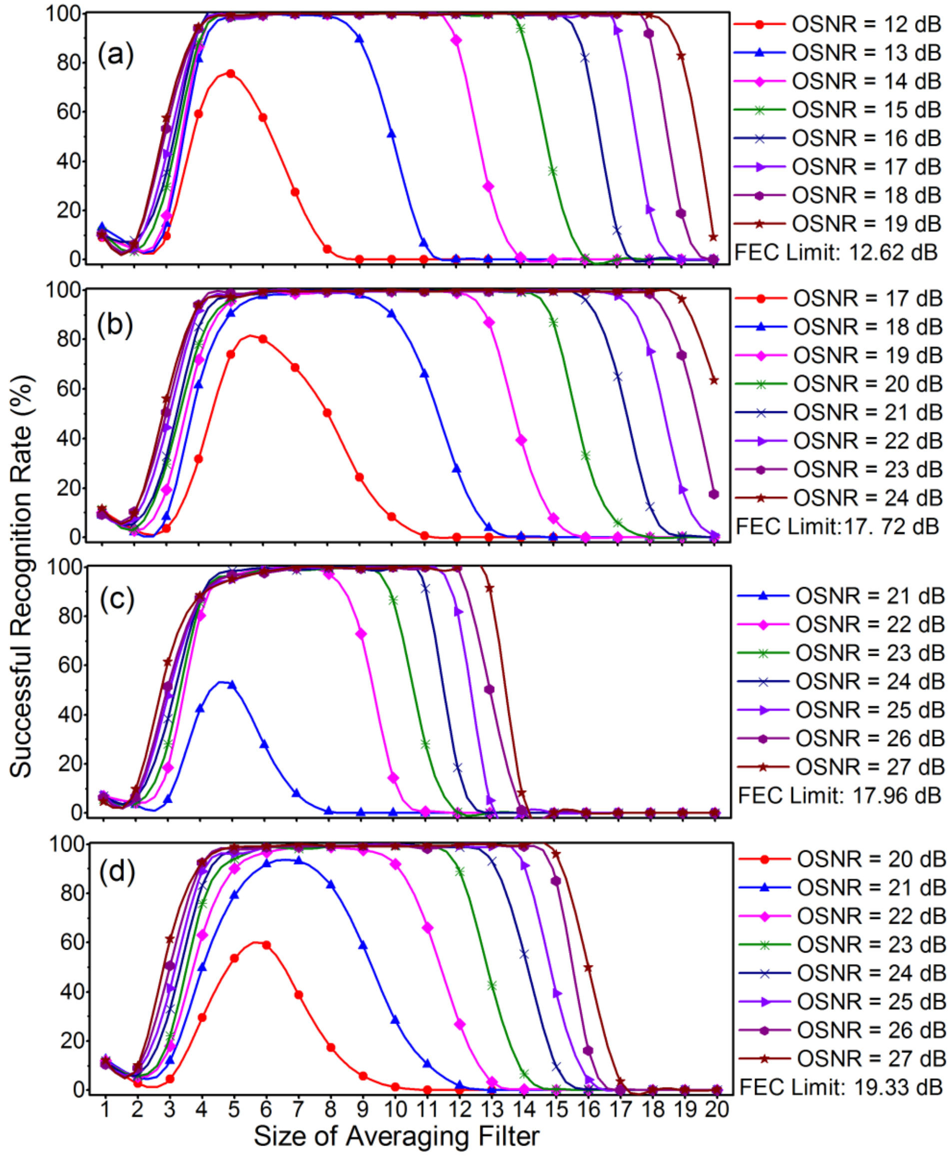

Fig. 5.11 Successful recognition rate w.r.t different size of averaging filter for (a) QPSK, (b) 8QAM (c) 8PSK and (d) 16QAM

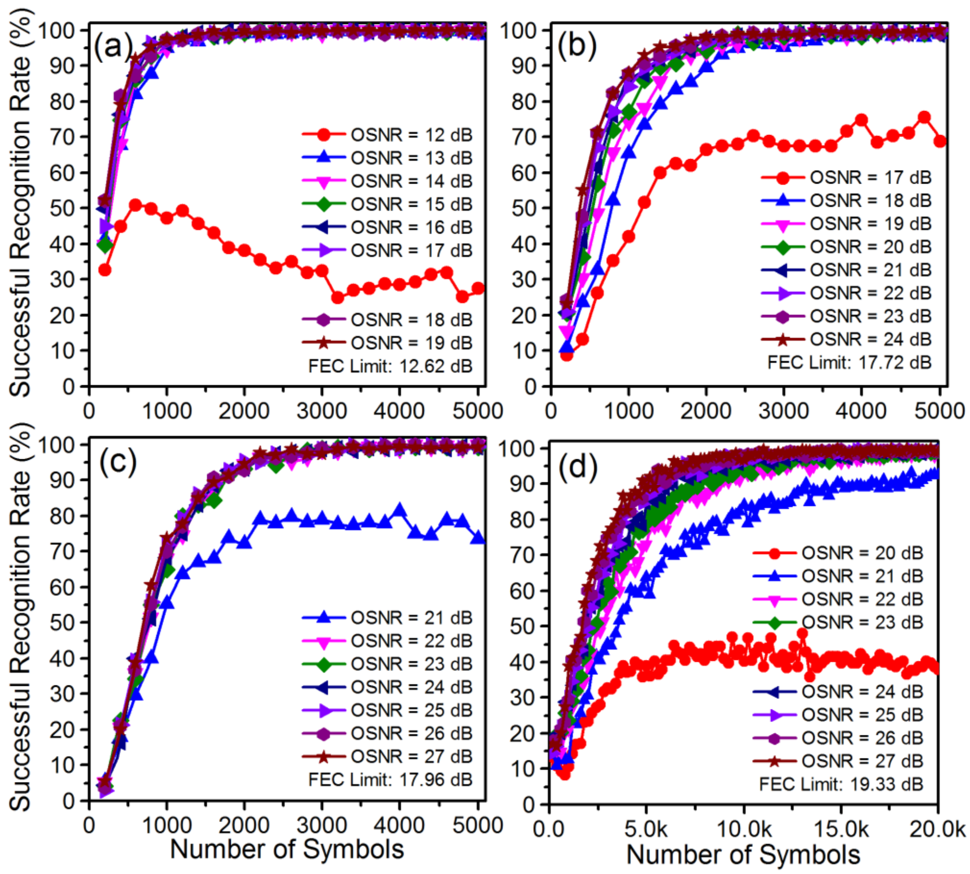

Fig. 5.12 Successful recognition rate with different symbol length for (a) QPSK, (b) 8QAM (c) 8PSK and (d) 16QAM.

5.3.2 Complexity comparison

In this section, we briefly compare the computation complexity between the proposed scheme and K-means based algorithm. As shown in [88], K-means has even smaller computation complexity than that of expectation maximization (EM) based algorithm [87] and has comparable complexity with other machine learning algorithms. Besides, the complexity of the K-means algorithm is easy to evaluate, as the operations in each iteration mainly comprise the calculation of Euclidean distance. In each iteration, the distance between each point to the current cluster centroid that it belongs to, is calculated, followed by updating the new centroid for each cluster at the end of the iteration. Assume the number of data symbols is N, the number of clusters is K, and M iterations are required to converge, in total. Then, about M×O(NK+K) primitive operations are needed.

In our proposed algorithm, the most computation extensive process is the Voronoi diagram generation, while the complexity of the image processing part is relatively moderate. In the well-known Fortune's algorithm [95] for Voronoi diagram calculation, there are two kinds of operations, namely site event and circle event, in the algorithm implementation. The number of site events is N, and that of the circle events is at most ($2N-5$). Each event can be executed in O(log N) time with the same number of primitive operations, in the worst case. Therefore, the total complexity is O($N\log N$). The area calculation is implemented in O(N) time.

It is worth noting that K-means algorithm is performed in 3-D space, while our method uses 2-D points in the calculation. Besides, K-means algorithm needs to test every possible K value for the modulation format, so the total K is 4+8+16+60=88 if only QPSK, 8PSK, 8QAM, and 16QAM are considered. Considering the number of iterations, M, our non-iterative approach outperforms K-means algorithm in computation complexity.

5.3.3 Conclusion

In this section, we have characterized and evaluated the CCA-based blind MFR algorithm for general coherent optical receiver, via numerical simulations. Various parameters, including the threshold of density filter, the size of averaging filter and the number of data samples required for successful recognition, are extensively investigated for various signal modulation formats. It is practical and simple for general coherent optical receivers.

5.4 MFR based on CCA with Quadratic Rotation

5.4.1 Introduction

In Section 5.2, we have shown the first demonstration of using image processing techniques to recognize modulation formats, and the detailed characterization of the key parameters has been performed in Section 5.3 to optimize the algorithm's performance. Of course, there is still room for the performance promotion. In this section, we show that, by taking the advantage of the symmetry of constellations in the converted binary graph, significant improvement can be achieved in the recognition performance. A simple and effective algorithm using quadratic rotation and addition is applied to the obtained binary image, resulting in less symbols required for the successful recognition, and improved OSNR sensitivity.

5.4.2 Principles

In principle, the parameter which is most relevant to the OSNR sensitivity, is the threshold *Th* in the density filter. It is intuitive that increasing *Th* results in increasing the OSNR sensitivity, as it removes more data samples which are corrupted by the noise. Fig. 5.13(b) shows the converted binary graph from a set of PM-8PSK signal (SNR =12 dB) with the threshold equal to 0.65 in the density filter. As the noise level is high, all the subsets in the converted binary graph mix together and CCA could not figure out the correct number of subsets. However, simply increasing *Th* leads to less survived points after the density filtering, which probably makes the subsequent CCA algorithm fail. In Fig. 5.13(c), the threshold in the density filter is set to be 0.8. It can be seen that even though the subsets can be distinguished now, there are two subsets missing, such that the output of CCA is still not correct. Fortunately, we can take advantage of the symmetry property of the patterns of these modulation formats in the binary graph and use simple logic AND operation between the original binary graph and the rotated graph to make up for the missing subsets, as shown in Fig. 5.13(d). It is worth noting that the logic AND is employed in the binary graph, which is quite computation-efficient in the DSP circuit. The additional logic operations are nearly negligible compared with the processing of complex numbers in other parts of the algorithm. Here, we name the modified CCA-based algorithm as CCA-QR, in which QR is the short form for quadruple rotation, as in

$$I = I \,\&\, rot_{\pi/2}(I) \,\&\, rot_{\pi}(I) \,\&\, rot_{-\pi/2}(I) \tag{5.2}$$

where I is the 0-1 matrix of the binary graph, *&* is the AND operation, and rot_θ is the function that rotates the matrix by an angle of θ. Fig. 5.13(d) shows the binary image after the QR process of Fig. 5.13(c). The output of CCA is correct now for recognition.

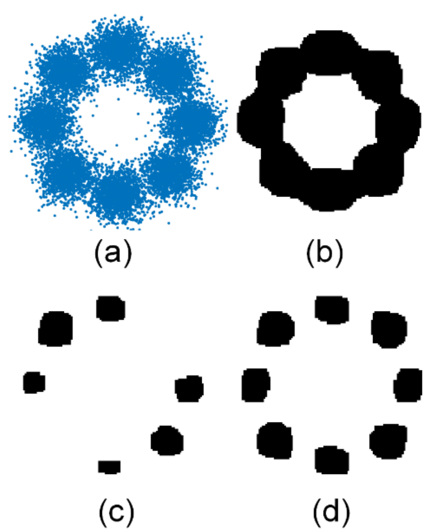

Fig. 5.13 (a) Constellation of 8PSK signal, SNR = 12; (b) Converted binary image, Th = 0.65; (c) Converted binary image, Th = 0.8; (d) Converted binary image, Th = 0.8, with quadruple rotation;

5.4.3 Simulations and results

We have performed numerical simulations for the proposed MFR scheme. 32-Gbaud PM-QPSK, PM-8QAM, PM-8PSK and PM-16QAM signal were generated and passed through a channel with additive Gaussian white noise. The converted binary image had a size of 100*100 pixels (N = 100). The threshold for the Voronoi filtering was set to be 0.65 and 0.8, respectively, corresponding to our previous CCA-based method and the newly proposed CCA-QR method. First, the OSNR value was varied from 10 dB to 26 dB, with a step of 0.2 dB, each having 500 independent implementations. The correct recognition rate was then calculated.

Fig. 5.14 and Fig. 5.15 show the correct recognition rate under different OSNR values, and different number of points involved in the MFR. The OSNR, in the latter case, was set to be 15 dB, 18 dB, 22 dB, and 24 dB for QPSK, 8QAM, 8PSK and 16QAM, respectively. The increase of OSNR sensitivity was clearly seen in Fig. 5.14, i.e., ~1 dB for QPSK, 8PSK and 8QAM, and ~2 dB for 16QAM. Meanwhile, for each tested modulation formats, the number of required points for successful recognition of the modulation formats was reduced significantly, as depicted in Fig. 5.15. The 16QAM case showed the most significant improvement, in which only about half of the points (5000) were needed to reach a successful rate of 95%, compared with the previous scheme (~10000).

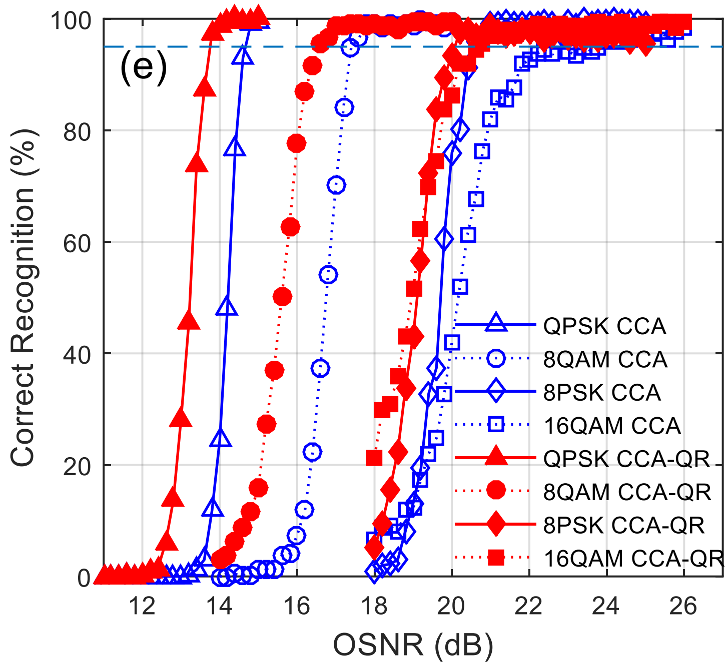

Fig. 5.14 Simulation results of the correct recognition rate under different OSNR values.

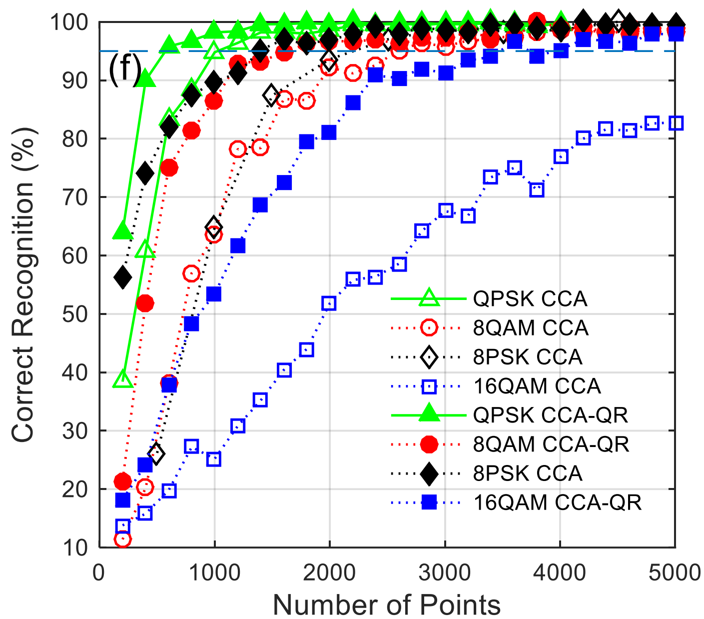

Fig. 5.15 Simulation results of the correct recognition rate under different number of points.

5.4.4 Experiments and results

The experimental setup and configurations were the same as those in [117]. 32-Gbaud polarization-multiplexed QPSK and 16QAM signals were transmitted in a general coherent optical communication testbed. Fig. 5.16(a) shows the experimental setup and the major DSP processes. CCA-based and CCA-QR-based MFR methods were employed to recognize the modulation formats of the received signal, with the threshold Th = 0.65 and 0.8, respectively. Fig. 5.16(b) shows the back-to-back bit error rate (BER) performance. The orange and yellow color blocks represent the successful recognition range of the CCA and CCA-QR based MFR method. The OSNR sensitivity was increased by 1.2 dB and 4.3 dB for QPSK and 16QAM, respectively. Fig. 3(c)-(n) show the converted binary graphs of the CCA and CCA-QR based method. The performance improvement of CCA-QR was significant, as shown in Fig. 5.16(c) & (i), and (f) & (l).

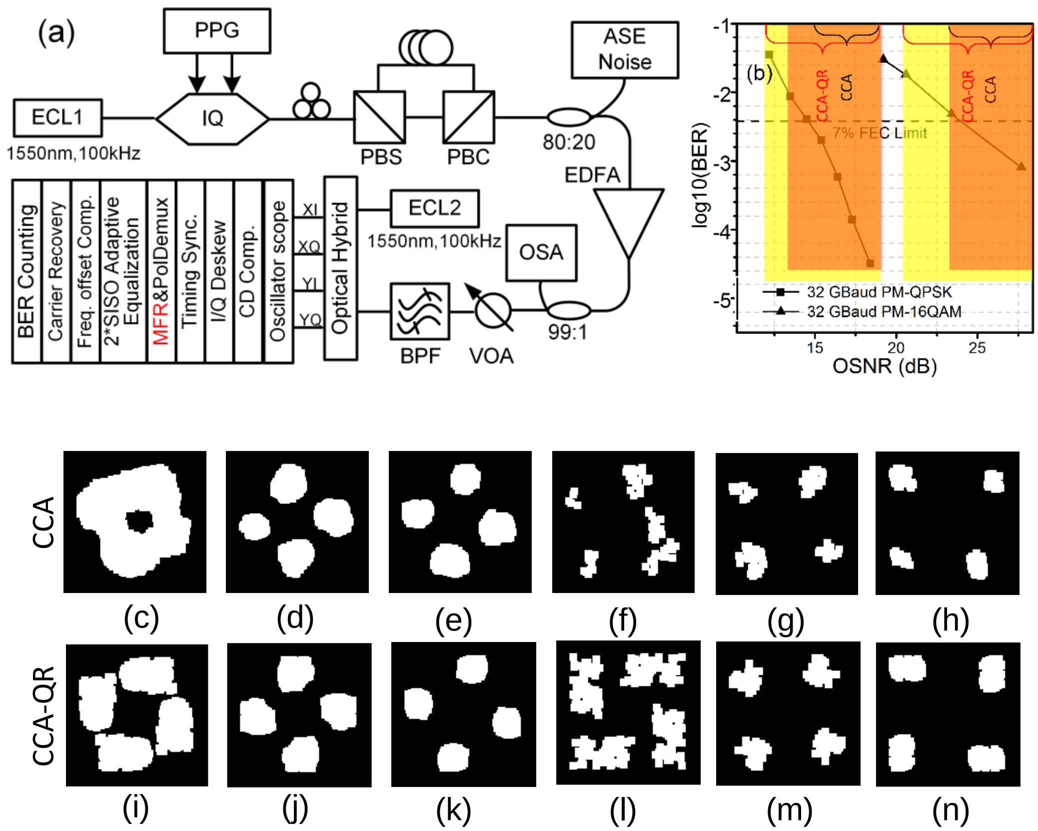

Fig. 5.16 (a) Experimental setup; (b) back-to-back BER result; (c)-(e) converted binary graph of QPSK signals using CCA, OSNR = 12.2 dB, 13.5 dB, and 14.5 dB, respectively; (f)-(h) converted binary graph of 16QAM signals using CCA, OSNR = 20.6 dB, 23.4 dB and 27.7 dB, respectively; (i)-(n): the corresponding CCA-QR results.

5.4.5 Conclusion

In this section, we have proposed a modified modulation format recognition method based on image processing techniques. It shows that, via both numerical simulations and experiments, about 1~3 dB OSNR sensitivity is improved, for coherent polarization multiplexed PSK and QAM signals, with slightly additional simple logic operations.

5.5 MFR in optical OFDM

5.5.1 Introduction

Flexibility is one of the advantages of optical OFDM system than the single-carrier transmission system. The modulation formats in OFDM subcarriers could be adaptively modified according to the data rate requirement, the allocated bandwidth limitation, and the OSNR budget of the link. Adaptive power and bit loading are two useful techniques to make full use of the channel capacity and assure the quality of service for each subcarrier. If we regard each subcarrier of optical OFDM system as a separate channel, it also requires blind modulation format recognition at the receiver, in some cases.

Fortunately, as optical OFDM system maintains the orthogonality between its subcarriers and it benefits from simple channel equalization and phase noise compensation techniques, the MFR in optical OFDM system is much simpler than that in single-carrier coherent system. The simplicity lies on a) the channel response has been compensated via the previous channel estimation; b) the phase noise has been compensated in the previous phase noise compensation; c) there is no need for the Stokes space conversion; d) the recognition is performed just before the decision, so several mature recognition methods which are used in wireless communication can be utilized in the identification.

In this section, we are going to show the feasibility of our proposed CCA-based MFR algorithm, by several simple numerical simulations.

5.5.2 Simulations and results

In the simulation, we used the same setup as in Fig. 5.9, except that the data loaded are OFDM signals. The FFT size was 256, in which 96 subcarriers with lower frequency were modulated with 16QAM signal while higher frequency were modulated with QPSK signal. In this way, we were emulating different modulation formats utilized (or bit loading) in optical OFDM enabled SDN. The laser linewidth was 100 kHz for both laser at the transmitter and laser located at the receiver. The sampling rate was 10 GSamples/s, resulting in a raw data rate of 22.5 Gbps.

The modulation format recognition was performed after the common phase estimation, and we firstly investigated the successful recognition rate (SRR) versus the error vector magnitude (EVM). The EVM here was calculated by

$$EVM = \sqrt{\frac{M}{N}\frac{\sum_{i=0}^{N}\left|x_i^{'} - x_i\right|^2}{\sum_{i=0}^{M}\left|m_i\right|^2}} \tag{5.3}$$

where *N* is the total number of received symbol, *M* is the order of QAM signal, *x* is the reference symbol, *m* is the ideal constellation point and *x'* is the received symbol.

The reason why we use EVM here was that we could not distinguish the ICI induced EVM degradation as mentioned in the previous section from the ASE noise induced EVM degradation, as we only compensated CPE in the receiver DSP process. Therefore, using EVM was a more accurate and fairer choice.

The simulation parameters are listed in Table 5.2.

Table 5.2 Simulation parameters

Parameter	Value
Grid Size	100
Threshold of Density filter	0.4
Size of Averaging filter	7
Number of points	2500

First, we investigated the SRR versus EVM for both QPSK and 16QAM signals. Fig. 5.17 shows the simulation result. We can see that the QPSK had a much larger EVM tolerance than that of 16QAM. The required number of points was also investigated, which is shown in Fig. 5.18. It took about 1000 and 2000 symbols to achieve near to 100% successful recognition rate for QPSK and 16QAM, respectively. It is worth noting that the required number was much smaller than those in single-carrier systems, for both of the two modulation formats.

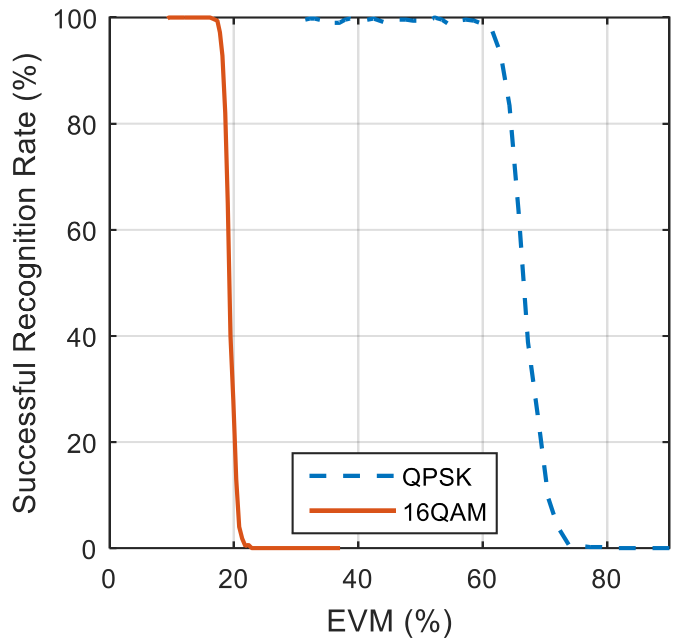

Fig. 5.17 Successful recognition rate under different EVM, for QPSK- and 16QAM-OFDM.

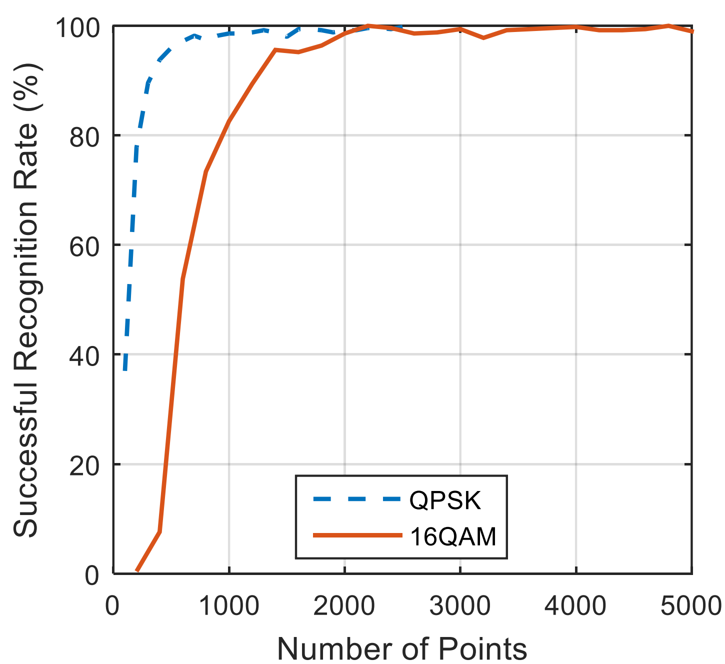

Fig. 5.18 Successful recognition rate versus number of points for QPSK- and 16QAM-OFDM respectively.

5.5.3 Conclusions

In this section, we have shown the feasibility of using our previous proposed CCA-based MFR algorithm to recognize QPSK and 16QAM in optical OFDM systems. The EVM sensitivity and number of points have been investigated via numerical simulations.

5.6 Summary

In this chapter, we have investigated the modulation format recognition in both single-carrier and optical OFDM system. A blind modulation format recognition algorithm based on image processing techniques has been proposed and well optimized. Moreover, a modified algorithm is proposed, and shows significant increase in the recognition sensitivity and reduced resource requirement. Finally, we discussed the feasibility of using the proposed CCA-based modulation format recognition method in the optical OFDM systems.

Chapters 6 Summary

6.1 Summary of this thesis

In this thesis, we have proposed several novel digital signal processing techniques for the OFDM-enabled optical networks. At the intermediate nodes, a low-cost and robust PMD monitoring scheme has been demonstrated and evaluated. At the receiver side, a series of algorithms for laser phase noise estimation and compensation have been proposed, with the tool of bounding box. To support intellective and autonomous detection, a blind modulation format recognition algorithm has been proposed and optimized. With all these work, we aim at ubiquitous and economical optical performance monitoring for the OFDM-enabled flexible optical networks.

In Chapter 1, we have talked about the background of optical OFDM systems. Started from the history and development, we introduce the basis and its significance in the software-defined optical network. Next, an overview of the optical performance monitoring is given, including the transmission impairments and common OPM techniques. In particular, we discuss the OPM in optical OFDM systems. We also review the research challenges in the optical OFDM-enabled SDN, for new requirement for OPM and new parameters to monitor. Finally, we summarize the contributions of this thesis.

In Chapter 2, the background of the research work involved in this thesis is presented. We have reviewed the fundamental basis of PMD and the laser phase noise, along with their monitoring and mitigation methods in fiber-optic communication systems. Previous schemes for modulation format recognition have been reviewed, as well. Moreover, we introduce several essential concepts such as bounding box, convex hull, and Voronoi diagrams in this chapter, which are the roots of our proposal of image processing techniques based algorithms for laser phase noise compensation and modulation format recognition.

In Chapter 3, we have proposed a novel code-correlated PMD monitoring scheme for the DDO-OFDM systems. The principle of the novel code-correlated power estimation as well as the pilot-aided PMD monitoring scheme are introduced first. Experimental demonstration has been shown in both VSB and pure SSB DDO-OFDM system, proving the feasibility and robustness of the code-correlated scheme. Besides, we have further decreased the cost of this PMD monitoring module by demonstrating the feasibility of using a photodiode with bandwidth much smaller than the optical OFDM signal. A new three-code design to improve the robustness of the proposed PMD monitoring scheme to the state of polarization of the optical signal has been proposed as well.

In Chapter 4, we study the laser phase noise effects on CO-OFDM signal and the corresponding estimation and compensation methods. We have proposed a set of algorithms, based on the bounding box of the constellation diagram, to compensate the common phase error. The innovation lies on the fact that it is the first approach, to use image processing technique to solve the problems in optical communication systems. We exhibit the performance of the proposed algorithms in this chapter, by a series of well-designed experiments and numerical simulations, In addition to the CPE, we also show the scheme that uses digital equalizers to compensate the ICI between adjacent subcarriers in CO-OFDM systems.

In Chapter 5, we investigate modulation format recognition at the general coherent receivers. Several schemes have been reviewed and their performance is compared. Afterward, we show our blind and phase-noise-insensitive MFR algorithm, which takes the advantage of simplicity in binary image processing. Extensive numerical simulations have been performed to investigate the OSNR sensitivity, the required number of points for successful recognition, and the optimization of key parameters in the algorithm. An improved algorithm based on quadratic rotation technique has also been demonstrated in this chapter.

6.2 Future work

In Chapter 3, we have proposed a low-cost PMD monitoring scheme for the DDO-OFDM systems. To further enrich the utility of the PMD monitoring scheme in the OFDM-enabled optical networks, the feasibility of the proposed scheme for coherent optical OFDM should be investigated in the future. In such case, a monitoring module consisting of a single-end photodetector is inserted in the coherent optical OFDM system to monitor the PMD value. The research challenge is the direct-detection of a coherent optical signal.

On the other hand, the code-correlated power estimation method should not be limited to the PMD monitoring, but also can be applied to monitor other fiber impairments, as long as the power of the frequency components can be used for monitoring. Chromatic dispersion [119] and OSNR [120] monitoring in OFDM system have been demonstrated by the same code-correlation method by our group. However, how to distinguish each impairment in the simultaneous monitoring is worth to investigate. Meanwhile, how to calibrate the monitoring results of certain parameter according to the accurate monitoring of another parameter is important to investigate.

Finally, it is meaningful to implement these monitoring techniques using low-cost digital signal processors to build up prototypes for the future deployment.

In Chapter 4, we have shown the potential of using image processing techniques in digital signal processing in optical communication system. The next step is to speed up the processing by using more efficient algorithm, or reducing the complexity of the currently proposed scheme. BBB has been proved to be more computation efficient than MBB method, but it requires extensive computation of the convex hull. We can investigate the possible methods to reduce the complexity of calculation the convex hull. Specialized hardware structure is a promising approach, as what the researchers and engineers have done in computer vision. Because the key technique in the algorithm, convex hull calculation, can be more efficiently implemented using parallel processors like graphic processing unit (GPU).

After our first proposal of using bounding box to simplify the estimation of common phase error, this work has been soon followed by other researchers to perform the channel equalization in optical OFDM systems [121], which shows the potential of image processing techniques in the digital signal processing. In the future work, we plan to find more applications for the techniques used in MBB and BBB algorithm. A meaningful but challenging topic is the carrier phase recovery in the coherent single-carrier optical transmission systems. The laser phase noise varies slowly compared with the higher symbol rate, which is the theoretical fundamental of block processing. Inside such data block, our bounding-box-based algorithm is expected to efficiently estimate the laser phase noise.

In Chapter 5, we have succeeded in using the converted image to represent received data signal and using image analysis techniques to recognize the modulation formats. It is just an initial approach in this area. Although we have characterized and optimized several key parameters in the algorithm, it still has much potential in the performance promotion. The fundamental limit and performance boundary of the image processing based algorithms are indispensable for investigation, so that we are able to push the performance close to its limit at the lowest computation complexity.

In the meantime, the most time-consuming computation in the current implementation is the density estimation. It is of great importance to investigate the methods to speed up this process. Even low-cost general graphic process unit (GPU) can be involved in the image processing algorithms' implementation.

It is the first time data are converted to an image for processing. We believe by reviewing the current DSP algorithms, there are potential parts that can be simplified by image processing technique. The efforts in the next phase will be made in finding more applications.

References

[1] J. Armstrong and A. J. Lowery, "Power efficient optical OFDM," *Electronics Letters,* vol. 42, p. 370, March 2006.

[2] W. Shieh and C. Athaudage, "Coherent optical orthogonal frequency division multiplexing," *Electronics Letters*, vol. 42, p. 587, 2006.

[3] W. Shieh, W. Chen, and R. Tucker, "Polarisation mode dispersion mitigation in coherent optical orthogonal frequency division multiplexed systems," *Electronics Letters*, vol. 42, p. 1, 2006.

[4] W. Shieh, "OFDM for Flexible High-Speed Optical Networks," *Journal of Lightwave Technology*, vol. 29, pp. 1560-1577, 2011/05/15 2011.

[5] R. W. Chang, *Orthogonal Frequency Multplex Data Transmission System,* 1970.

[6] L. Cimini, "Analysis and Simulation of a Digital Mobile Channel Using Orthogonal Frequency Division Multiplexing," *IEEE Transactions on Communications*, vol. 33, pp. 665-675, 1985.

[7] Y. Tanaka, T. Komine, S. Haruyama, and M. Nakagawa, "Indoor visible communication utilizing plural white LEDs as lighting," in *Personal, Indoor and Mobile Radio Communications, 2001 12th IEEE International Symposium on*, 2001, pp. F-81-F-85 vol.2.

[8] A. James Lowery and J. Armstrong, "10 Gbit/s multimode fiber link using power-efficient orthogonal-frequency-division multiplexing," *Optics Express*, vol. 13, pp. 10003-10009, 2005/12/12 2005.

[9] A. Li, X. Chen, G. Gao, and W. Shieh, "Transmission of 1 Tb/s Unique-Word DFT-Spread OFDM Superchannel Over 8000 km EDFA-Only SSMF Link," *Journal of Lightwave Technology*, vol. 30, pp. 3931-3937, 2012.

[10] T. Omiya, M. Yoshida, and M. Nakazawa, "400 Gbit/s 256 QAM-OFDM Transmission over 720 km with a 14 bit/s/Hz Spectral Efficiency Using an Improved FDE Technique," in *Optical Fiber Communication Conference/National Fiber Optic Engineers Conference 2013*, Anaheim, California, 2013, p. OTh4E.1.

[11] C. H. Yeh, C. W. Chow, J. Y. Sung, and Y. F. Wu, "Use of RSOA-transmitter for OFDM colorless WDM-PON communication," *Optical and Quantum Electronics*, vol. 48, pp. 1-10, 2016.

[12] P. Dong, J. Lee, Y.-K. Chen, L. L. Buhl, S. Chandrasekhar, J. H. Sinsky, *et al.*, "Four-Channel 100-Gb/s per Channel Discrete Multi-Tone Modulation Using Silicon Photonic Integrated Circuits," in *Optical Fiber Communication Conference Post Deadline Papers*, Los Angeles, California, 2015, p. Th5B.4.

[13] J. Armstrong, "OFDM for optical communications," *Journal of Lightwave Technology*, vol. 27, p. 189, 2009.

[14] W. Shieh, H. Bao, and Y. Tang, "Coherent optical OFDM: theory and design," *Optics Express*, vol. 16, pp. 841-859, 2008/01/21 2008.

[15] M. Jinno, H. Takara, B. Kozicki, Y. Tsukishima, Y. Sone, and S. Matsuoka, "Spectrum-efficient and scalable elastic optical path network: architecture, benefits, and enabling technologies," *IEEE Communications Magazine*, vol. 47, pp. 66-73, 2009.

[16] W. Shieh, "OFDM for Flexible High-Speed Optical Networks," *J.Lightwave Technol.*, vol. 29, p. 1560, May 2011.

[17] C. C.-K. Chan, *Optical performance monitoring: advanced techniques for next-generation photonic networks*: Academic Press, 2010.

[18] "ANSI/TIA Standard," in *ANSI/TIA/EIA-536-19-200*, ed, 2000.

[19] C. R. Doerr and H. Kim, "Monitoring alignment between pulse carvers and phase modulators in optical systems," ed: Google Patents, 2005.

[20] J. Hansryd, P. A. Andrekson, and B. Bakhshi, "Prescaled Clock Recovery Based on Small Timing Misalignment of Data Pulses," *Journal of Lightwave Technology*, vol. 19, p. 105, 2001/01/01 2001.

[21] D. C. Kilper, R. Bach, D. J. Blumenthal, D. Einstein, T. Landolsi, L. Ostar, *et al.*, "Optical Performance Monitoring," *Journal of Lightwave Technology*, vol. 22, p. 294, 2004/01/01 2004.

[22] L. Zhihong and L. Guifang, "Chromatic dispersion and polarization-mode dispersion monitoring for RZ-DPSK signals based on asynchronous amplitude-histogram evaluation," *Journal of Lightwave Technology*, vol. 24, pp. 2859-2866, 2006.

[23] T. B. Anderson, A. Kowalczyk, K. Clarke, S. D. Dods, D. Hewitt, and J. C. Li, "Multi Impairment Monitoring for Optical Networks," *Journal of Lightwave Technology*, vol. 27, pp. 3729-3736, 2009.

[24] K. Jong, H. Tsao, and S. Lee, "Q-factor monitoring of optical signal-to-noise ratio degradation in optical DPSK transmission," *Electronics Letters*, vol. 5, 2008.

[25] C. Dorrer, D. C. Kilper, H. R. Stuart, G. Raybon, and M. G. Raymer, "Linear optical sampling," *IEEE Photonics Technology Letters*, vol. 15, pp. 1746-1748, 2003.

[26] T. Luo, Z. Pan, S. M. R. Motaghian Nezam, L. S. Yan, A. B. Sahin, and A. E. Willner, "PMD monitoring by tracking the chromatic-dispersion-insensitive RF power of the vestigial sideband," *Photonics Technology Letters, IEEE*, vol. 16, p. 2177, Sept 2004.

[27] S. M. R. M. Nezam, S. Yong-Won, Y. Changyuan, J. E. McGeehan, A. B. Sahin, and A. E. Willner, "First-order PMD monitoring for NRZ data using RF clock regeneration techniques," *Lightwave Technology, Journal of,* vol. 22, p. 1086, April 2004.

[28] M. N. Petersen, Z. Pan, S. Lee, S. A. Havstad, and A. E. Willner, "Online chromatic dispersion monitoring and compensation using a single inband subcarrier tone," *IEEE Photonics Technology Letters,* vol. 14, pp. 570-572, 2002.

[29] G.-W. Lu, M.-H. Cheung, L.-K. Chen, and C.-K. Chan, "Simultaneous PMD and OSNR monitoring by enhanced RF spectral dip analysis assisted with a local large-DGD element," *Photonics Technology Letters, IEEE,* vol. 17, p. 2790, Dec 2005.

[30] J. H. Lee, H. Y. Choi, S. K. Shin, and Y. C. Chung, "A Review of the Polarization-Nulling Technique for Monitoring Optical-Signal-to-Noise Ratio in Dynamic WDM Networks," *Journal of Lightwave Technology,* vol. 24, pp. 4162-4171, 2006.

[31] S. M. R. M. Nezam, L. S. Yan, Y. Q. Shi, A. E. Willner, and S. Yao, "Wide-dynamic-range DGD monitoring by partial optical signal spectrum DOP measurement," in *Optical Fiber Communication Conference and Exhibit, 2002. OFC 2002,* 2002, pp. FD8-1-FD8-3.

[32] S. M. R. M. Nezam, J. E. McGeehan, and A. E. Willner, "Degree-of-polarization-based PMD monitoring for subcarrier-multiplexed signals via equalized carrier/sideband filtering," *Journal of Lightwave Technology,* vol. 22, pp. 1078-1085, 2004.

[33] W. Xiaoxia, J. Jargon, and A. E. Willner, "Off-line monitoring of OSNR/CD/PMD degradation effects using neural-network-based training sequences," in *2008 34th European Conference on Optical Communication,* 2008, pp. 1-2.

[34] T. S. R. Shen, K. Meng, A. P. T. Lau, and Z. Y. Dong, "Optical Performance Monitoring Using Artificial Neural Network Trained With Asynchronous Amplitude Histograms," *IEEE Photonics Technology Letters*, vol. 22, pp. 1665-1667, 2010.

[35] J. A. Jargon, X. Wu, and A. E. Willner, "Optical Performance Monitoring by Use of Artificial Neural Networks Trained with Parameters Derived from Delay-Tap Asynchronous Sampling," in *Optical Fiber Communication Conference and National Fiber Optic Engineers Conference*, San Diego, California, 2009, p. OThH1.

[36] S. J. Savory, "Digital Coherent Optical Receivers: Algorithms and Subsystems," *IEEE Journal of Selected Topics in Quantum Electronics*, vol. 16, pp. 1164-1179, Sep-Oct 2010.

[37] J. C. Geyer, C. R. Fludger, T. Duthel, C. Schulien, and B. Schmauss, "Performance Monitoring Using Coherent Receivers," in *Optical Fiber Communication Conference and National Fiber Optic Engineers Conference*, San Diego, California, 2009, p. OThH5.

[38] Y.-C. Ku, C.-K. Chan, and L.-K. Chen, "A Novel Robust OSNR Monitoring Technique with 40-dB Dynamic Range Using Phase Modulator Embedded Fiber Loop Mirror," in *Optical Fiber Communication Conference and Exposition and The National Fiber Optic Engineers Conference*, Anaheim, California, 2006, p. OWN6.

[39] X. Liu, Y. H. Kao, S. Chandrasekhar, I. Kang, S. Cabot, and L. L. Buhl, "OSNR Monitoring Method for OOK and DPSK Based on Optical Delay Interferometer," *IEEE Photonics Technology Letters*, vol. 19, pp. 1172-1174, 2007.

[40] W. Shieh, R. S. Tucker, W. Chen, X. Yi, and G. Pendock, "Optical performance monitoring in coherent optical OFDM systems," *Optics Express*, vol. 15, pp. 350-356, 2007/01/22 2007.

[41] X. Yi, W. Shieh, Y. Ma, Y. Tang, and G. J. Pendock, "Experimental Demonstration of Optical Performance Monitoring in Coherent Optical OFDM Systems," in *Optical Fiber Communication Conference/National Fiber Optic Engineers Conference*, 2008, p. OThW3.

[42] S. Chen, T. Anderson, D. Hewitt, A. V. Tran, C. Zhu, L. B. Du, *et al.*, "Optical performance monitoring for OFDM using low bandwidth coherent receivers," *Opt Express,* vol. 20, pp. 28724-33, Dec 17 2012.

[43] C. C. Do, A. V. Tran, S. Chen, T. Anderson, D. Hewitt, and E. Skafidas, "Flexible bandwidth DGD estimation for coherent optical OFDM system," *Opt.Express,* vol. 21, p. 25788, Nov 2013.

[44] X. Chen, A. A. Amin, and W. Shieh, "Characterization and Monitoring of Laser Linewidths in Coherent Systems," *Journal of Lightwave Technology,* vol. 29, pp. 2533-2537, 2011.

[45] L. E. Nelson and R. M. Jopson, "Introduction to polarization mode dispersion in optical systems," in *Polarization Mode Dispersion*, ed: Springer, 2005, p. 1.

[46] C. D. Poole and R. E. Wagner, "Phenomenological approach to polarisation dispersion in long single-mode fibres," *Electronics Letters,* vol. 22, p. 1029, 1986.

[47] C. D. Poole, N. S. Bergano, R. E. Wagner, and H. J. Schulte, "Polarization dispersion and principal states in a 147-km undersea lightwave cable," *Journal of Lightwave Technology ,* vol. 6, p. 1185, 1988.

[48] C. Francia, F. Bruyere, D. Penninckx, and M. Chbat, "PMD second-order effects on pulse propagation in single-mode optical fibers," *Photonics Technology Letters, IEEE,* vol. 10, p. 1739, 1998.

[49] N. Cvijetic, S. G. Wilson, and D. Qian, "System Outage Probability Due to PMD in High-Speed Optical OFDM Transmission," *J.Lightwave Technol.,* vol. 26, p. 2118, Jul 2008.

[50] C. D. Poole, R. W. Tkach, A. R. Chraplyvy, and D. A. Fishman, "Fading in lightwave systems due to polarization-mode dispersion," *Photonics Technology Letters, IEEE,* vol. 3, p. 68, Jan 1991.

[51] W. Shieh and I. Djordjevic, *OFDM for optical communications*: Academic Press, 2009.

[52] F. Roy, C. Francia, F. Bruyere, and D. Penninckx, "A simple dynamic polarization mode dispersion compensator," in *Optical Fiber Communication Conference, 1999, and the International Conference on Integrated Optics and Optical Fiber Communication. OFC/IOOC '99. Technical Digest*, 1999, pp. 275-278 vol.1.

[53] F. N. Khan, T. S. R. Shen, Y. Zhou, A. P. T. Lau, and C. Lu, "Optical Performance Monitoring Using Artificial Neural Networks Trained With Empirical Moments of Asynchronously Sampled Signal Amplitudes," *IEEE Photonics Technology Letters,* vol. 24, pp. 982-984, 2012.

[54] W. Shieh, "PMD-Supported Coherent Optical OFDM Systems," *IEEE Photonics Technology Letters,* vol. 19, pp. 134-136, 2007.

[55] B. J. C. Schmidt, A. J. Lowery, and J. Armstrong, "Impact of PMD in Single-Receiver and Polarization-Diverse Direct-Detection Optical OFDM," *J.Lightwave Technol.,* vol. 27, p. 2792, Jul 2009.

[56] W. Songping and Y. Bar-Ness, "OFDM systems in the presence of phase noise: consequences and solutions," *IEEE Transactions on Communications,* vol. 52, pp. 1988-1996, 2004.

[57] T. Pfau, S. Hoffmann, and R. Noe, "Hardware-Efficient Coherent Digital Receiver Concept With Feedforward Carrier Recovery for M-QAM Constellations," *Journal of Lightwave Technology,* vol. 27, pp. 989-999, 2009.

[58] A. G. Armada and M. Calvo, "Phase Noise and Sub-Carrier Spacing Effects on the Performance of an OFDM Communication System," *IEEE Communications Letters,* vol. 2, pp. 11-13, Jan 1998.

[59] X. Yi, W. Shieh, and Y. Tang, "Phase Estimation for Coherent Optical OFDM," *IEEE Photonics Technology Letters,* vol. 19, pp. 919-921, 2007.

[60] A. Viterbi, "Nonlinear estimation of PSK-modulated carrier phase with application to burst digital transmission," *Information Theory, IEEE Transactions on,* vol. 29, pp. 543-551, 1983.

[61] S. L. Jansen, I. Morita, T. C. W. Schenk, N. Takeda, and H. Tanaka, "Coherent Optical 25.8-Gb/s OFDM Transmission Over 4160-km SSMF," *Journal of Lightwave Technology,* vol. 26, pp. 6-15, 2008/01/01 2008.

[62] Z. Liu, J.-Y. Kim, D. S. Wu, D. J. Richardson, and R. Slavik, "Homodyne OFDM with Optical Injection Locking for Carrier Recovery," *Journal of Lightwave Technology,* vol. 33, pp. 34-41, 2015.

[63] T. K. S. T. Le*, M. E. McCarthy, E. Giacoumidis, I.D. Phillips, M. F. C. Stephens, M. Tan, N. J. Doran, and A. D. E. a. S. K. Turitsyn, "Demonstration of Data-dependent Pilot Aided Phase Noise Estimation for CO-OFDM," in *Optical Fiber Communication Conference (OFC),* San Francisco, CA, USA, 2014.

[64] S. T. Le, M. E. McCarthy, N. M. Suibhne, M. A. Z. Al-Khateeb, E. Giacoumidis, N. Doran, *et al.*, "Demonstration of Phase-Conjugated Subcarrier Coding for Fiber Nonlinearity Compensation in CO-OFDM Transmission," *Journal of Lightwave Technology,* vol. 33, pp. 2206-2212, 2015/06/01 2015.

[65] X. Zhang, J. Li, C. Li, M. Luo, H. Li, Z. He, *et al.*, "Pilot-based blind phase estimation for coherent optical OFDM system," *Opt Express*, vol. 22, pp. 22888-94, Sep 22 2014.

[66] M.-K. Lee, S.-C. Lim, and K. Yang, "Blind Compensation for Phase Noise in OFDM Systems over Constant Modulus Modulation," *IEEE Transactions on Communications,* vol. 60, pp. 620-625, 2012.

[67] Y. Ha and W. Chung, "Non-Data-Aided Phase Noise Suppression Scheme for CO-OFDM Systems," *IEEE Photonics Technology Letters,* vol. 25, pp. 1703-1706, 2013.

[68] X. Yi, X. Chen, D. Sharma, C. Li, M. Luo, Q. Yang, *et al.*, "Digital coherent superposition of optical OFDM subcarrier pairs with Hermitian symmetry for phase noise mitigation," *Opt Express,* vol. 22, pp. 13454-9, Jun 2 2014.

[69] X. Hong, X. Hong, and S. He, "Linearly interpolated sub-symbol optical phase noise suppression in CO-OFDM system," *Optics Express,* vol. 23, pp. 4691-4702, 2015/02/23 2015.

[70] W. Chung, "A Matched Filtering Approach for Phase Noise Suppression in CO-OFDM Systems," *IEEE Photonics Technology Letters,* vol. 22, pp. 1802-1804, 2010.

[71] C. Yang, C. He, and Z. Wang, "Iterative phase noise estimation and suppression for CO-OFDM systems with large laser linewidth," in *Communications and Photonics Conference and Exhibition, 2011. ACP. Asia*, 2011, pp. 1-6.

[72] C. Yang, F. Yang, and Z. Wang, "Orthogonal Basis Expansion-Based Phase Noise Estimation and Suppression for CO-OFDM Systems," *IEEE Photonics Technology Letters,* vol. 22, pp. 51-53, 2010.

[73] C. Yang, F. Yang, and Z. Wang, "Phase noise suppression for coherent optical block transmission systems: a unified framework," *Optics Express,* vol. 19, pp. 17013-17020, 2011/08/29 2011.

[74] G. Toussaint, "Solving geometric problems with the rotating calipers," in *IEEE MELECON*, Athens, Greece,, 1983.

[75] H. Freeman and R. Shapira, "Determining the minimum-area encasing rectangle for an arbitrary closed curve," *Commun. ACM,* vol. 18, pp. 409-413, 1975.

[76] R. L. Graham, "An Efficient Algorithm for Determining the Convex Hull of a Finite Planar Set," *Inf. Process. Lett.,* vol. 1, pp. 132-133, 1972.

[77] C. B. Barber, D. P. Dobkin, and H. Huhdanpaa, "The Quickhull algorithm for convex hulls," *Acm Transactions on Mathematical Software,* vol. 22, pp. 469-483, Dec 1996.

[78] T. M. Chan, "Optimal output-sensitive convex hull algorithms in two and three dimensions," *Discrete & Computational Geometry,* vol. 16, pp. 361-368, 1995.

[79] O. A. Dobre, A. Abdi, Y. Bar-Ness, and W. Su, "Survey of automatic modulation classification techniques: classical approaches and new trends," *IET Communications,* vol. 1, pp. 137-156, 2007.

[80] N. G. Gonzalez, D. Zibar, and I. T. Monroy, "Cognitive digital receiver for burst mode phase modulated radio over fiber links," in *Proc. ECOC*, 2010.

[81] J. MacQueen, "Some methods for classification and analysis of multivariate observations," in *Proceedings of the fifth Berkeley symposium on mathematical statistics and probability*, 1967, pp. 281-297.

[82] P. Isautier, A. Stark, K. Mehta, R. de Salvo, and S. E. Ralph, "Autonomous Software-Defined Coherent Optical Receivers," in *Optical Fiber Communication Conference/National Fiber Optic Engineers Conference 2013,* Anaheim, California, 2013, p. OTh3B.4.

[83] E. J. Adles, M. L. Dennis, W. R. Johnson, T. P. McKenna, C. R. Menyuk, J. E. Sluz, *et al.*, "Blind Optical Modulation Format Identification From Physical Layer Characteristics," *Journal of Lightwave Technology,* vol. 32, pp. 1501-1509, 2014/04/15 2014.

[84] F. N. Khan, Y. Zhou, A. P. T. Lau, and C. Lu, "Modulation format identification in heterogeneous fiber-optic networks using artificial neural networks," *Optics express*, vol. 20, pp. 12422-12431, 2012.

[85] J. Liu, Z. Dong, K. Zhong, A. P. T. Lau, C. Lu, and Y. Lu, "Modulation format identification based on received signal power distributions for digital coherent receivers," in *Optical Fiber Communications Conference and Exhibition (OFC), 2014*, 2014, pp. 1-3.

[86] S. M. Bilal, G. Bosco, Z. Dong, A. P. T. Lau, and C. Lu, "Blind modulation format identification for digital coherent receivers," *Optics Express*, vol. 23, pp. 26769-26778, 2015/10/05 2015.

[87] R. Borkowski, D. Zibar, A. Caballero, V. Arlunno, and I. T. Monroy, "Stokes Space-Based Optical Modulation Format Recognition for Digital Coherent Receivers," *IEEE Photonics Technology Letters*, vol. 25, pp. 2129-2132, Nov 1 2013.

[88] R. Boada, R. Borkowski, and I. T. Monroy, "Clustering algorithms for Stokes space modulation format recognition," *Opt Express*, vol. 23, pp. 15521-31, Jun 15 2015.

[89] A. Dempster, N. Laird, and D. Rdin, "Maximum Likelihood from Incomplete Data via the EM Algorithm," in *Journal Of The Royal Statistical Society, Series B*, 1977, pp. 1-38.

[90] M. Ester, H.-p. Kriegel, S. JÃ¶rg, and X. Xu, "A density-based algorithm for discovering clusters in large spatial databases with noise," pp. 226-231, 1996.

[91] M. Ankerst, M. M. Breunig, H.-P. Kriegel, #246, and r. Sander, "OPTICS: ordering points to identify the clustering structure," presented at the Proceedings of the 1999 ACM SIGMOD international conference on Management of data, Philadelphia, Pennsylvania, USA, 1999.

[92] A. Y. Ng, M. I. Jordan, and Y. Weiss, "On spectral clustering: Analysis and an algorithm," *Advances in neural information processing systems*, vol. 2, pp. 849-856, 2002.

[93] D. Derickson, "Fiber optic test and measurement," in *Fiber optic test and measurement/edited by Dennis Derickson. Upper Saddle River, NJ: Prentice Hall, c1998.*, 1998.

[94] B. Szafraniec, B. Nebendahl, and T. Marshall, "Polarization demultiplexing in Stokes space," *Optics Express*, vol. 18, pp. 17928-17939, 2010/08/16 2010.

[95] S. Fortune, "A sweepline algorithm for Voronoi diagrams," *Algorithmica*, vol. 2, pp. 153-174.

[96] *Voronoi diagram*. Available: https://en.wikipedia.org/wiki/Voronoi_diagram

[97] W. R. Peng, "Direct Detection Optical OFDM," in *Optical Fiber Communication Conference*, 2014, p. Th3K.7.

[98] L. Zhaohui, X. Xiao, G. Tao, Y. Qi, H. Rong, H. Zhixue, *et al.*, "432-Gb/s Direct-Detection Optical OFDM Superchannel Transmission Over 3040-km SSMF," *IEEE Photonics Technology Letters*, vol. 25, p. 1524, aug 2013.

[99] B. C. Schmidt, A. Lowery, and J. Armstrong, "Experimental Demonstrations of Electronic Dispersion Compensation for Long-Haul Transmission Using Direct-Detection Optical OFDM," *J.Lightwave Technol.*, vol. 26, p. 196, Jan 2008.

[100] M. Mayrock and H. Haunstein, "PMD Tolerant Direct-Detection Optical OFDM System," in *Optical Communication (ECOC), 2007 33rd European Conference and Ehxibition of*, 2007, p. 1.

[101] W.-R. Peng, X. Wu, V. R. Arbab, K.-M. Feng, B. Shamee, L. C. Christen, *et al.*, "Theoretical and Experimental Investigations of Direct-Detected RF-Tone-Assisted Optical OFDM Systems," *J.Lightwave Technol.*, vol. 27, p. 1332, May 2009.

[102] A. E. Willner, S. M. R. M. Nezam, L. Yan, P. Zhongqi, and M. C. Hauer, "Monitoring and control of polarization-related impairments in optical fiber systems," *Journal of Lightwave Technology,* vol. 22, p. 106, Jan 2004.

[103] R. Feced, S. J. Savory, A. Hadjifotiou, J. Jiang, D. Richards, S. Oliva, *et al.*, "Interaction between polarization mode dispersion and polarization-dependent losses in optical communication links; PMD and PDL monitoring of traffic-carrying transatlantic fibre-optic system," *Electronics Letters*, vol. 20; 45, p. 424; 123, Mar; January 2003.

[104] S. Chandrasekhar, L. Xiang, B. Zhu, and D. W. Peckham, "Transmission of a 1.2-Tb/s 24-carrier no-guard-interval coherent OFDM superchannel over 7200-km of ultra-large-area fiber," in *2009 35th European Conference on Optical Communication*, 2009, pp. 1-2.

[105] B. Yuan, L. K. Kwoh, and C. L. Tan, "Finding the Best-Fit Bounding-Boxes," in *Document Analysis Systems VII: 7th International Workshop, DAS 2006, Nelson, New Zealand, February 13-15, 2006. Proceedings*, H. Bunke and A. L. Spitz, Eds., ed Berlin, Heidelberg: Springer Berlin Heidelberg, 2006, pp. 268-279.

[106] M. Sarfraz and Z. Rasheed, "Skew Estimation and Correction of Text Using Bounding Box," pp. 259-264, 2008.

[107] T. Bo, L. Huang, and C.-K. Chan, "Image Processing Based Common Phase Estimation for Coherent Optical Orthogonal Frequency Division Multiplexing System," in *Optical Fiber Communication Conference*, Los Angeles, California, 2015, p. W1E.8.

[108] T. Bo, L. Huang, and C. K. Chan, "Common Phase Estimation in Coherent OFDM System Using Image Processing Technique," *IEEE Photonics Technology Letters,* vol. 27, pp. 1597-1600, 2015.

[109] S. G. Akl and G. T. Toussaint, "A fast convex hull algorithm," *Information Processing Letters*, vol. 7, pp. 219-222, 8// 1978.

[110] L. Devroye and G. T. Toussaint, "A note on linear expected time algorithms for finding convex hulls," *Computing*, vol. 26, pp. 361-366.

[111] R. Atanassov, P. Bose, M. Couture, A. Maheshwari, P. Morin, M. Paquette, *et al.*, "Algorithms for optimal outlier removal," *Journal of Discrete Algorithms*, vol. 7, pp. 239-248, 6// 2009.

[112] T. Pfau, S. Hoffmann, and R. Noe, "Hardware-Efficient Coherent Digital Receiver Concept With Feedforward Carrier Recovery for *M*-QAM Constellations," *Journal of Lightwave Technology*, vol. 27, pp. 989-999, 2009.

[113] M. R. Gholami, S. Nader-Esfahani, and A. A. Eftekhar, "A new method of phase noise compensation in OFDM," in *Communications, 2003. ICC '03. IEEE International Conference on*, 2003, pp. 3443-3446 vol.5.

[114] D. Petrovic, W. Rave, and G. Fettweis, "Phase noise suppression in OFDM including intercarrier interference," in *Proc. Intl. OFDM Workshop (InOWo)*, 2003, pp. 219-224.

[115] Z. Zan and A. J. Lowery, "Experimental demonstration of a flexible and stable semiconductor laser linewidth emulator," *Optics Express*, vol. 18, pp. 13880-13885, 2010/06/21 2010.

[116] D. Che, A. Li, and W. Shieh, "Blind polarization de-multiplexing for stokes vector direct detection," in *Optical Communication (ECOC), 2015 European Conference on*, 2015, pp. 1-3.

[117] T. Bo, J. Tang, and C.-K. Chan, "Blind Modulation Format Recognition for Software-defined Optical Networks Using Image Processing Techniques " in *Optical Fiber Communications Conference and Exhibition (OFC), 2016*, Anaheim, California, USA, 2016, pp. 1-3.

[118] A. AbuBaker, R. Qahwaji, S. Ipson, and M. Saleh, "One Scan Connected Component Labeling Technique," in *Signal Processing and Communications, 2007. ICSPC 2007. IEEE International Conference on*, 2007, pp. 1283-1286.

[119] K.-H. Tse and C.-K. Chan, "Coded-subcarrier-aided chromatic dispersion monitoring scheme for flexible optical OFDM networks," *Optics Express*, vol. 22, p. 18934, 2014.

[120] S. Gao, L. Huang, and C.-K. Chan, "Pilot-Aided Optical Signal-to-Noise Ratio Estimation for Direct-Detection OFDM Systems," *IEEE Photonics Technology Letters*, vol. 27, pp. 1165-1168, 2015.

[121] Z. Yu, Y. Lou, M. Chen, H. Chen, S. Yang, and S. Xie, "Channel Estimation on Individual Subcarrier Using Image Processing in Optical OFDM System," *IEEE Photonics Technology Letters*, vol. 28, pp. 1815-1818, 2016.

Appendix

List of abbreviations

AAH	Asymmetric amplitude histogram
ADSL	Asymmetric digital subscriber line
AF	Averaging filter
ANN	Artificial neural network
ASE	Amplified spontaneous emission
AWG	Arbitrary waveform generator
BER	Bit-error-rate
BPS	Blind phase searching
CCA	Connected component analysis
CD	Chromatic dispersion
CML	Chirp managed laser
CP	Cyclic prefix
CPE	Common phase error
CSI	Channel state information
CW	Continuous-wave
DA	Data aided
DCM	Dispersion compensation module
DF	Decision-feedback
DGD	Differential group delay

DML	Directly modulated semiconductor laser
DOF	Degrees of freedom
DOP	Degree of polarization
DSA	Digital sampling analyzer
DSO	Digital sampling oscilloscope
DSP	Digital signal processing
DWDM	Dense wavelength division multiplexing
ECL	External cavity laser
EDC	Electronic dispersion compensation
EDFA	Erbium doped fiber amplifier
EM	Expectation maximization
FBG	Fiber Bragg grating
FDM	Frequency division multiplexing
FFT	Fast Fourier transform
FWM	Four-wave mixing
ICI	Inter-carrier interference
IDFT	Inverse discrete Fourier transform
IFFT	Inverse fast Fourier transform
IQ	In-phase/quadrature
ISI	Inter symbol interference
LMS	Least-mean-square
LO	Local oscillator
MBB	Minimum bounding box
MCM	Multi-carrier modulation
MFR	Modulation format recognition
NRZ	Non-return-to-zero
OFC	Optical Fiber Communication Conference

OFDM	Orthogonal frequency division multiplexing
OOK	On-off-keying
OPM	Optical performance monitoring
OSA	Optical spectrum analyzer
OSNR	Optical signal-noise-ratio
OTN	Optical transport network
PA	Pilot-aided
PBC	Polarization beam combiner
PBS	Polarization beam splitter
PDL	Polarization dependent loss
PM	Phase modulator
PMD	Polarization mode dispersion
PPG	Programmable pattern generator
PS	Pilot subcarrier
PSD	Power spectral density
PSK	Phase-shift-keying
PSP	Principle state of polarization
QAM	Quadrature amplitude modulated
QoS	Quality of service
QR	Quadruple rotation
RF	Radio frequency
RMSE	Root mean square error
RZ	Return-to-zero
SBS	Stimulated Brillouin scattering
SDOT	Software-defined optical transponder
SDR	Software defined radio
SMF	Single mode fiber

SNR	Signal-to-noise ratio
SOP	State of polarization
SPM	Self-phase modulation
SRS	Stimulated Raman scattering
SSB	Single side band
VOA	Variable optical attenuator
WDM	Wavelength division multiplexing

List of publications

[1] **T. Bo**, S. Gao, K.H. Tse, C.K. Chan "A PMD Monitoring Scheme for Direct-Detection Optical OFDM Systems Using Code-Assisted Optical Subcarriers" *International Conference on Lasers and Electro- Optics, CLEO 2014*, STu3J.4, San Jose, California, USA, 2014.

[2] **T. Bo**, L. Huang, C.K. Chan "Image Processing Based Common Phase Estimation for Coherent Optical Orthogonal Frequency Division Multiplexing System" *IEEE/OSA Optical Fiber Conference (OFC) 2015*, W1E.8, Los Angeles, California, USA, 2015.

[3] **T. Bo**, S. Gao, K.H. Tse, C.K. Chan "A Pilot-correlated PMD Monitoring Scheme for Direct-Detection Optical OFDM Systems" *IEEE OSA Journal of Lightwave Technology*, vol.33 no. 13, pp. 2884–2891, Apr. 2015.

[4] **T. Bo**, L. Huang, C.K. Chan "Common Phase Estimation in Coherent OFDM System Using Image Processing Technique" *IEEE Photonics Technology Letters*, vol. 27, no. 15, pp. 1597–1600, May. 2015.

[5] **T. Bo**, C.K. Chan " Common Phase Error Estimation for Coherent Optical OFDM System Using Best-fit Bounding Box" *Photonics in Switching 2015*, FrIII1–5, Florence, Italy, 2015.

[6] X. Guan, **T. Bo**, C.K. Chan "Mitigation of Inter-Carrier Interference Induced by Phase Noise and Residual Carrier Frequency Offset in CO-OFDM Systems" *Photonics in Switching 2015*, Poster SC3–5, Florence, Italy, 2015.

[7] X. Guan, **<u>T. Bo</u>**, C.K. Chan " Virtual Private Networks in RoF-OFDM-PON with Physical-layer Network Coding" *Photonics in Switching 2015*, ThIII3–3, Florence, Italy, 2015.

[8] **<u>T. Bo</u>**, J. Tang, C.K.Chan "Blind Modulation Format Recognition for Software-defined Optical Networks Using Image Processing Techniques" *IEEE/OSA Optical Fiber Conference (OFC) 2016*, Th2A.31, Anaheim, California, USA, 2016.

[9] G.W. Lu, **<u>T. Bo</u>**, C.K.Chan "Pump-Phase-Noise-Tolerant Wavelength Conversion for Coherent Optical OFDM using Coherent DFB Pumping" *IEEE/OSA Optical Fiber Conference (OFC) 2016*, W3D.3, Anaheim, California, USA, 2016.

[10] G.W. Lu, **<u>T. Bo</u>**, T. Sakamoto, K. Akahane, C.K. Chan,N. Yamamoto "Experimental Investigation of Phase-Sensitive Amplification in Quantum-Dot Semiconductor Optical Amplifier" *International Conference on Lasers and Electro-Optics, CLEO 2016*, accepted, San Jose, California, USA, 2014.

[11] **<u>T. Bo</u>**, J. Tang, C.K.Chan "Enhanced Blind Modulation Formats Recognition using Connected Component Analysis with Quadruple Rotation" *Optoelectronoics and Communications Conference / International Conference on Photonics in Switching 2016*, accepted, Niigata, Japan, 2016.

[12] G.W. Lu, **<u>T. Bo</u>**, T. Sakamoto, N. Yamaoto, C.K. Chan, "Flexible and scalable wavelength multicast of coherent optical OFDM with tolerance against pump phase-noise using reconfigurable coherent multi-carrier pumping", *Optics Express, vol. 24, Sep. 2016.*

[13] **<u>T. Bo</u>**, J. Tang, C.K. Chan "Modulation Format Recognition for Optical Signals Using Connected Component Analysis", submitted to *IEEE Photonics Technology Letters*.

[14] **T. Bo**, C.K. Chan "Common Phase Error Estimation in Coherent Optical-OFDM Systems Using Best-fit Bounding Box", submitted to O*SA Optics Express*.